Study of optomechanical parametric instabilities in the Advanced Virgo detector

David Cohen

To cite this version:

David Cohen. Study of optomechanical parametric instabilities in the Advanced Virgo detector. Astrophysics [astro-ph]. Université Paris-Saclay, 2021. English. NNT : 2021UPASP031 . tel-03259687

HAL Id: tel-03259687
https://theses.hal.science/tel-03259687v1

Submitted on 14 Jun 2021

Study of optomechanical parametric instabilities in the Advanced Virgo detector

Étude des instabilités paramétriques optomécaniques pour le détecteur Advanced Virgo

Thèse de doctorat de l'université Paris-Saclay

École doctorale n° 576, Particules, Hadrons, Énergie, Noyau,
Instrumentation, Imagerie, Cosmos et Simulation (PHENIICS)
Spécialité de doctorat: Astroparticules et Cosmologie
Unité de recherche : Université Paris-Saclay, CNRS, IJCLab, 91405, Orsay, France
Référent : Faculté des sciences d'Orsay

Thèse présentée et soutenue à Paris-Saclay,
le 29/03/2021, par

David COHEN

Composition du Jury

Sophie HENROT-VERSILLÉ Directrice de recherche, Université Paris-Saclay, IJCLab	Présidente
Ettore MAJORANA Professeur, Università di Roma	Rapporteur & Examinateur
Frédérique MARION Directrice de recherche, Université Savoie Mont Blanc, LAPP	Rapporteuse & Examinatrice
Jérôme DEGALLAIX Chargé de recherche, Université de Lyon, LMA	Examinateur
Sophie KAZAMIAS Professeure, Université Paris-Saclay, IJCLab	Examinatrice

Direction de la thèse

Nicolas ARNAUD Chargé de recherche, Université Paris-Saclay, IJCLab	Directeur de thèse
Thibaut JACQMIN Maitre de conférences, Sorbonne Université, LKB	Coencadrant de thèse

Thèse de doctorat

NNT : 2021UPASP031

À ma mère,

Contents

Résumé

En 1915, Albert Einstein publia sa théorie de la relativité générale et prédit à la fois l'existence d'ondes gravitationnelles et des trous noirs. Les ondes gravitationnelles sont des oscillations de la courbure de l'espace-temps engendrées par des masses accélérées se déplaçant à la vitesse de la lumière. Les objets les plus susceptibles de produire des ondes gravitationnelles détectables (pour le moment et sur Terre) sont les coalescences de systèmes binaires, comme des binaires de trous noirs ou d'étoiles à neutron. Après avoir introduit brièvement le concept des ondes gravitationnelles, le chapitre 1 présente quelques autres sources d'ondes gravitationnelles importantes. Ces évènements astronomiques libèrent des quantités d'énergie quasiment incomparables à quelque autre évènement physique, et pourtant, l'amplitude relative de la courbure spatiale due au passage de l'onde est extrêmement faible : 10^{-21}.

Bien que la théorie de la relativité générale fut relativement vite acceptée, l'existence des ondes gravitationnelles, quant à elle, prit beaucoup plus de temps : ce fut seulement après la conférence de Chapel Hill de 1954 que la communauté aboutit à un consensus ; une fois l'existence des ondes gravitationnelles entérinée, le développement d'instruments capables de détecter de telles ondes put commencer. C'est ainsi que Joseph Weber mit au point, dans les années 1960, la *barre de Weber* qui est composée de plusieurs couches d'aluminium (AL5056), agissant comme une antenne. Cependant, ses observations n'ont pu être confirmées. Il faudra encore attendre plus de 40 ans pour obtenir la première détection directe : le 14 septembre 2015. En parallèle du travail de Weber, Mikhail Gertsenshtein et Vladimir Pustovoit travaillèrent sur un dispositif plus sensible, ayant une bande fréquentielle de détection plus large, et étant sensible aux déplacements différentiels : un interféromètre de Michelson. Cette solution vit le jour par la création du Laser Interferometer Gravitational-wave Observatory (LIGO), dont les deux détecteurs furent terminés en 2000 ; et de Virgo, terminé en 2003. Ces deux collaborations travaillent ensemble et permirent cette fameuse première détection, qui fut le signal produit par la coalescence d'un système binaire de trous noirs. Avant cette observation, seulement l'étude de la décroissance orbitale du pulsar binaire PSR1913+16 avait fourni une preuve indirecte de l'existence de telles ondes. Depuis la première observation directe, la collaborations LIGO-Virgo a annoncé quanrante-neuf nouvelles détections. Des informations supplémentaires sur quelques-unes de ces détections sont données en fin de chapitre 2.

Le principe de détection interférométrique est le suivant : on cherche à mesurer une différence de variation de longueur des bras de l'interféromètre lorsqu'une onde graviationnelle passe. En effet, les ondes graviationnelles sont des ondes transverses, donc les deux bras de l'interféromètre ne seront pas étirés ou compressés de la même manière, au même moment. Toutefois, un interféromètre de Michelson basique nécessiterait des bras de plusieurs centaines de kilomètres afin de pouvoir espèrer être sensible à des déplacements aussi faibles que ceux engendrés par le passage d'une onde graviationnelle. C'est pourquoi, un détecteur inteférométrique d'ondes gravitationnelles est une version améliorée d'un interféromètre de Michelson, auquel des cavités optiques ont été ajoutées afin d'améliorer sa sensibilité. Aujourd'hui, la version la plus optimisée comprend quatre cavités optiques : deux dans les bras pour alonger artificiellement le chemin optique, une au niveau du port symétrique (entrée) pour recycler la puissance, et une au niveau du port antisymétrique (sortie) pour régler la sensibilité à des fréquences d'intérêt. Ces améliorations permettent à la fois d'augmenter la variation de puissance mesurée due au passage d'une onde graviationnelle, et de diminuer certains bruits ; ces deux aspects reviennent à améliorer la sensibilité du détecteur. Tout

ceci est détaillé au chapitre 2.

Instabilités optomécaniques

Parmi tous les aspects physiques et technologiques qui peuvent être améliorés dans la quête d'une meilleure sensibilité, augmenter la puissance laser en entrée d'interféromètre est une priorité. Par contre, une puissance plus importante signifie également que l'effet de la pression de radiation des photons sur les miroirs est plus importante ; ce qui peut avoir comme conséquence l'apparition d'instabilités paramétriques optomécaniques *optomechanical parametric instability (OPI)*, qui sont au centre du chapitre 3. Ces instabilités — qui peuvent avoir lieu au sein de n'importe quelle cavité optique — sont dues à des effets non linéaires provenant du couplage de trois modes : un mode mécanique propre d'un miroir, le mode fondamental de la cavité optique (TEM_{00}), et un mode optique de plus haut ordre, appelé *higher-order mode (HOM)*. Ce type de couplage non linéaire est proche de la diffusion Mandelstram-Brillouin : dans une cavité, un photon de fréquence ω_0 du mode fondamental est diffusé vers un photon de plus basse fréquence ω_1 (un autre mode de la cavité optique), et vers un phonon de fréquence ω_m ; ce phonon excite le mode mécanique du miroir. La relation de conservation d'énergie suivante peut être écrite

$$\hbar\omega_0 = \hbar\omega_1 + \hbar\omega_m. \tag{1}$$

Comme le photon diffusé a moins d'énergie que le photon absorbé, ce procédé est appelé *processus de Stokes*. La fréquence de battement (« beat note ») entre les deux modes optiques génère une oscillation de la radiation de pression à la différence de fréquences $\omega_0 - \omega_1 \approx \omega_m$, fournissant de l'énergie au mode mécanique. À son tour, le mode mécanique intéragit avec le mode fondamental et intensifie le processus de diffusion du phonon. Si l'intensité du mode fondamental atteint un certain seuil, le couplage non linéaire entre les trois modes produit ladite instabilité paramétrique. Figure 1(a) montre le processus de Stokes. Il faut également tenir compte du processus inverse, c'est-à-dire le *processus d'anti-Stokes*, pour lequel le photon diffusé a plus d'énergie que le mode fondamental ($\hbar\omega_1 = \hbar\omega_0 + \hbar\omega_m$). À l'inverse du processus « chauffant », celui-ci prend de l'énergie au mode mécanique, ce qui l'affaiblit. Ce processus est montré par figure 1(b). Dans le cas d'un processus de Stokes, l'amplitude du mode mécanique se vera croitre exponentiellement, jusqu'à ce qu'elle atteigne un plateau après un certain temps. Le signal associé à l'excitation mécanique du miroir pourrait saturer l'électronique de mesure, et, ainsi, faire perdre le contrôle de l'interféromètre.

Le phénomène d'instabilité entre les trois modes, déclanché par le mouvement thermique du miroir à ω_m, peut être décrit comme une boucle de rétroaction classique. Cette approche est très

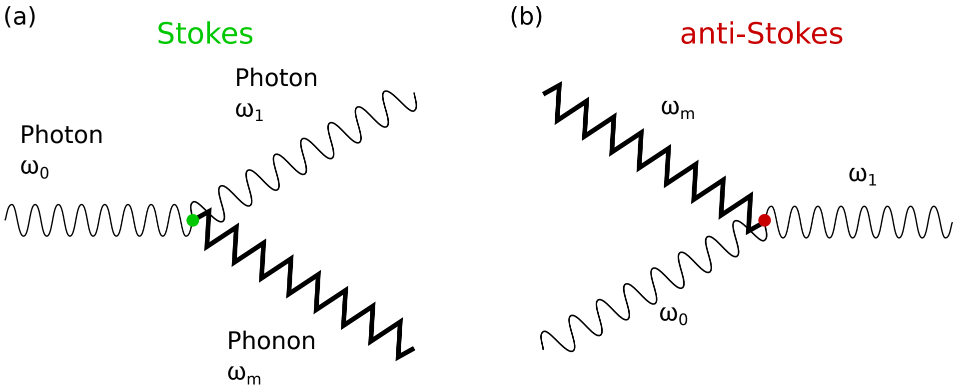

Figure 1 : (a) Processus de Stokes : émission d'un phonon $\omega_0 = \omega_1 + \omega_m$. (b) Processus d'anti-Stokes : absorption d'un phonon $\omega_0 = \omega_1 - \omega_m$. Image créée par Daniel Schwen `http://commons.wikimedia.org`, modifiée, sous les termes de Creative-Commons-License CC-BY-SA-2.5.

pratique car elle peut être adaptée à n'importe quelle configuration d'interféromètre, avec les mêmes formules analytiques. Dans cette approche, le gain paramétrique d'un mode mécanique m avec tous les HOM, prenant en compte et le processus de Stokes et le processus d'anti-Stokes, s'écrit

$$R_m = \underbrace{\frac{8\pi Q_\mathrm{m} P}{M\omega_m^2 c\lambda}}_{\text{préfacteur}} \sum_{n=0}^{\infty} \left(\underbrace{\mathrm{Re}\left[G_n\right]}_{\text{coefficient de transfert optique}} \times \underbrace{B_{m,n}^2}_{\text{chevauchement spatiale}} \right), \tag{2}$$

où Q_m est le facteur de qualité (Q *factor*) du mode mécanique m et ω_m sa fréquence, P la puissance intracavité, λ la longueur d'onde optique, M la masse du miroir, c la vitesse de la lumière ; G_n est le coefficient de transfert optique du $n^{\text{ème}}$ mode optique ; finalement, $B_{m,n}$ est l'intégrale du chevauchement spatial des trois modes. Un mode mécanique est amplifié si $R_m > 0$, et affaiblit si $R_m < 0$. Il devient instable si $R_m > 1$.

Durant la phase d'observation Observing Run 1 (O1), en 2015, LIGO observa une OPI lorsqu'un mode mécanique d'un miroir à 15 kHz devint instable, pour une puissance optique dans les cavités de bras (puissance intracavité) de 50 kW. Nous nous attendions à observer un phénomène similaire à Virgo puisque sa puissance intracavité était déjà bien plus élevée que celle de LIGO. Ce qui devait arriver, arriva : le 7 janvier 2020, un mode mécanique à 155 kHz entra en instabilité jusqu'à, également, faire perdre le contôle de l'instrument. Étant donnés le temps moyen d'un évènement d'onde gravitationnelle de l'ordre de la milliseconde à la seconde, et de leurs fréquences, on doit, à tout prix, éviter de perdre le contrôle de l'interféromètre. D'où l'étude de ces instabilités au sein de la collaboration Virgo.

Modes mécaniques des miroirs de Virgo

Dans le chapitre 4, j'introduis le calcul des modes mécaniques des cavités de bras de Virgo : ils ont été calculés par analyse des éléments finis, par Paola Puppo (INFN Roma). Son analyse a permit d'obtenir les modes mécaniques jusqu'à 157 kHz, avec leur fréquence et facteur de qualité. De plus, elle a effectué des mesures, sur site, des facteurs de qualité et des fréquences des modes mécaniques jusqu'à 40 kHz : ceci a permi d'estimer une incertitude sur les fréquences, et d'ajuster les facteurs de qualité.

Modes optiques des cavités de bras de Virgo

En ce qui concerne les modes optiques de cavités de bras, dans le chapitre 5, j'étudie deux conditions aux limites : miroirs infinis et miroirs finis. La première aboutit à des bases de modes connues, telle que la base des modes *Hermite-Gaussian modes (HGM)*. La deuxième nous impose de résoudre une équations aux valeurs propres afin de trouver les modes propres ; ils sont nommés *finite-sized mirror modes (FSMM)*. C'est une opération beaucoup plus complexe et couteuse d'un point de vue CPU. Cependant, elle permet plusieurs avantages : on peut calculer les modes pour n'importe quelle forme de miroir (déformations intrinsèques, déformations thermiques, etc.) ; les modes obtenus sont a priori plus proches de la réalité ; on obtient directement les pertes de diffraction des modes. En effet, ce dernier point est particuler dans le cas des HGM puisque, par définition, ces modes sont ceux si les miroirs sont infinis. C'est pour cela que, pour les HGM, nous devons estimer les pertes de diffraction.

Enfin, je confronte les deux bases. Pour cela, j'ai choisi trois paramètres permettant de décrire complètement les modes optiques : la forme du mode, la perte de diffraction (définit la largeur à mi-hauteur de la résonance optique), et la phase de Gouy (définit la fréquence de résonance optique). En ce qui concerne la forme du mode, j'ai choisi de montrer la projection, sur la base des HGM, de quelques FSMM : on se rend compte qu'à partir de l'ordre 7, les projections ne sont plus une combinaison linéaire de HGM de même ordre. Pour la perte de diffraction, on observe que notre évaluation des pertes de diffraction des HGM est sousestimée pour tous les modes, mais devient non négligeable à partir de l'ordre 5. Et à propos des phases de Gouy, on observe une nette déviation des phases de Gouy des FSMM, par rapport à celles des HGM, dès l'ordre 8. On en conclut que, dès l'ordre 5, les HGM ne sont plus suffisants pour décrire proprement les modes des cavités de bras de Virgo.

Calcul du gain paramétrique dans la configuration de Virgo

Afin de calculer le gain paramétrique des modes mécaniques, j'ai écrit un programme orienté objet. Ce programme a été vérifié au moins grâce à une comparaison avec le logiciel Finesse et une reproduction de résultats d'un article scientifique. Grâce à cela, j'ai pu vérifier les résultats attendus quant à la différence des deux bases optiques. Puis, j'ai pu faire tourner des simulations dans différentes configurations de Virgo : celles d'O3 et O4. De plus, ces simulations sont effectuées pour différents points de fonctionnement (rayons de courbure) des miroirs de fin de cavité des bras. En effet, cela est nécessaire pour de multiples raisons : l'incertitude du point réel de fonctionnement ; des anneaux chauffant sont fixés autour des miroirs afin de pouvoir modifier le rayon de courbure de ces derniers, et c'est ce qui peut être utilisé afin d'atténuer ou supprimer une éventuelle instabilité ; il existe une incertitude non négligeable sur les fréquences mécaniques, et je montre qu'au lieu de faire varier ces fréquences, il revient au même de faire varier les rayons de courbure des miroirs.

Les premiers résultats obtenus, donnés en chapitre 6, ceux d'O3, ont permis, etre autres, de vérifier que la densité d'instabilité était en effet relativement faible. Puis, lorsque le 7 janvier 2020 Virgo observa pour la première une OPI, nous avons pu utiliser nos outils de simulations pour s'assurer de l'origine OPI de cette instabilité d'une part, et de vérifier, encore, la fonctionnabilité de nos outils de simulation d'autre part.

Pour la prochaine phase d'observation, O4, la cavité de recyclage du signal sera installée. Cette cavité pourrait permettre à certains HOM de perdurer dans l'interféromètre. Ceci se traduit par un mode avec moins de pertes, ce qui se traduit à son tour par des résonances ayant une largeur à mi-hauteur plus fine. Donc, la densité d'instabilité devrait diminuer, mais, comme la hauteur maximum des résonances est augmentée, les gains paramétriques pourraient être plus élevés. C'est effectivement ce que l'on observe, et ce que je montre en figure 2, où les lettres sont les labels des OPI, dont on retrouve les informations en tableau 1. Au final, 15 modes mécaniques ont été identifiés comme potentiellement instables ; ces instabilités, si elles ont lieu, auront des gains paramétriques plus élevés qu'ils ne l'auraient été dans la configuration d'O3, impliquant une instabilité plus rapide ; par contre, les résonances étant plus fines, il sera plus facile de s'en éloigner grâce aux anneaux chauffants.

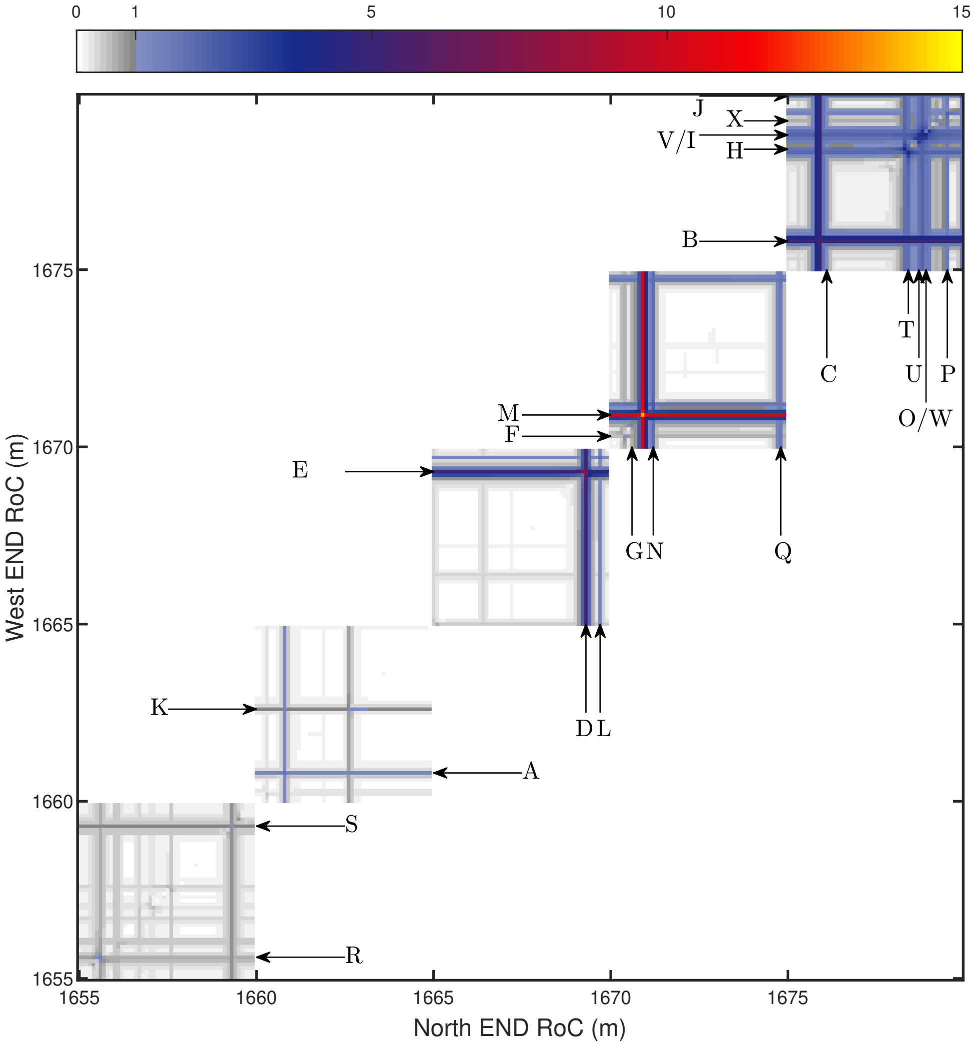

Figure 2 : (a) R_m vs rayons de courbure des miroirs de fin de cavité, utilisant les FSMM, à puissance d'entrée 50 W (puissance nominale), pour la configuration de O4 ; tous les 12 750 modes mécaniques jusqu'à 157 kHz. L'échelle de nuances de gris représente les gains paramétriques inférieurs à 1, alors que la colorée indique les instabilités ($R_m > 1$). Chaque résonance de mode mécanique peut se voir sur les deux cavités de bras ; cependant, par soucis de clareté, seulement une cavité est pointée pour chaque mode mécanique, et le choix de l'axe est purement arbitraire.

Label	Fréquence (kHz)	$\Delta\nu_{\mathrm{max}}$ ($\pm 10^2$ Hz)	Ordre optique	R (m)	ΔR_{max} ($\pm$m)	R_m
A	16.015	0.80	3	1660.8	0.89	1.7344
B	23.128	1.2	4	1675.9	1.0	5.3664
C	23.258	1.2	4	1676.1	1.0	1.3776
D	61.154	3.1	2	1669.3	5.2	7.6253
E	61.160	3.1	2	1669.4	5.2	2.9983
F	61.216	3.1	2	1670.4	5.2	1.0805
G	61.231	3.1	2	1670.6	5.2	1.3914
H	61.676	3.1	2	1678.4	5.2	2.5652
I	61.705	3.1	2	1679.0	5.2	3.3382
J	61.759	3.1	2	1679.9	5.2	2.6389
K	66.150	3.3	3	1662.7	3.7	1.1813
L	66.784	3.3	3	1669.7	3.7	2.0182
M	66.888	3.3	3	1670.9	3.7	14.0449
N	66.912	3.3	3	1671.2	3.7	2.4578
O	67.567	3.4	3	1678.9	3.8	0.8203
P	67.616	3.4	3	1679.5	3.8	2.1297
Q	72.971	3.6	4	1674.8	3.0	1.7454
R	105.112	5.3	1	1655.6	18	1.4159
S	115.812	5.8	3	1659.3	6.4	1.0308
T	155.756	7.8	1	1678.4	26	4.4221
U	155.765	7.8	1	1678.7	26	3.2889
V	155.768	7.8	1	1678.8	26	4.6354
W	155.770	7.8	1	1678.9	26	3.9399
X	155.780	7.8	1	1679.2	26	1.3523

TABLE 1 : Tous les modes mécaniques instables d'O4 sur toute la gamme de rayon de courbure choisie. $\Delta\nu_{\mathrm{max}}$ est la déviation maximale en fréquence due aux incertitudes. R est le rayon de courbure auquel le mode mécanique résonne. R_m est le gain paramétrique maximum sur toute la gamme de rayon de courbure. L'ordre optique est l'ordre du mode optique qui contribue le plus à cette OPI, c'est-à-dire au rayon de courbure correspondant (ou phase de Gouy de cavité de bras). ΔR_{max} est la déviation maximale en rayon de courbure correspondant à la déviation maximale en fréquence. Les lignes en vert-beu foncé représentent les modes mécaniques qui pourront être instables au point de fonctionnement 1667 m. H, I, J, O, P, et Q pourraient être dans le voisinage de ce point de fonctionnement (en vert-bleu clair) ; ils pourraient donner lieu à une OPI si le point de fonctionnement est un peu modifié.

Introduction

In 1915, Albert Einstein published the General Relativity theory and predicted the existence of gravitational waves. But gravitational waves are so weak that the first direct detection only occurred a century later; on 14th September 2015, ground-based interferometric gravitational-wave detectors finally recorded a signal produced by a Binary Black Holes coalescence. In the meantime, the study of the binary pulsar PSR1913+16 had provided an indirect evidence of the existence of gravitational waves.

The operating principle of interferometric gravitational-wave detectors is based on an enhanced version of a Michelson interferometer, to which optical cavities are added to improve its sensitivity. To date, the most enhanced configuration includes four optical cavities: two in the arms to artificially lengthen the optical path, one at the symmetric port (the input) to recycle the power, and one at the antisymmetric port (the output) to tune the sensitivity at specific frequencies of interest.

Since the first direct observation, the LIGO-Virgo Collaboration announced 49 new detections. On 1st August 2017, the Virgo detector joined the two LIGO detectors for a first joint data taking period with three advanced (second generation) detectors. For Virgo, this was the outcome of a multi-year upgrade program during which most components of the detector were upgraded, with the goal of improving its sensitivity by an order of magnitude.

Amongst all the physical and technological aspects that can be improved in the pursuit of a better sensitivity, increasing the laser input power is a major key. A higher power also implies that effects due to the radiation pressure of the photons on the mirrors are increased. Among those effects, an optomechanical parametric instability, referred to as optomechanical parametric instability (OPI), can occur. That is why, after introducing the gravitational waves and their sources in chapter 1, and the principle of interferometric detection in chapter 2, I give a presentation of the OPI process and the computational formalism for interferometric gravitational-wave detectors in chapter 3.

The OPI is driven by three modes: the fundamental optical mode, a higher-order mode (HOM), and a mechanical mode. An OPI can occur if the optical beat note — that is the frequency difference between the two optical mode frequencies — is near the mechanical mode frequency, such that the mechanical mode is coherently driven. Hence, we need to evaluate the optical modes of Advanced Virgo (AdV)'s arm cavities and the mechanical modes of its mirrors. In chapter 4, I briefly introduce how we obtained the mechanical modes. Chapter 5 tackles the optical modes: I study and compare two different bases from two different boundary conditions.

Finally, in chapter 6, I briefly introduce the validation of my program thanks to which we can forecast AdV's OPI behaviour in various configurations, namely those of Observing Run 3 (O3) and Observing Run 4 (O4). This thesis is written between these two Observing Runs; therefore, O3 results are a validation rather than a prediction. I will show, as well, that, due to non-negligible uncertainties, we cannot provide thorough prognoses. Notwithstanding, the results obtained for O4 configuration can considerably help apprehend how AdV may behave with regard to OPIs; furthermore, they provide us with a good idea of what mechanical mode frequencies can lead to an OPI.

Chapter 1

Gravitational waves

Gravitational waves are ripples of the curvature of spacetime. They are emitted by accelerating massive bodies and travel at the speed of light. The existence of such waves were first discussed in 1893 by Oliver Heaviside following an analogy between electricity and gravitation [1] [1]. In 1905, Henri Poincaré suggested that those waves (*ondes gravifiques* as he himself called them) emerge from massive bodies in motion and travel at the speed of light such that they respect the Lorentz transformation [2], which describes the relation between the three space coordinates and the time for a flat space (*Minkowski space*).

From Lorentz and Poincaré's work arose Albert Einstein's *special relativity* in 1905, in which he posited that nothing can travel faster than the speed of light. The instantaneous aspect of Newton's theory of gravitation does not fit this last assertion and this is how, in 1915, Albert Einstein unveiled his *general relativity* theory [3] — generalising the relativity to curved space — and predicted the existence of gravitational waves shortly thereafter. But, the main difference from his forerunners lies in the fact the space and the time are not absolute but relative to the observer [2]. These two notions, formerly completely independent, are now part of a single concept: a four-dimensional manifold, the so-called spacetime, which is curved by masses. He thus opened an entirely novel field of physics, which can both extrapolate Newton's theory of gravitation to relativistic speeds and solve some built-in problems, such as the decoupling of gravity to massless objects. One hundred years later, on 14 September 2015, the first gravitational waves (emitted by a *Binary Black Holes (BBH)*) were detected by the LIGO-Virgo collaboration [4]. Before this observation, the existence of gravitational waves had only been indirectly detected by the decrease of the orbital period of the binary pulsar PSR B1916+13, discovered in 1974 by Russel Hulse and Joseph Taylor [5]. Since the very first observation, many new detections have been performed [6,7], which endorse the existence of gravitational waves.

1.1 General relativity and gravitational waves

According to general relativity, the gravitation results of the curvature of spacetime by mass and energy, through the *Einstein equation.* In other words, 'space tells matter how to move' and 'matter tells space how to curve' [8]. This is actually pretty similar to the determination of electromagnetic waves by the Maxwell's equations. Indeed, charges and currents allow to determine electromagnetic fields, as well as mass-energy and momentum allow to determine the spacetime geometry. The *Einstein equation* is:

$$G_{\mu\nu} = \frac{8\pi G}{c^4} T_{\mu\nu} \tag{1.1}$$

---

[1] In this article, he also mentioned that gravitation could propagate at the speed of light, which goes against Newton's theory of gravitation, for which gravitation interaction is instantaneous.

[2] One does not consider Poincaré as the spacetime's father because he first thought that the 'local time' introduced by the Lorentz transformation was only a mathematical tool.

where $G_{\mu\nu}$ is the Einstein tensor, which describes the curvature of a manifold, $T_{\mu\nu}$ the stress-energy tensor, which describes the matter distribution, G the Newton's gravitational constant, and c the speed of light. The coefficient $8\pi G/c^4$ being of the order of 10^{-43}, spacetime is extremely rigid, explaining, thus, the weakness of the gravitational waves. The Einstein tensor can be written as:

$$G_{\mu\nu} = R_{\mu\nu} - \frac{1}{2} R g_{\mu\nu} \tag{1.2}$$

where $R_{\mu\nu}$ is the Ricci curvature tensor, which describes the spacetime curvature, $g_{\mu\nu}$ the metric tensor, and R the scalar curvature.

Usually, the Einstein equation cannot be directly solved, but it can be linearised in the case of small perturbations:

$$g_{\mu\nu} = \eta_{\mu\nu} + h_{\mu\nu} \tag{1.3}$$

where $\eta_{\mu\nu}$ describes an infinite space without gravitation, and $|h_{\mu\nu}| \ll 1$. This weak-field approximation is suitable for the Solar system or for weak gravitational waves [8]. Then, using such a linearisation alongside with a *Lorentz gauge* yields a wave equation from eq. (1.1) [8,9]:

$$\underbrace{\left(\nabla^2 - \frac{1}{c^2}\frac{\partial^2}{\partial t^2}\right)\overline{h_{\mu\nu}}}_{\text{propagation term}} = -\frac{16\pi G}{c^4}\underbrace{\left(T_{\mu\nu} - \frac{1}{2} g_{\mu\nu} T^k_k\right)}_{\text{source term}} \tag{1.4}$$

with:

$$\overline{h_{\mu\nu}} = h_{\mu\nu} - \frac{1}{2}\eta^{\mu\nu} h_{\mu\nu}\eta_{\mu\nu} \tag{1.5}$$

If the assumption of being far from the source is valid, the source term can be neglected. Hence, the general solution of eq. (1.4) is a superposition of monochromatic plane waves: the *gravitational waves*. A single monochromatic wave can be written as [10]:

$$h_{\mu\nu} = \left(h_+ \varepsilon^+_{\mu\nu} + h_\times \varepsilon^\times_{\mu\nu}\right) e^{-i(\omega_{\mathrm{GW}} t - k_{\mathrm{GW}} z)} \tag{1.6}$$

where ω_{GW} and k_{GW} are respectively the pulsation and the wave vector of the gravitational wave, and $\varepsilon^+_{\mu\nu}$ and $\varepsilon^\times_{\mu\nu}$ the polarisation tensors of a wave propagating along the z-axis; they are defined as:

$$\varepsilon^+_{\mu\nu} = \begin{pmatrix} 0 & 0 & 0 & 0 \\ 0 & 1 & 0 & 0 \\ 0 & 0 & -1 & 0 \\ 0 & 0 & 0 & 0 \end{pmatrix} \quad \text{and} \quad \varepsilon^\times_{\mu\nu} = \begin{pmatrix} 0 & 0 & 0 & 0 \\ 0 & 0 & 1 & 0 \\ 0 & 1 & 0 & 0 \\ 0 & 0 & 0 & 0 \end{pmatrix} \tag{1.7}$$

Indeed, alongside with electromagnetic waves, gravitational waves are transverse, that is, the forces are perpendicular to the direction of propagation. However, a gravitational wave stretches and squeezes an object along two axes. Half a period later, the axis that was stretched is then squeezed and vice versa. Thus, two polarisations can describe this configuration: one called + and the other one called ×. An effect of a gravitational wave over a test mass circle is shown in fig. 1.1. Both stretch and squeeze are proportional to the length of the object: the larger the object, the more it stretches, as [11,12]

$$\frac{\delta L}{L_0} = \frac{h}{2} \tag{1.8}$$

where L_0 is the length of the object, δL the length variation due to the gravitational wave, and h the gravitational wave *strain amplitude*. In fig. 1.1 it is also shown that the relative displacement along two orthogonal axes is opposite. Using an interferometer permits to have a signal twice higher than that of a single cavity, and cancel out a lot of noises that would be dominant with a single cavity.

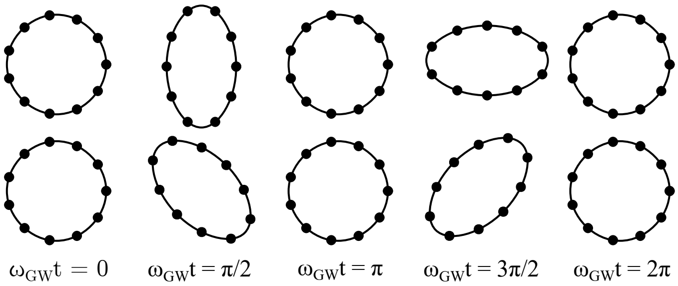

Figure 1.1: Effect of a gravitational wave over a ring of free-falling masses for a + polarisation (top) and a × polarisation (bottom).

1.2 Sources of gravitational waves

As already mentioned, gravitational waves are emitted by accelerating massive bodies. However, only astrophysical compact bodies can be detectable by ground-based detectors [13]. Indeed, the gravitational luminosity of a source can be written as [11, 12]

$$\mathcal{L} \sim \frac{c^5}{G}\,\varepsilon^2 \left(\frac{R_S}{R}\right)^2 \left(\frac{v}{c}\right)^6 \tag{1.9}$$

where ε is the source asymmetry, R the source radius, $R_S = \frac{2GM}{c^2}$ the Schwarzschild radius, which is the radius of a mass-equivalent black hole [3], thus $\frac{R_S}{R}$ represents the object compactness, and v its velocity.

Table 1.1 shows some compactness factors of astronomical objects of interest:

Object	Black hole	Neutron star	Sun	Earth
$\frac{R_S}{R}$	1	0.30	10×10^{-6}	3×10^{-8}

Table 1.1: Compactness factors of some astronomical objects. The black hole's value is 1 by definition of the Schwarzschild radius.

Hence, according to eq. (1.9), to be a good gravitational-wave emitter, a source has to be *asymmetric* ($\varepsilon \sim 1$), *compact* ($R_S/R \sim 1$), and *relativistic* ($v/c \sim 1$). According to these conditions, four major expected source categories can be detectable by ground-based detectors: 'burst' signals, compact binary system coalescences, neutron stars, and the stochastic background. The two first of these are extremely energetic events occurring during the life of some very massive stars (from 6–10 $\mathrm{M}_\odot$ [4]) Let us summarise here the main different faiths of stars, which will eventually help to introduce these events.

The story of a star depends on its mass: the heavier, the higher the gravity, the hotter, the faster it consumes its hydrogen. Therefore, the heavier, the younger the star dies. In the first stage of their life, almost all stars experience the same process called *main sequence*, during which they mainly fuse their hydrogen into helium. This fusion reaction allows a hydrostatic equilibrium and, thus, the existence of the star itself as it induces an outward thermal pressure balancing the inward gravity pull. Once all the hydrogen is fused, if its mass is high enough, the star continues fusing heavier elements until the iron (the most stable element). Eventually, as nuclear fusion reactions cease (when the iron core reaches the Chandrasekhar limit of about 1.4 $\mathrm{M}_\odot$), the star is only subjected to its own gravitational pull and hence collapses until the iron core reaches nuclear densities, leading its protons to catch electrons and form neutrons; this leads to a very compact

---

[3] This general relativity definition matches the one which can be derived in classical (Newtonian) physics by setting the escape velocity equal to the light speed.

[4] The symbol $\mathrm{M}_\odot$ stands for *solar mass*.

neutron core that can withstand the whole collapse energy, which produces an outward shock wave and gives birth to an astonishing astronomical show: the so-called *supernova*. The 'corpse' of a star dying this way can be either a *neutron star* or, if the core mass reaches a certain limit (the Tolman–Oppenheimer–Volkoff limit [14–17]), a *black hole*.

1.2.1 'Burst' signals

One calls a 'burst' signal a high bandwidth signal over a short period of time. They are categorised as 'transient sources'. In terms of gravitational waves, one expects to observe this kind of signal for some supernova events like type-II supernovas [5] or for hypothetical cosmic strings.

The former should emit gravitational waves mostly because of its asymmetry. One used to expect that supernovas would emit a significant amount of energy as gravitational waves, but simulations have shown that the gravitational radiation fraction with respect to the total mass energy of the star would be of the order of 10^{-6} [18]. Moreover, the rate of supernovas is rather low: between three and five within a century in the Milky Way (whose diameter is estimated to 460–710 kpc [6]), one every other year at 3–5 Mpc, one per year at 12 Mpc, and maybe two or three per year if one includes the Virgo cluster located at 16.5 Mpc.

1.2.2 Compact binary system coalescences

In the Universe can be formed systems of two very compact bodies, like neutron stars and black holes, spiralling around each other, thus radiating power through gravitational waves. The more the energy is lost (by radiation), the faster the objects spiral and the closer they get until they eventually merge into an even more massive object. By turning faster, the strain amplitude of the emitted gravitational waves increases (see eq. (1.9)); this phenomenon is directly observed in the detected signal by its so-called *'chirp'* shape (see fig. 2.12): both the signal amplitude and frequency increase with respect to time. This kind of source is definitely a good emitter of gravitational waves: it is clearly asymmetric and compact, and the closer the two objects get, the faster they spiral, the more relativistic the system speed gets. While the two objects are spiralling, the emitted gravitational wave frequency is too low for detection (mHz) and the only part of the event that is observable by ground-based detectors is its very end, right before the merge, when the wave frequency is within the detection bandwidth (> 10 Hz). Hence, these sources are also considered as *transient sources* even though they actually emit gravitational waves over a very long period of time (hundreds of millions of years).

To date, this is the only kind of event that has been detected: fifty events, of which only two Binary Neutron Stars (BNS) have yet been confirmed. All these events were recorded during Observing Run 1 (O1), Observing Run 2 (O2), and Observing Run 3 (O3) (see section 2.4). The expected rates of binary system coalescences are between 10^{-10} and $10^{-5}\,\mathrm{Mpc^{-3}\,yr^{-1}}$ [19]. These values consider the uncertainties and the different binary system types: BNS, Neutron Star – Black Hole (NS-BH), and BBH.

The detection range of ground-based gravitational-wave detectors — which is directly linked to the sensitivity (see section 2.2.1) — is traditionally given by a figure of merit called *BNS range*, which corresponds to the distance at which the coalescence of two $1.4\,\mathrm{M_\odot}$ neutron stars would be detected with a Signal-to-Noise Ratio (SNR) of 8.

A realistic BBH system could emit a gravitational wave with a strain amplitude of [20]

$$h \sim 10^{-21}. \tag{1.10}$$

This order of magnitude is the highest that one can expect to observe from astronomical sources.

---

[5] This notation can be misleading. Indeed, originally, the *type* of a supernova determines its spectrum: type-I has no hydrogen, whereas type-II does. However, one can also classify them according to the way they are produced: either by *thermal runaway* (type-Ia) or by *core collapse* (all the others). Only the latter is expected to produce (observable) gravitational waves; hence this 'mistake' including type-Ib supernovas within type-II ones.

[6] A *parsec* (pc) is defined as $\frac{648000}{\pi}$ au, that is to say about 3.26 ly (*lightyear*). And an *astronomical unit* (au) is the distance from the Earth to the Sun, which is about 150×10^6 km or 8 'lightminute'.

1.2.3 Neutron stars

Neutron stars are objects spinning very fast and emitting a high magnetic field. As they are very dense objects (table 1.1), if their mass happen to be asymmetrical, then they could emit gravitational waves. Pulsars are neutrons stars whose magnetic field axis is not parallel to its spinning axis. This produces a very stable periodic signal of radio waves that can be precisely measured; that is why there are seen as astronomical ‘lighthouses’. In terms of gravitational waves detection, this helps reconstruct the signal, whose frequency is twice that of the star rotation. These sources are *continuous sources*: one can integrate the signal over time to increase the SNR.

1.3 From idea to reality

Unlike the the existence of gravitational waves, general relativity was quickly acknowledged by academics. Albert Einstein himself proposed three tests to validate his theory: the perihelion precession of Mercury, the light deflection by the Sun, and the gravitational redshift.

The perihelion precession of Mercury In 1859, Urbain Le Verrier reported that the perihelion precession [7] of Mercury calculated theoretically taking into account the motion of all planets disagreed with the experimental value. Only by adding the gravitational field effects could Albert Einstein resolve this anomaly.

The light deflection by the Sun The idea that the light should be bent by the attraction of a massive body, such as the Sun, was already stated by Henry Cavendish in 1786 [21] and Johann Georg von Soldner in 1804 [22]. However, taking into account only Newton’s theory of gravitation yields a wrong estimation of the deflection that can be corrected considering general relativity. The *Eddington experiment*, organised by Arthur Eddington and Frank Dyson in 1919, was the first attempt to verify Einstein’s prediction by measuring the starlight deflection passing near the Sun during a solar eclipse [23].

The gravitational redshift Einstein expected gravitational fields to shift spectral rays towards red. This effect should be weak for the Sun but detectable with *white dwarf* stars, which are much more dense. A first observation of this effect was made in 1925 by Walter Adams for the Sirius-B white dwarf star [24]. Again, the reliability of this measure was questioned and the first accepted accurate measurement was done in 1954 by Daniel Popper for the Eri B white dwarf [25].

Concerning the existence of gravitational waves, it was another business. Einstein himself never fully believed in Poincaré’s idea. In 1922 (six years after Einstein’s general relativity), Eddington stated that ‘gravitational waves propagate at the speed of thought’. Not until the Chapel Hill conference in 1957 was reached a consensus about their existence: a couple of thought experiments explaining how gravitational waves could transmit energy were proposed to the audience and put an end to the matter. Subsequently, the development of instruments able to detect such elusive signals started (detailed in the next chapter).

The first observation of gravitational waves, though, was not made directly. In 1974, Russel Hulse and Joseph Taylor discovered the binary pulsar PSR B1916+13 (or PSR J1915+1606, or PSR 1913+16, or the Hulse–Taylor binary), which was the first binary pulsar ever observed. General relativity predicts that such systems should see their orbital momentum decay by emitting gravitational waves, and this is exactly what Hulse and Taylor measured and found to be in agreement with the theory. A Nobel Prize of Physics in 1993 ‘for the discovery of a new type of pulsar, a discovery that has opened up new possibilities for the study of gravitation’ rewarded their double achievement.

---

[7] The *perihelion* is, for a Solar System object, the closest point to the Sun of its orbit. For any two-body system it is called *periapsis* and is fixed. However, as many bodies are in the Solar System, one another’s gravitational interaction causes this point to move around the Sun: this is the *precession*.

Chapter 2

Advanced Virgo: a ground-based gravitational-wave detector

In the previous chapter, I have introduced the basics about gravitational waves and their sources. Here, I will focus on how gravitational waves are detected and the technical solutions to improve their detections, and I will present some recent detections.

After the Chapel Hill conference of 1954, the interest to gravitational waves took off and the challenge to detect them was launched. In the 1960s, Joseph Weber pioneered the challenge — or at least he was eventually convinced he had — by designing a device, called after him, the Weber bar [26–28]. The principle of this detector consists in several aluminium (AL5056) cylinders acting as an antenna, whose fundamental mechanical mode (1660 Hz for Weber's device [28]) is expected to get excited by strains in space due to the passage of a gravitational wave. Tiny variations of the antenna's length are read out with piezo crystals. Although the sensitivity of his detector was not good enough and nobody could reproduce his results [28], improvements were carried on to improve the sensitivity of bar detectors up to $3 \times 10^{-22}\,\mathrm{Hz}^{-1/2}$ in a $\sim 1\,\mathrm{Hz}$ bandwidth back in the 1990s [29]. This technology was still being investigating, together with spherical versions of it, whose strain sensitivity is expected to be from 5×10^{-22} to $4 \times 10^{-23}\,\mathrm{Hz}^{-1/2}$ within a 200 Hz bandwidth [30].

In parallel to Weber's bar technological development, a novel idea was first thought by Mikhail Gertsenshtein and Vladislav Pustovoit: an optical interferometric gravitational-wave detector [31]. This technology enables a much wider detection bandwidth (for it is not only sensitive to the resonance frequency, unlike Weber bars) and is sensitive to differential displacements. In 1967, Rainer Weiss started the construction of a prototype [32]. This solution came forth in 1984 with the foundation of Laser Interferometer Gravitational-wave Observatory (LIGO) as a Caltech/MIT project by Ronald Drever, Kip Thorne, and Rainer Weiss. The two last ones, together with Barry Barish, won the Nobel Prize in Physics in 2017 'for decisive contributions to the LIGO detector and the observation of gravitational waves'. Only after ten years passed did the construction of the two LIGO sites (Hanford and Livingston) start and last until 2000; operation was initiated from 2002 to 2011.

In regard to the Virgo Collaboration, the first design proposal for a detector was delivered to funding agencies in 1992, and approved by the Centre National de la Recherche Scientifique (CNRS) and the Istituto Nazionale di Fisica Nucleare (INFN) in 1994. Its construction lasted from 1996 to 2003 on the site of Cascina, Italy, where European Gravitational Observatory (EGO) was created in 2000. From 2007 to 2011, Virgo performed a series of four scientific runs, among which three were in coincidence with LIGO, but the sensitivity of neither of the detectors was good enough to expect gravitational-wave observations. That is why Virgo experienced an upgrade phase from 2012 to 2016 leading to Advanced Virgo (AdV)[1], and allowing it to join LIGO for the end of Observing Run 2 (O2) (more explanation on Observing runs will be given in section 2.4), during which the first triple detection, GW170814, was made.

---

[1] LIGO was upgraded to Advanced LIGO (aLIGO) from 2010 to 2015.

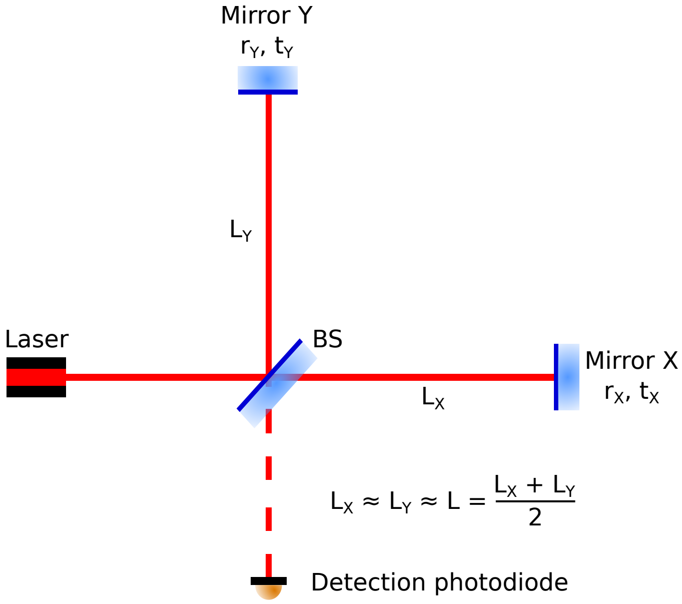

Figure 2.1: Schematic of a Michelson interferometer.

2.1 Michelson interferometry

The Michelson interferometer was invented for the Michelson-Morley experiment, with which Albert Michelson and Edward Morley attempted to detect the effect of the aether[2] on light. They believed that motion of matter would induce a change of the speed of light and wanted to measure this difference between two perpendicular paths of beam lights originally coming from the same source. It happened to be a negative outcome, in that they did not detect any difference of speed. Yet, this gave the 'the first hint [...] in exactly two hundreds years [...] that Newton's laws might not apply all the time everywhere' [33], and helped physics go beyond, towards what eventually became Einstein's special relativity theory.[3]

2.1.1 General

The Michelson interferometer principle consists of injecting a laser beam towards a half reflecting Beam Splitter (BS), which splits the beam light into two perpendicular beams. These beams travel down the interferometer arms, are reflected off the end mirrors towards the BS as shown in fig. 2.1. The recombination of the two beam gives birth to interferences that can be either constructive or destructive, according to the optical path difference (ΔL) between the beams, which is related to the beam phase difference ($\Delta\phi$) as

$$\Delta\phi = \frac{2\pi}{\lambda_0}\,\Delta L = \frac{2\pi}{c}\,\nu_0\,\Delta L = k_0\,\Delta L \tag{2.1}$$

where λ_0 is the laser wavelength, ν_0 its frequency, k_0 its wavenumber, and c the speed of light.

Let us consider a perfect Michelson interferometer: optics without losses, which can be rewritten $\mathcal{T} + \mathcal{R} = 1$ with $\mathcal{T}$ the transmittance in energy and $\mathcal{R}$ the reflectance in energy; end mirrors

---

[2] The *aether* — or *æther* in a more old-fashioned way — has had various definitions throughout history and different branches of knowledge, even if one omits the organics compounds that are only spelled *ethers*. For physicists contemporary to Michelson and Morley, one refers to the *luminiferous aether*, which was believed to be the medium thanks to which light could propagate.

[3] It is interesting to notice how the Michelson interferometer brought about the collapse of the aether idea, from which emerged new ideas that led to the conclusion of the existence of gravitational waves that are now observed thanks to this same instrument.

are strictly reflective, i.e. $\mathcal{T}_{x,y} = 1 - r_{x,y}^2 = 0$ and $\mathcal{R}_{x,y} = r_{x,y}^2 = 1$; and the BS splits perfectly the beam into to beams of same energy, i.e. $T_{\mathrm{BS}} = R_{\mathrm{BS}} = 0.5$. Then arises the output power expression

$$P_{\mathrm{out}} = \frac{P_{\mathrm{in}}}{2} \left(1 + \cos \Delta\phi\right) \tag{2.2}$$

$$\Delta\phi = 2k\,\Delta L_0 = \Delta\phi_0 \tag{2.3}$$

$$\Delta L_0 = L_x - L_y \tag{2.4}$$

where P_{in} the input power of the interferometer, and $L_{x,y}$ the arm lengths. Regarding eq. (2.1), $\Delta L = 2\Delta L_0$, given that each beam performs a round trip within its arm before recombining.

One can notice that

$$P_{\mathrm{out}} = P_{\mathrm{in}} \quad \Rightarrow \quad \Delta L_0 = n\,\frac{\lambda_0}{2}, n \in \mathbb{Z} \tag{2.5}$$

$$P_{\mathrm{out}} = 0 \quad \Rightarrow \quad \Delta L_0 = (2n+1)\,\frac{\lambda_0}{4}, n \in \mathbb{Z} \tag{2.6}$$

$$P_{\mathrm{out}} = P_{\mathrm{in}}/2 \quad \Rightarrow \quad \Delta L_0 = (2n+1)\,\frac{\lambda_0}{8}, n \in \mathbb{Z} \tag{2.7}$$

which correspond to the *bright fringe* (constructive interferences), the *dark fringe* (destructive interferences), and the *grey fringe* (the intermediate situation).

2.1.2 Effect of a gravitational wave

The detection principle consists of measuring a phase change between the laser beams coming from the two arms of the interferometer. Indeed, the passage of a gravitational wave perpendicular to the detector plane (optimal case) induces a change in the optical path length, which induces a phase shift (see eq. (2.1)). This phase shift is directly linked to the shape of the gravitational wave as [34]

$$\delta\Phi = G\,\delta L \tag{2.8}$$

with G the optical gain and δL the length variation, which follows

$$\delta L_{x,y} = \pm\frac{h}{2}\,L_{x,y} \tag{2.9}$$

with L a baseline length and h the gravitational wave strain amplitude. Therefore, the passage of a gravitational wave is detected by a change in the interference produced at the output — or antisymmetric port —, which receives all the differential field. The input — or symmetric port — gets all the common field. A Michelson interferometer is a sensitive instrument thanks to the differential measurement due to the two orthogonal arms, which removes all the common noises.

When a gravitational wave passes, the phase difference is

$$\begin{aligned} \Delta\phi &= 2k\Delta L_0 + 2k(\delta L_x - \delta L_y) \\ &= \quad \Delta\phi_0 \quad + \qquad \delta\phi_{\mathrm{GW}} \end{aligned} \tag{2.10}$$

where $\delta L_x = \frac{hL_x}{2}$ and $\delta L_y = -\frac{hL_y}{2}$ (see eq. (2.9)), and $\delta\phi_{\mathrm{GW}}$ represents the additional phase shift due to the passage of the gravitational wave (see eq. (2.3)). Considering the gravitational wave strain amplitude as very small, one can let $\delta L/L \ll 1$, then $\delta\phi_{\mathrm{GW}} \ll 1$, which allows to write $\cos\left(\delta\phi_{\mathrm{GW}}\right) \simeq 1$ and $\sin\left(\delta\phi_{\mathrm{GW}}\right) \simeq \delta\phi_{\mathrm{GW}}$. Hence, the output power detected is obtained by reporting eq. (2.10) in eq. (2.2)

$$P_{\mathrm{out}}^{\mathrm{GW}} \simeq \frac{P_{\mathrm{in}}}{2}\left[1 + \cos\left(\Delta\phi_0\right) - \sin\left(\Delta\phi_0\right)\delta\phi_{\mathrm{GW}}\right] \tag{2.11}$$

The detected power variation due to a gravitational wave δP_{GW} is then

$$\delta P_{\mathrm{GW}} = -\frac{P_{\mathrm{in}}}{2}\sin\left(\Delta\phi_0\right) 2khL \tag{2.12}$$

Figure 2.2: On the left: aerial view of the AdV detector. On the right: interior of the central building. Credits: Virgo Collaboration.

where $L = \frac{L_x + L_y}{2}$ is the interferometer average length. The detected power variation is optimised at grey fringe and is proportional to the interferometer arm length and the input power.

2.2 Advanced Virgo detector

The Advanced Virgo is an interferometric gravitational-wave detector built in Cascina, Tuscany, Italy. It was initially a project carried by both the CNRS (France) and the INFN (Italy). Nowadays, it includes 106 institutions in 12 different countries, counting more than 550 members [35].

On the photograph showing the aerial view of Virgo in fig. 2.2, one can see the entire North arm and a part of the West arm. At the junction is the Central Building (CB), in which the injection laser, the Power Recycling Mirror (PRM) (see section 2.2.2), the BS, and the Input Mirrors (IMs) (see section 2.2.2). The End Mirrors (EMs) are situated in the two buildings that are at the end of the arms (one can see the North one). Each optic, or test mass, is suspended by a series of inverted pendulums (see section 2.2.1) that are inserted within a vacuum tower. The photograph on the right in fig. 2.2 shows the inside of the CB with the towers of the aforementioned test masses.

The AdV detector is a Michelson interferometer as described in section 2.1. However, to be able to detect the extremely weak signal of gravitational waves, the basic Michelson interferometer needs to be enhanced to improve its sensitivity.

2.2.1 Sensitivity and noise sources

The *sensitivity* is defined as the smallest signal that can be detected; therefore, the objective is to maximise the detected power variation due to a gravitational wave δP_{GW}. We shall see that noises limit the detectable power. Therefore, to improve the sensitivity, one can both try to reduce noises and try to increase the detected power variation (see eq. (2.12)). This section introduces some noises importantly limiting the detector sensitivity, while section 2.2.2 treats of the main technical features that help both increase the detected power variation and decrease the noises.

Instrumental and fundamental physical noises are frequency dependent, so is the sensitivity; this is why it is usually given in terms of *Amplitude Spectral Density (ASD)*, expressed in $\mathrm{Hz}^{-1/2}$ (the amplitude is the square root of the energy). One can, thus, determine the whole sensitivity curve (see fig. 2.5) and obtain the detector bandwidth for given astronomical events. As introduced in section 1.2.2, among the Virgo Collaboration, one rather speaks in terms of Binary Neutron Stars (BNS) range. Figure 2.3 shows the sensitivity both in terms of ASD and BNS range. From O2 to the end of Observing Run 3 (O3), AdV's BNS range increased from 30 Mpc to 60 Mpc, corresponding to a observable volume improved by a factor 8! That is why improving the sensitivity is a critical work.

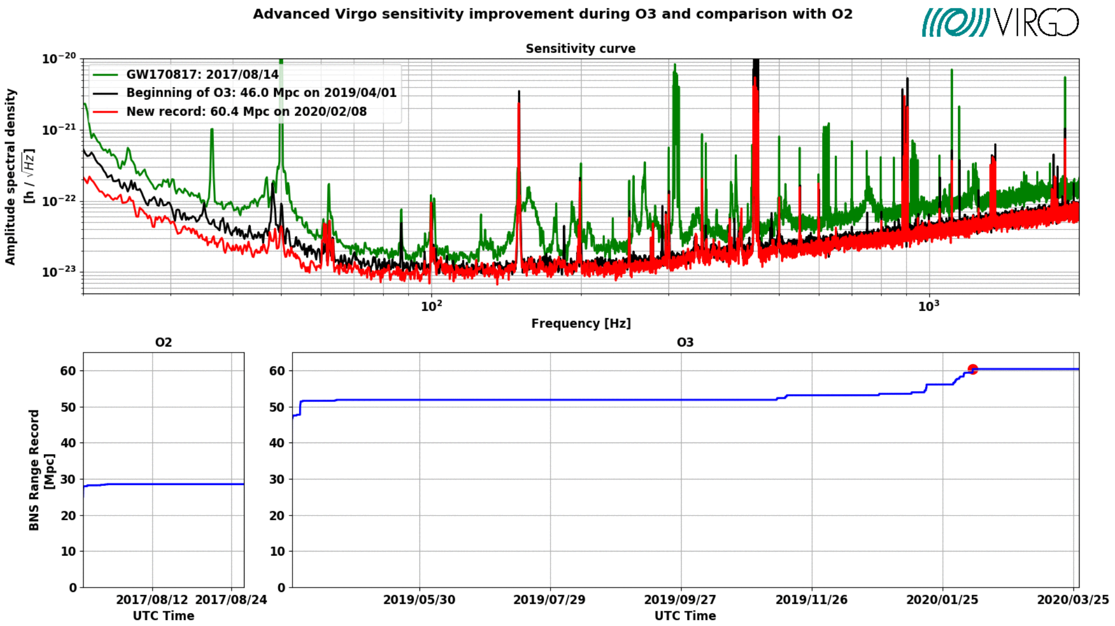

Figure 2.3: AdV's sensitivity. In the upper part, the sensitivity in terms of ASD at three different moments: in green, on 14 August 2017 (first triple-detector detection during O2); in black, on 1 April 2019 (beginning of O3); in red, the record. In the bottom part, the sensitivity in terms of BNS range vs time: O2 and O3 periods are shown. Credits: Virgo Collaboration.

The three main sources of fundamental noises are: the quantum noise — which comprises both the shot noise and the radiation pressure noise — the seismic noise, and the thermal noise.

Shot noise

The *photon shot noise* comes from the quantum nature of the photons. In other words, although the Michelson equations are solved considering the wave nature of the light, photons are actually particles that reach the photodiode following a Poisson distribution. The number of photons N_{det} detected on the photodiode during Δt is

$$N_{\text{det}}\,\hbar\,\omega_0 = P_{\text{det}}\,\Delta t = \frac{N_{\text{det}}}{N_{\text{out}}}\,P_{\text{out}}\,\Delta t = \eta\,P_{\text{out}}\,\Delta t \tag{2.13}$$

where η is the photodiode quantum efficiency, $\hbar$ the reduced Planck constant.

The number of photons follows a Poisson distribution, then its uncertainty follows $\delta N_{\text{det}} \sim \sqrt{N_{\text{det}}}$, and finally its associated power fluctuation is

$$\delta P_{\text{det}} = \frac{\delta N_{\text{det}}\,\hbar\,\omega_0}{\eta\,\Delta t} = \sqrt{N_{\text{det}}}\,\frac{\hbar\,\omega_0}{\eta\,\Delta t} = \sqrt{\frac{\hbar\,\omega_0 P_{\text{out}}}{\eta\,\Delta t}} \tag{2.14}$$

Therefore, the power variation from a gravitational signal must be at least as high as the shot noise power fluctuation (in other words, the Signal-to-Noise Ratio (SNR) must be at least 1), which is written

$$\left|\delta P_{\text{out}}^{\text{GW}}\right| = \delta P_{\text{det}}; \tag{2.15}$$

with eqs. (2.11), (2.12) and (2.14), the smallest strain amplitude that can be detected due to the shot noise in terms of ASD (if considering Δt as the process bandwidth) comes

$$\tilde{h}_{\text{shot}}(f) = \frac{1}{4\,\pi\,L}\sqrt{\frac{\hbar\,\omega_0}{\eta\,P_{\text{in}}}} \tag{2.16}$$

Note that the shot noise is independent of the perturbation frequency. Its contribution is proportional to the square root of the laser frequency [10, 34]. Contrariwise, it is inversely proportional to both the power at the BS and the length of the arms. Hence, a way to enhance the sensitivity is either to lengthen the arms (limited by the technology feasibility and the curvature of the Earth) or to increase the laser power (limited by the radiation pressure noise that would degrade the sensitivity at low frequency, see section 2.2.1).

The shot noise for a simple Michelson interferometer can be evaluated (for a photodiode quantum efficiency of 1)

$$\tilde{h}_{\mathrm{shot}} \sim 10^{-21} \left(\frac{25\,\mathrm{W}}{P_{\mathrm{in}}}\right)^{-1/2} \left(\frac{\lambda_0}{1064\,\mathrm{nm}}\right)^{1/2} \left(\frac{3\,\mathrm{km}}{L}\right) \mathrm{Hz}^{-1/2}. \tag{2.17}$$

This value is of the same order of highest expected gravitational wave strain amplitude (see eq. (1.10)); therefore, other enhancements (introduced in section 2.2.2) are needed.

Radiation pressure noise

This noise is the displacement of the optics hit by photons; the higher the laser power, the higher the radiation pressure noise. Its contribution is proportional to $1/f^2$ as [12]

$$\tilde{h}_{\mathrm{rad}}(f) = \frac{1}{m\, f^2\, L} \sqrt{\frac{\hbar\, P_{\mathrm{in}}}{2\, \pi^3\, \lambda_0\, c}} \tag{2.18}$$

where m is the mirror mass, and f is the frequency at which L varies, or, in other words, the gravitational wave frequency. That is why this effect is much more important at low frequency. One way to decrease this effect is to make mirrors heavier. It has actually been done from Virgo (21 kg) to AdV (42 kg) [36]. This noise is potentially limiting at low frequency.

Seismic noise

One of the specificities of a Michelson interferometer used for detecting gravitational waves is that mirrors are suspended by an inverted pendulum. There are actually two reasons for such a design: (*i*) to make them behave as free-falling test masses; (*ii*) to insulate them from seismic noise. Indeed, a pendulum acts as a low-pass filter, more precisely as a second order integrator (in $1/f^2$). This implies that high frequencies are quickly cut off, but seismic noise usually occurs at low frequency. Hence, the very complex design of the so-called *Superattenuators (SAs)* (see fig. 2.4). The rejection factor is 10^{14} above 10 Hz.

Thermal noise

There are two different thermal noises: the suspension thermal noise and the mirror thermal noise. Both of them are due to a Brownian motion. For the suspensions, the noise is attenuated by the intrinsic low-pass filter of the pendulum above its resonance frequency. For the mirrors, the coating noise is distributed all over the surface. Hence, either increasing the size of the mirrors or the size of the beam, are ways to decrease it; from Virgo to AdV, the beam size has been increased from about 2 cm to 5 cm [36].

The thermal ASD for a given object (suspensions or mirrors) is [11]

$$\tilde{h}_{\mathrm{th}}(f) = \sqrt{\frac{k_B\, T\, f_{\mathrm{res}}^2}{2\, \pi^3\, m\, Q\, f} \frac{1}{(f^2 - f_{\mathrm{res}}^2)^2 + \frac{f_{\mathrm{res}}^4}{Q^2}}} \tag{2.19}$$

where k_B is the Boltzmann constant, T the object's temperature, Q its quality factor (Q factor), and f_{res} its resonant frequency (the object is considered as a oscillator). From this equation, one can justify the choice of heavy mirrors with high Q factors[4]. Furthermore, it shows its band-pass

---

[4] However, as chapter 3 will show, high Q factor tend to increase the very kind of instability on which this thesis focuses.

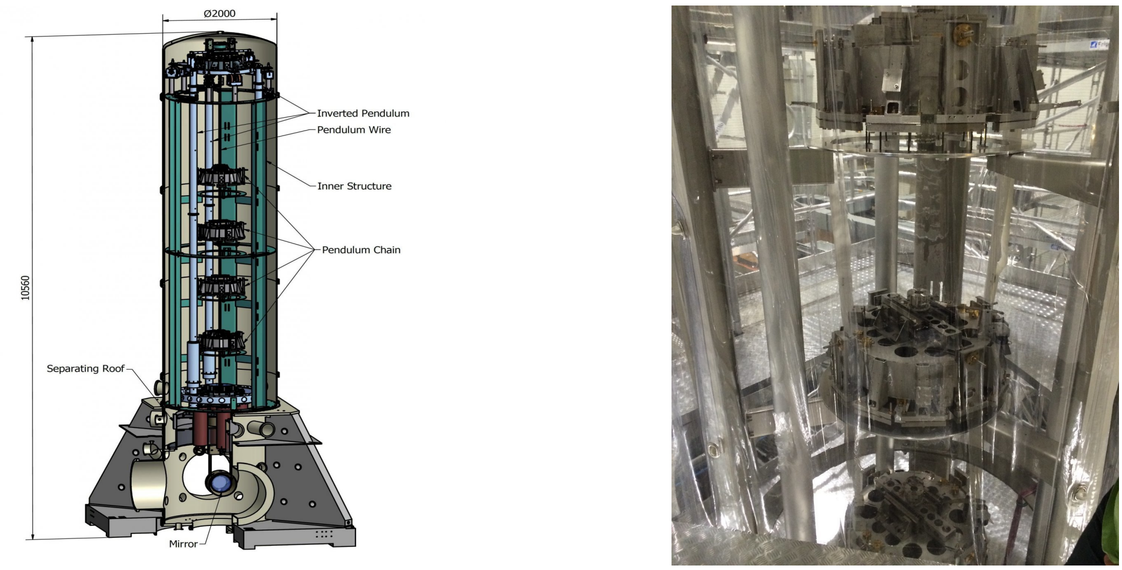

Figure 2.4: On the left: sketch of an AdV mirror SA. The Virgo suspension is about 8 meter high and is placed in a vacuum tank. It is composed of a series of pendulum that reduce the horizontal seismic vibrations that reach the mirrors. Horizontal vibration dampers are also visible. The last suspended element is a mirror payload. On the right: photograph of a SA. Three pendulums are visible. The wire used to suspend one to each other is also visible. Credits: Virgo Collaboration.

filter behaviour — the higher the Q factor, the narrower the bandwidth — in order that these noises be dominant in the medium frequency range.

Noise budget

The knowledge of all noise source ASDs enables to plot what is called the *noise budget* that allows to determine the detector's sensitivity by looking at uncorrelated sum of fundamental noise contribution. In fig. 2.5, AdV's sensitivity, accounting the main components of the noise budget. One can see that the sensitivity is limited by the suspension thermal noise at low frequency and by the quantum noise at high frequency and the coating thermal noise in the middle.

2.2.2 Improving the sensitivity

Equation (2.12) and eq. (2.16) show that the detected power variation can be increased by the same means as to decrease the shot noise: increasing the input power and lengthening the arms. The former can bring about troubles to keep the laser stable, and an increase of the radiation pressure. The latter is mainly limited by the curvature of the Earth. Down here are explained three technical solutions used in interferometric gravitational-wave detectors to bypass these limits.

Arm Fabry-Perot Cavities

A technical solution to lengthen the optical path while maintaining the actual length of the arms is to implement an optical cavity in the arms. Such a cavity is compounded of two mirrors on the axis: the input one is partially reflective and the end one is almost totally reflective. Light is stored inside cavities because the resonant frequency travels round trips between the two mirrors. These optical cavities are traditionally called *Arm Fabry-Perot Cavities (AFPCs)* within the Virgo Collaboration, although their mirrors are not plane. Hence, the reader may encounter both 'AFPC' and 'arm cavity' in the following.

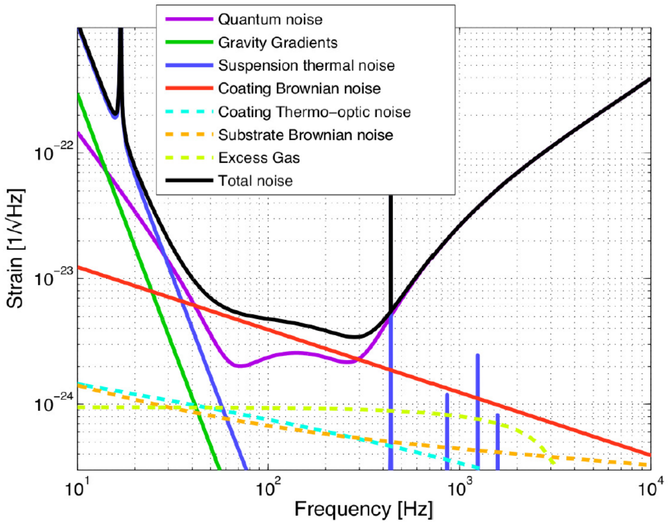

Figure 2.5: AdV's designed noise budget. Image from [36].

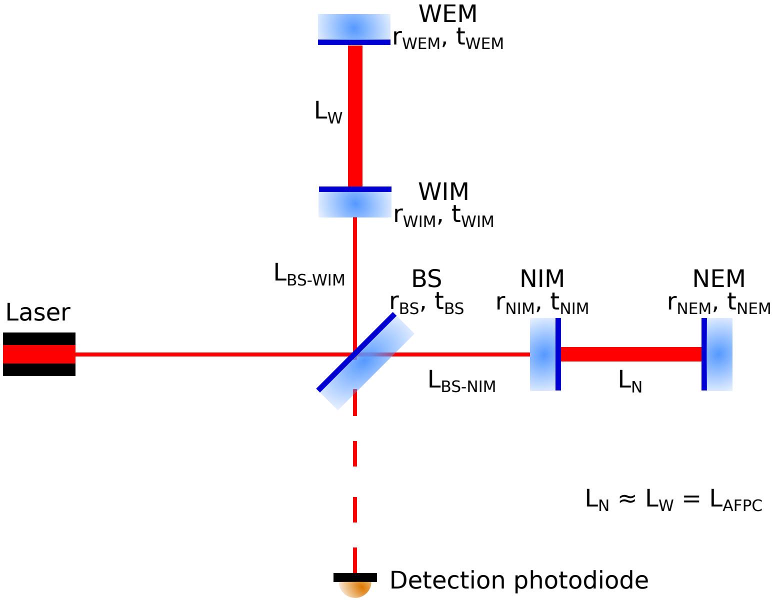

Figure 2.6: Schematic of a Michelson interferometer with arm cavities.

The number of round trips is proportional to the *finesse* of the arm cavity, which is defined as [11]

$$\mathcal{F} \approx \frac{\pi\sqrt{r_{\text{IM}} r_{\text{EM}}}}{1 - r_{\text{IM}} r_{\text{EM}}} \tag{2.20}$$

where $r_{\text{IM,EM}}$ are respectively the reflectivities of the IM and the EM, as shown in fig. 2.6. Further details on the finesse will be given in chapter 5; for now, let us rather consider only the effect of the arm cavities on the detection.

By travelling round trips down the L_{AFPC}-long arm cavities, the optical path is increased by a factor G_{AFPC} as [37]

$$G_{\text{AFPC}} = \frac{2\mathcal{F}}{\pi}. \tag{2.21}$$

In the case of AdV, the arm cavity finesse is about 450, yielding

$$\boxed{G_{\text{AFPC}} \approx 300.} \tag{2.22}$$

that is, the effective arm length is slightly less than 1000 km. Then, the light acquires an extra phase $\delta\phi_{\text{AFPC}}$

$$\delta\phi_{\text{AFPC}} = 2\, k\, G_{\text{AFPC}}\, \delta L_{\text{AFPC}} \tag{2.23}$$

However, in order to mimic the passage of a gravitational wave, let us consider the motion of an End Mirror at frequency f; thus, the phase difference can be rewritten [12]

$$\delta\phi_{\text{AFPC}} = 2\, k\, G_{\text{AFPC}} \frac{1}{\sqrt{1 + \left(\frac{f}{f_c}\right)^2}}\, \delta L_{\text{AFPC}}, \tag{2.24}$$

$$f_c = \frac{c}{4\, \mathcal{F}\, L_{\text{AFPC}}}. \tag{2.25}$$

The optical phase is then increased by the factor G_{AFPC}. Furthermore, the arm cavity acts as a low-pass filter, with a cutoff frequency f_c. For AdV, $f_c \sim 50\,\text{Hz}$.

One can model the new Michelson interferometer as a basic one, as seen in fig. 2.1, for which the two end mirrors have now complex reflection coefficients [12]

$$r_{\text{AFPC}} = \rho_{\text{AFPC}}\, e^{i\delta\phi_{\text{AFPC}}}, \tag{2.26}$$

$$\rho_{\text{AFPC}} = \left| \frac{r_{\text{IM}} - \left(r_{\text{IM}}^2 + t_{\text{IM}}^2\right) r_{\text{EM}}}{1 - r_{\text{IM}}\, r_{\text{EM}}} \right| ; \tag{2.27}$$

therefore, the output power is like in eq. (2.2), taking account of the new complex reflection coefficients. By substituting eq. (2.24) in eq. (2.12), it yields

$$\delta P_{\text{GW}} = -\frac{P_{\text{in}}}{2} \sin\left(\Delta\phi_0\right) G_{\text{AFPC}} \frac{2\, k\, h\, L_{\text{AFPC}}}{\sqrt{1 + \left(\frac{f}{f_c}\right)^2}} \tag{2.28}$$

The detection power change due to the passage of a gravitational wave is now multiplied by G_{AFPC} but is attenuated at high-frequency gravitational waves. Similarly, the resulting shot noise is given by [38]

$$\tilde{h}_{\text{shot}} = \frac{1}{4\, \pi\, G_{\text{AFPC}}\, L_{\text{AFPC}}} \sqrt{\frac{\hbar\, \omega_0}{\eta\, P_{\text{in}}}} \sqrt{1 + \left(\frac{f}{f_c}\right)^2} \tag{2.29}$$

On the one hand, the arm cavities tend to decrease the shot-noise-limited sensitivity by the factor G_{AFPC}, but, on the other hand, they add a linear dependency with respect to the gravitational wave frequency when $f \gg f_c$. Hence, it becomes a major source of noise at high frequencies, as shown in fig. 2.5.

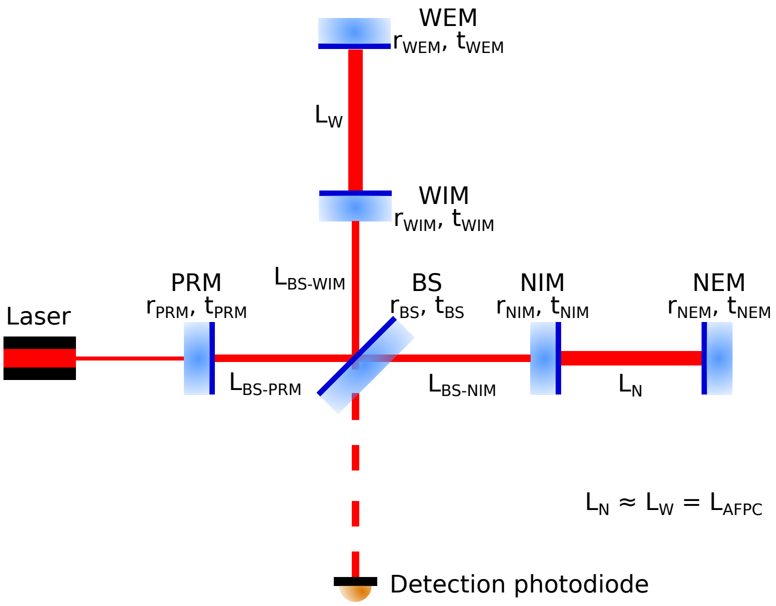

Figure 2.7: Schematic of a Michelson interferometer with arm cavities and the PRC. This is AdV's O3 configuration.

Then, looking at eqs. (2.21), (2.28) and (2.29), one can see that the finesse should be as high as possible. Nevertheless, one must keep in mind that a too high finesse would shrink the cavity linewidth, implying that the length would have to be much more accurately controlled [34]. That being said, this enhancement decreases the shot noise limit approximately by a factor 300:

$$\tilde{h}_{\mathrm{shot}} \approx 10^{-23}\sqrt{1+\left(\frac{f}{f_c}\right)^2}\left(\frac{25\,\mathrm{W}}{P_{\mathrm{in}}}\right)^{-1/2}\left(\frac{\lambda_0}{1064\,\mathrm{nm}}\right)^{1/2}\left(\frac{3\,\mathrm{km}}{L_{\mathrm{AFPC}}}\right)\mathrm{Hz}^{-1/2} \tag{2.30}$$

Power Recycling Cavity

According to eq. (2.12), the most optimised working point is the grey fringe. However, due to the photon shot noise (see section 2.2.1), the best sensitivity is obtained when the configuration is close to the *dark fringe* [11,39], which causes all the power to return towards the symmetric port [5]; this power is no longer used within the interferometer. Therefore, adding a semitransparent mirror at the symmetrical port (see fig. 2.7) significantly increases the circulating power in the interferometer by recycling all this power; hence its name: *Power Recycling Mirror (PRM)*. Considering the rest of the interferometer as equivalent to a mirror of reflectivity r_{MICH} (which is then supposed to be around 1), the PRM comes to create an extra resonant cavity, the *PRC*, whose optical gains is defined as [39]

$$G_{\mathrm{PRM}} = \left(\frac{t_{\mathrm{PRM}}}{1 - r_{\mathrm{PRM}}\, r_{\mathrm{MICH}}}\right)^2 \tag{2.31}$$

where t_{PRM} and r_{PRM} are respectively the transmission and the reflection coefficients of PRM. The detected power is multiplied by this factor G_{PRM}. Then the resulting shot noise is

$$\tilde{h}_{\mathrm{shot}} = \frac{1}{4\,\pi\, G_{\mathrm{AFPC}}\, L_{\mathrm{AFPC}}}\sqrt{\frac{\hbar\,\omega_0}{G_{\mathrm{PRM}}\,\eta\, P_{\mathrm{in}}}}\sqrt{1+\left(\frac{f}{f_c}\right)^2} \tag{2.32}$$

---

[5] The EMs have a reflective coefficient close to one, therefore the transmission losses in the arm cavities are very small.

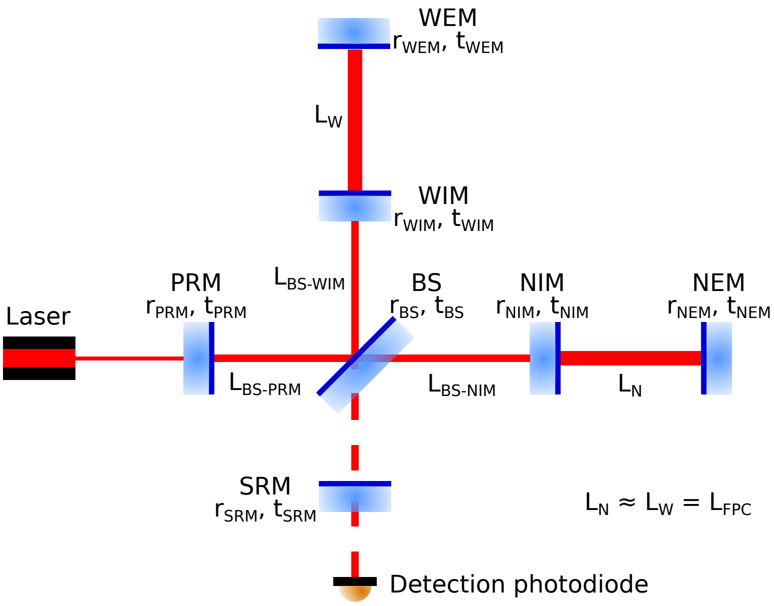

Figure 2.8: Schematic of a Michelson interferometer with arm cavities, the PRC, and the SRC. This will be AdV's O4 configuration.

The sensitivity is improved by a factor $\sqrt{G_{\mathrm{PRM}}}$. AdV's G_{PRM} is

$$\boxed{G_{\mathrm{PRM}} \approx 40,} \tag{2.33}$$

Once AdV's G_{PRM} and G_{AFPC} are known, one can calculate the intracavity power. Indeed, the intracavity power $\mathcal{P}_{\mathrm{AFPC}}$ is related to the input laser power $\mathcal{P}_{\mathrm{in}}$ as

$$\mathcal{P}_{\mathrm{AFPC}} = \mathcal{P}_{\mathrm{in}} \cdot G_{\mathrm{PRM}} \cdot \frac{1}{2} \cdot G_{\mathrm{AFPC}}, \tag{2.34}$$

where the factor 1/2 comes from the BS. Then, for AdV, one can write

$$\boxed{\mathcal{P}_{\mathrm{AFPC}} \approx 6000\, \mathcal{P}_{\mathrm{in}}.} \tag{2.35}$$

Signal Recycling Cavity

At dark fringe, the PRM is actually impinged only by the common field, which is obviously the main part of the recombined field. Yet, a remaining differential field arrives to the detection photodiode. By tuning this signal, one can shape the sensitivity and, thus, improve it at specific frequency ranges, chosen for detecting signals of specific events. This can be achieved by adding again an extra mirror — the Signal Recycling Mirror (SRM) giving birth to the SRC — but on the antisymmetric port this time (see fig. 2.8).

In AdV's current configuration (which is the one of O3), the arm cavities and the PRM are installed and made detections possible. The installation of the SRM is foreseen for the next Observing run, O4, which should start in mid-2022.

Squeezing

The squeezing is a technical solution to beat the standard quantum noise. On an amplitude-phase diagram, a coherent light (from a laser for instance) is represented by a circle, whose area describes the Heisenberg uncertainty. While keeping the same area — that is to say the same uncertainty — it is possible to decrease the phase uncertainty, but the amplitude uncertainty will be increased:

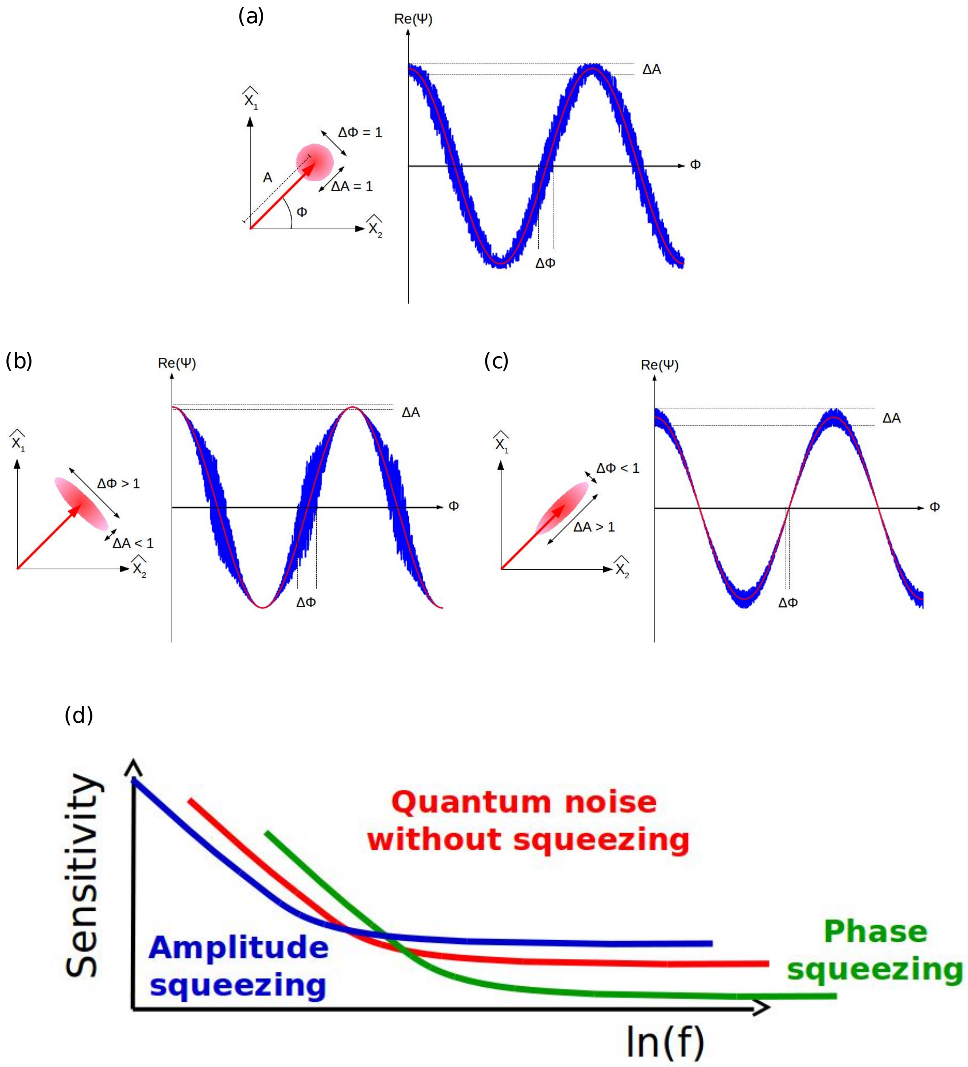

Figure 2.9: (a) Coherent light. (b) Amplitude squeezing. (c) Phase squeezing. (d) Representation of advantages and drawbacks of each type of squeezing. Credits: Angélique Lartaux-Vollard, IJCLab, from [20].

this is the phase squeezing. The opposite is also possible: the amplitude squeezing. The phase squeezing improve the sensitivity at low frequency, while the phase squeezing improve it at high frequency. All of this is summarised in fig. 2.9. For further information about squeezing for AdV, please refer, for example, to [20, 40, 41].

2.2.3 From Virgo to Advanced Virgo

Increasing the laser beam size to decrease the thermal noise, or increasing the mirror mass to decrease both the thermal noise and the radiation pressure noise have already been introduced. Here are summarised other enhancements done from Virgo to AdV, which was designed to improve its sensitivity by one order of magnitude. Its optical design is given in fig. 2.10.

The AdV column in table 2.1 gives the designed parameters; as we shall see, some have actually not been reached.

From the whole configuration aspect, the SRC was already planned for AdV but will finally

Parameters	**AdV design**	**Initial Virgo**
Sensitivity		
BNS range	134 Mpc	12 Mpc
Instrument topology		
Power enhancement	Arm cavities and Power Recycling	Arm cavities and Power Recycling
Signal enhancement	Signal Recycling	n.a.
Laser and optical powers		
Laser wavelength	1064 nm	1064 nm
Optical power at laser output	> 175 TEM$_{00}$ W	20 W
Optical power at interferometer input	125 W	8 W
Optical power at mirrors	650 kW	6 kW
Optical power at BS	4.9 kW	0.3 kW
Test masses		
Mirror material	fused silica (FS)	FS
Mirror diameter	35 cm	35 cm
Mirror mass	42 kg	21 kg
BS diameter	55 cm	23 cm
Mirror surfaces and coatings		
Coating material	SiO_2	SiO_2
Mirror radii of curvature	IM: 1420 m EM: 1683 m	IM: flat EM: 3600 m
Beam radius at IM	48.7 mm	21 mm
Beam radius at EM	58 mm	52.5 mm
Arm cavity finesse	443	50
Thermal compensation		
Thermal actuators	CO_2 lasers and Ring Heater (RH)	CO_2 lasers
Actuation points	Compensation Plates (CPs) and directly on mirrors	Directly on mirrors
Suspensions		
Seismic isolation system	SA	SA
Test mass suspensions	FS fibres	Wires
Lengths		
Arm cavity length	3 km	3 km
PRC	11.952 m	12.053 m
SRC	11.952 m	n.a.

Table 2.1: Some main parameters of the AdV Reference Design [36].

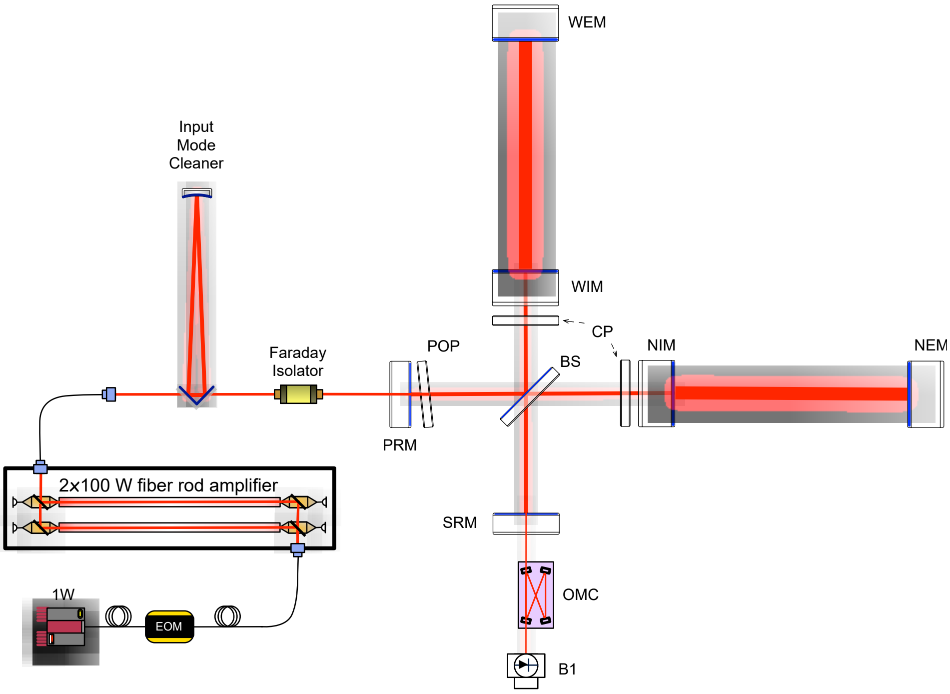

Figure 2.10: AdV's optical design. Image from [36].

be ready for AdV+ phase I, that is, for O4. Regarding the laser power, the interferometer input power was planned to be increased up to 125 W, while it eventually reached 27 W for Observing Run 3b (O3b).

Regarding the optical design, not only was increased the mass of the mirrors and the radius of the beam impinging them, but also the radii of curvature of the mirrors were modified, which directly affects the stability condition of the interferometer (see section 5.3.1). The PRC length needed to be retuned, setting, thus, the interferometer configuration closer to instability [38]. As well, the arm cavity finesse was strongly enhanced by almost a factor 10, which proportionally improved the sensitivity (see section 2.2.2).

Another AdV's important enhancement regarding this thesis topic are the Ring Heaters. They enable the tuning of the radii of curvature of the mirrors by heating them. I shall show how they are important for our study.

2.3 A detector network

To date, five ground-based detectors work all together within the three following collaborations: the *LIGO Scientific Collaboration (LSC)*, the *Virgo Collaboration*, and the *Kamioka Gravitational Wave Detector (KAGRA) Collaboration*.

The LSC is constituted of the LIGO Hanford Observatory (LHO) (Hanford site, Washington, USA), the LIGO Livingston Observatory (LLO) (Livingston, Louisiana, USA), and GEO600 (Sarstedt, Hildesheim, Lower Saxony, Germany). The arms of the two first ones are 4 km long, whereas those of GEO600 are only 600 m, which make it not sensitive enough to properly detect gravitational wave signals. However, it is still in use for engineering tests and coherence between the signals of the whole network. The LSC is also planning to build a new detector in India within a decade.

The Virgo Collaboration is constituted of the Virgo detector, on the EGO site (Santo Stefano a Macerata, Cascina, Tuscany, Italy). It has 3-kilometre arms.

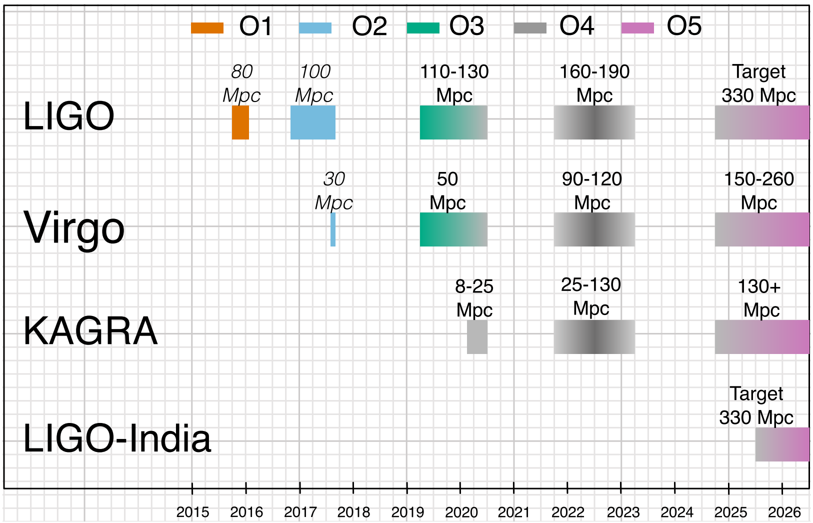

Figure 2.11: Planned sensitivities for LIGO, Virgo, KAGRA, and the foreseen LIGO-India. Image from [42].

The KAGRA Collaboration is constituted of the KAGRA detector (Kamioka mine, Gifu Prefecture, Japan). It has 3-kilometre arms.

The main goal of having a network of detectors is to improve the general sensitivity, have coincidence detections, and help localise the source. Moreover, as the bisector of interferometer arms is a blind zone, having some detectors misaligned from one another could allow to scan the whole sky.

2.4 Operation and detections

Any detector faces various phases during its life: upgrade, commissioning, and observation. The observation periods are called *Observing runs*. Between each of them, detectors experience upgrades and commissioning phases, during which various activities are performed to improve the detectors. A general view of the different phases for each detector can be seen in fig. 2.11. This figure also shows the increase of sensitivity from an observing run to another.

Without the improvements introduced in section 2.2.2, the detection of gravitational wave signals, for any type of source, would have been impossible. Each commissioning phase helps gain more sensitivity, which in turn allows to detect much further or weaker sources. Thanks to this work, GW150914 the first direct observation was made on 14th September 2015 (during Observing Run 1 (O1))[6] by the two aLIGO detectors [43]. It was the first event of the coalescence of Binary Black Holes (BBH) ever observed. Each black hole had a mass of about $30\,\mathrm{M}_\odot$ each. The 'chirp' shape (see section 1.2.2) of the signal can be seen in fig. 2.12. First, at the very beginning, the signal is hidden by the noise as the strain amplitude is really weak. Then, the two black holes are getting closer to each other, increasing both the amplitude and the frequency of the signal, whose maximums corresponds to the merging. Finally, the two black holes form another more massive and is no longer in motion; hence, the signal stops. The interesting part of the signal is rather close to the numerical prediction because the SNR was 25, which is really high. The detected signal is the few last milliseconds of a spiralling phase that lasted millions of years.

During the whole O1 from 12th September 2015 to 19th January 2016, the LIGO-Virgo observed three BBH mergers.

---

[6] Gravitational wave events are always labelled 'GW' directly followed by the observation date in YYMMDD format.

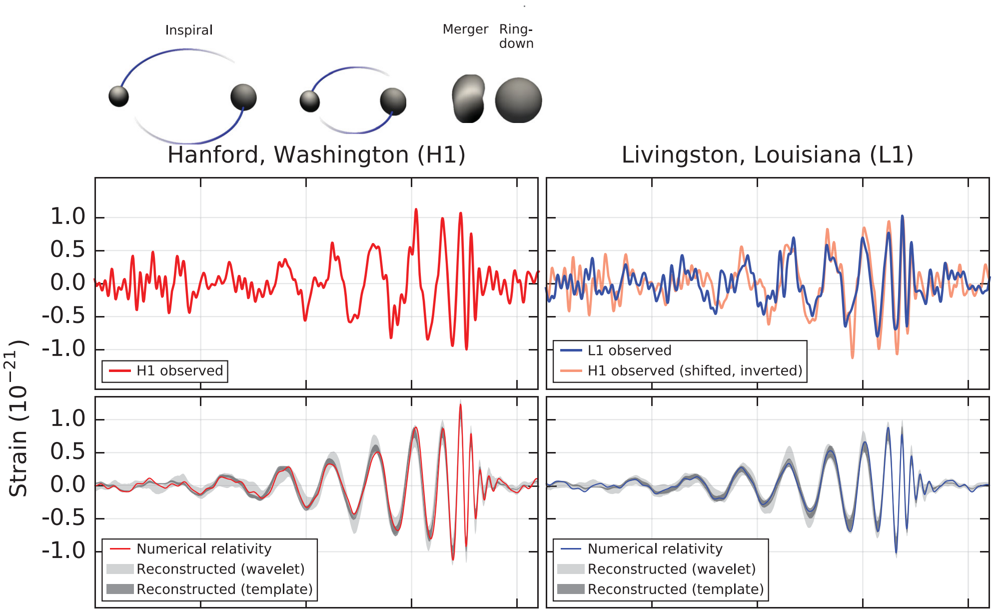

Figure 2.12: The gravitational wave event GW150914 observed by the LHO (H1, left column panels) and LLO (L1, right column panels) detectors. Top row: band limited filtered aLIGO data. Bottom row: reconstructed signal and numerical prediction.

Then, O2 started on 30th November 2016 and ended on 25th August 2017. Virgo joined LIGO on 1st August 2017. Virgo demonstrated its capability of detecting gravitational waves, seeing that during that very short period of time, all the three detectors observed four gravitational wave events: GW170814 was the first three-detector observation [44] (see fig. 2.13), and GW170817 was the first detection of a BNS merger and the first detection of an electromagnetic counterpart [45]. In total, O2 cumulated eight detections. All the O1 and O2 detections are summarised in the catalogue of O1 and O2 [46].

O3 was separated into two subruns: Observing Run 3a (O3a) from 1st April 2019 to 1st October 2019, and O3b from 1st November 2019 to 27th March 2020. In total, thirty-nine observations were done during O3a, of which only one is certified to be a BNS. They are all summarised in the catalogue of the first half of O3 [47].

Among the O3 detections, three are of further interest. The first one, GW190412 could be the first observation of a merger of two black holes of very distinct masses [48]. The second, GW190425 is the first confirmed gravitational wave detection based on data from a single observatory; it is the second confirmed BNS, whereas no electromagnetic counterpart was found. Note that the total mass exceeds that of known galactic neutron star binaries [49]. The last one, GW190521 is the most massive gravitational wave binary observed to date: the two black holes had masses of about 85 and 66 $\mathrm{M}_\odot$, resulting into an remnant black hole of 142 $\mathrm{M}_\odot$. Also, it is considered as the first clear detection of an ‘intermediate-mass’ black hole [50].

All of these detections have provided us with confirmation on the expected rate of BBH mergers, $\gtrsim 1\,\mathrm{Gpc}^{-3}\,\mathrm{yr}^{-1}$ [51], a better understanding of BBHs population [51, 52], a better limit to the mass of the graviton [7] $m_g \leq 7.7 \times 10^{-23}\,\mathrm{eV}\,c^{-2}$, a first direct evidence of a link between BNS mergers and short gamma-ray bursts [45], a better understanding of BNS mergers [45], and a higher precision in constraining the Hubble constant [53].

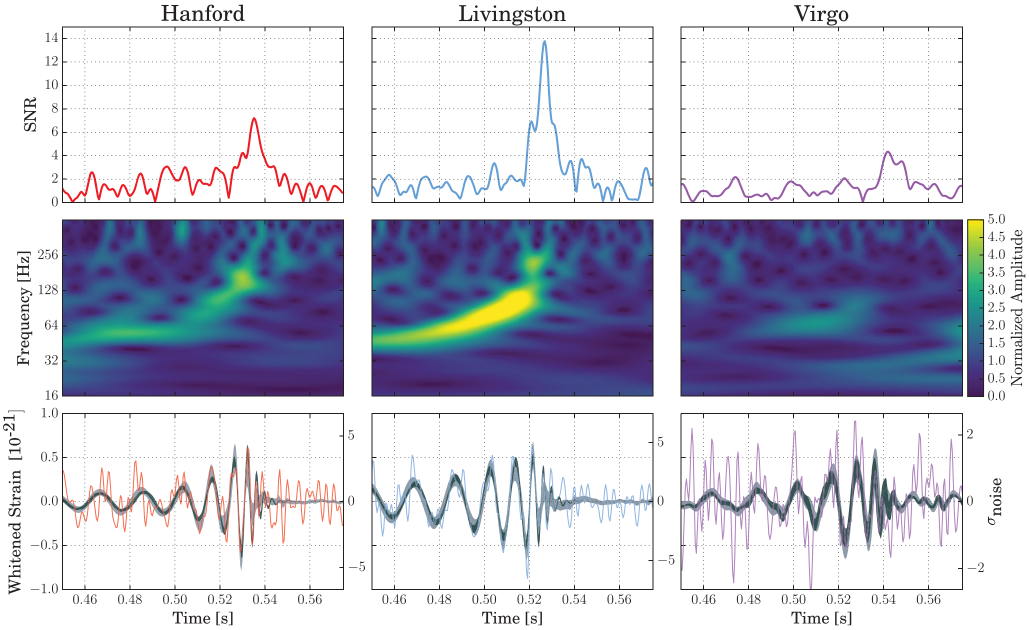

Figure 2.13: The gravitational wave event GW170914. First triple-detector observation.

Chapter 3

Optomechanical parametric instability

This chapter chiefly describes a worrisome nonlinear effect encountered within arm cavities, then also occurring in the two arms of an interferometric gravitational-wave detector. This effect comes from the coupling of three modes: a mirror acoustic mode that sets the mirror surface in motion, the fundamental optical mode of the optical cavity (TEM_{00}), and an optical higher-order mode (HOM). Hence, there are numerous ways of calling this phenomenon: *parametric (oscillatory) instability*, *three-mode parametric instability*, or **optomechanical parametric instability (OPI)**. In the following, we will use the last one as it better describes the phenomenon.

Before going further into details, let us summarise here *how* this effect appears, *what* it implies, and *why* studying it for Advanced Virgo (AdV) matters.

Photons can be scattered from the TEM_{00} to an HOM through the mechanical mode by annihilating or creating one phonon in this mode. These photons can generate an optical beat note if the difference in frequencies of the two optical modes is equal to the resonant frequency of a structural mechanical mode. This beat note, in turn, can either damp or increase the mechanical motion via radiation pressure [54]. The latter effect leads to an exponentially growing amplitude of the mechanical mode, which then reaches a plateau after some time. The signal associated with this mirror mechanical excitation could saturate the electronics, hence the control of the interferometer would be lost [55].

During Observing Run 1 (O1), in 2015, Advanced LIGO (aLIGO) observed an OPI when a mirror mechanical mode at 15 kHz became unstable, for an intracavity power of 50 kW [56]. A similar phenomenon was expected to occur in AdV, especially since AdV's intracavity power was already much higher than that of aLIGO. It eventually happened on 7th January 2020. The purpose of this work is to investigate possible OPIs within AdV.

As a first step, a pedagogical introduction — both historical and physical — of the OPIs is given. Second, a section recalls the two OPIs that were observed: one in the aLIGO and the other one in AdV. Then, the parametric gain of the OPI is introduced.

3.1 Introduction

In chapter 2 were introduced the two quantum noises that limit the detector sensitivity: the *photon shot noise* and the *radiation pressure noise*. The former is the main limitation from 100 Hz on; that is why it needs to be reduced. To do so, according to eq. (2.16), one can increase the intracavity power. For example, from Observing Run 3a (O3a) to Observing Run 3b (O3b), the AdV input power was increased from 18.5 W to 27 W. Then, as a rough estimation — not taking into account the frequency dependence of the noise — the photon shot noise was decreased by a factor $1-\sqrt{\frac{18.5}{27}} \approx 0.17$. On the other hand, increasing the intracavity power increases the radiation pressure contribution (eq. (2.18)), and may cause nonlinear coupling effects.

These types of nonlinear coupling have been studied, mostly since the 1960s with the advent of lasers. Among them is the Mandelstram-Brillouin scattering [57, 58], which is the interaction of light with various material waves of the crossed medium, such as mass oscillations via energy transfer to phonons. The process leading to OPIs is really close to that of the Mandelstram-Brillouin scattering [59]: in an optical cavity, a photon of frequency ω_0 from the fundamental mode (the *carrier*) is scattered into a photon of lower frequency ω_1 (another optical cavity mode), and a phonon of frequency ω_m; this phonon being an excitation of a mirror mechanical mode. The energy conservation writes

$$\hbar\omega_0 = \hbar\omega_1 + \hbar\omega_m. \tag{3.1}$$

This process is shown in fig. 3.1(a). As the scattered photon has less energy than the absorbed one, this process is called a Stokes process. The *beat note* between the two optical fields yields a radiation pressure oscillation at the difference frequency $\omega_0 - \omega_1 \approx \omega_m$, which drives the mechanical mode. In turn, the mechanical mode interacts with the optical fundamental mode and intensifies the photon scattering process. If the fundamental mode intensity reaches a certain threshold [59], the nonlinear coupling between the three modes yields a parametric instability: the OPI. The populations of the different energies with respect to the laser power are shown in fig. 3.2.

Note that the reverse process, that is to say the *anti-Stokes process*, for which the scattered photon has a higher energy than the carrier one ($\hbar\omega_1 = \hbar\omega_0 + \hbar\omega_m$) is possible. Contrary to the previous heating process, it takes energy from the acoustic mode, thus damping it. Figure 3.1 shows these two possible irradiations of the Mandesltram-Brillouin scattering.

Braginsky et al. were the first to show the impact of OPIs within an arm cavity in [54], but they did not take the anti-Stokes process into account. Kells and D'Ambrosio [60] showed that taking it into account can substantially reduce or even suppress an OPI. Note that they considered only the longitudinal TEM$_{00}$ modes. Inasmuch as all TEM$_{00}$ modes are separated by the Free Spectral Range (FSR), the Stokes and the anti-Stokes waves are equidistant to the carrier and the anti-Stokes wave compensates the Stokes one. If one takes into account the HOMs, as they are not symmetrically distributed (see fig. 3.3), they may not have a suitable anti-Stokes mode [61].

In definitive, OPIs can occur because they are not self-compensated and must then be studied for the sake of gravitational-wave detections; and this study must include the anti-Stokes processes.

Eventually, both aLIGO and AdV have experienced such instabilities: aLIGO in 2015 [56] and AdV in 2020.

3.2 Optomechanical parametric instability observations

3.2.1 At LIGO

The first observation of a self-sustaining OPI in a gravitational-wave detector was made in aLIGO at the LIGO Livingston Observatory (LLO) [56]. The unstable mechanical mode was identified

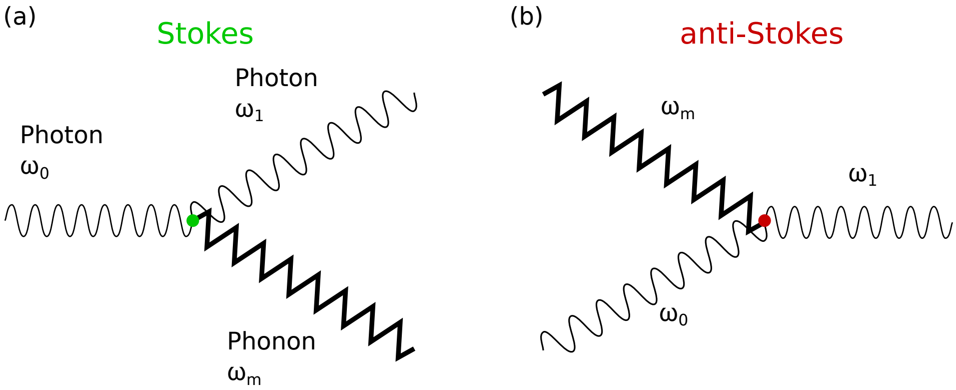

Figure 3.1: (a) Stokes irradiation: emission of a phonon $\omega_0 = \omega_1 + \omega_m$. (b) Anti-Stokes irradiation: absorption of a phonon $\omega_0 = \omega_1 - \omega_m$. Image created by Daniel Schwen `http://commons.wikimedia.org`, modified, under the terms of the Creative-Commons-License CC-BY-SA-2.5.

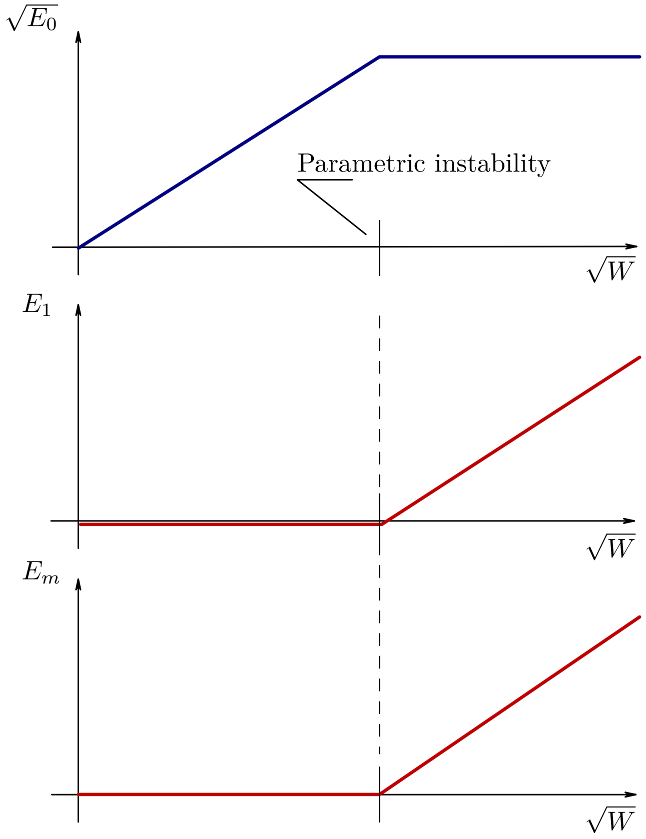

Figure 3.2: Energy in the fundamental mode E_0, energy in the Stokes E_1, and energy in the mechanical mode E_m with respect to the laser power W, below and above the OPI threshold. Image adapted from [59].

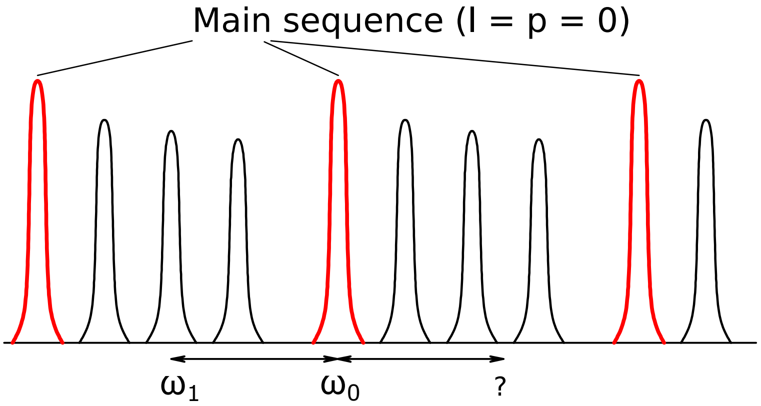

Figure 3.3: Schematic structure of optical modes in an optical cavity. The main sequence (higher peaks in red) contains all the fundamental modes spaced by the Free Spectral Range: a Stokes mode on the main sequence always have a suitable anti-Stokes mode. Which is not obviously the case for a Stokes mode at ω_1, whose anti-Stokes mode is represented by the question mark. Image adapted from [59].

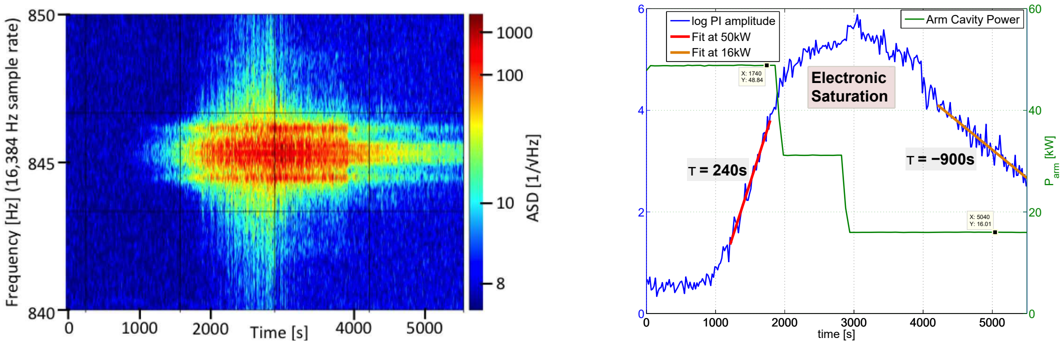

Figure 3.4: On the left, a time-frequency diagram of the ASD of LIGO's primary output, that is, the gravitational wave strain channel. The growing instability appears around 845 Hz. It eventually saturates the electronics between 2000 s and 4000 s. On the right, the amplitude of the image on the left, together with two fits with different values of the intracavity power to find the growth (or decay) time-scale. Images from [56].

as a 15.54 kHz mechanical mode of the arm cavity mirrors, and the involved optical mode was an order 3. The arm intracavity power was 50 kW. The instability gave rise to an electronic saturation of the detection signal. The two images of fig. 3.4 show the exponential growth and the electronic saturation. In fig. 3.4(b), one can calculate the e-folding growth (or decay) time τ_m, which enables to retrieve the parametric gain R_m (explained in section 3.3) and the *quality factor (Q factor)* of the mechanical mode thanks to the following relation

$$\tau_m = \frac{2\,Q_m}{\omega_m\,(R_m - 1)}. \tag{3.2}$$

According to Evans et al. in [56], the observation rose an instability with an expected high gain, at an expected mechanical frequency, and with a Q factor in an expected range.

3.2.2 At Virgo

Virgo, too, observed such an instability on 7th January 2020. Until December 2019, the arm intracavity power was around 100 kW. This was twice the intracavity power at which aLIGO had faced an OPI; yet, AdV had not.

The nominal input power of AdV's Observing Run 3 (O3) configuration is 50 W, which corresponds to an intracavity power of around 300 kW. A first increase step was made in December 2019 to pass from 18.5 W to 27 W input power. Ultimately, this power increase requires a commissioning afterwards in order to keep the detector under control, which sufficiently changed AdV's configuration, getting closer to an OPI: a 155 kHz oscillation exponentially grew up until it also saturated the output electronics, as shown in fig. 3.5. We could retrieve the parametric gain of this instability, and the mechanical Q factor, thanks to the measurement of the growth time-scale. Few extra details will be given in section 6.5.2, and an article is being written [62].

The main difference with regard to the observation in aLIGO is that the OPI occurred during the locking phase and the instability directly led to a lock loss. We could not have the time to try to decrease the input power. That is why we could not obtain, in fig. 3.5, an e-folding decay like in fig. 3.4.

3.3 Parametric gain: classical feedback system method

The instability phenomenon is triggered by the thermal motion of the mirror at ω_m [55]. Starting from these considerations, Braginsky et al. developed a series of equations in [54, 61], introducing an expression for the *parametric gain* R_m. If this gain is higher than one, then the interaction

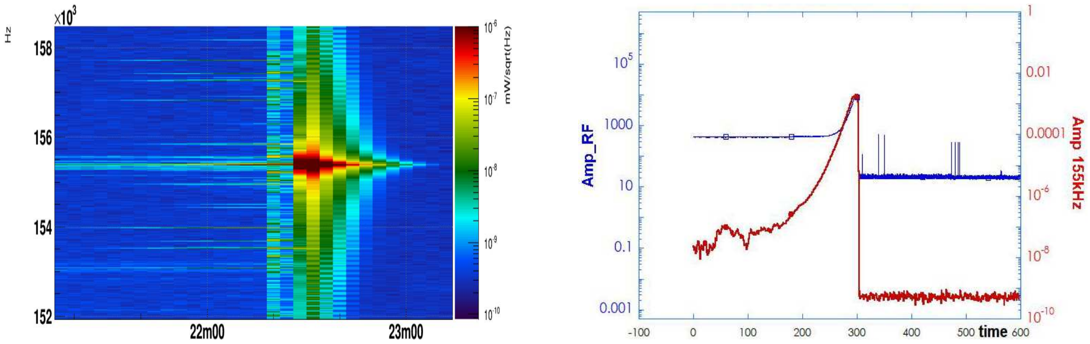

Figure 3.5: On the left, a time-frequency diagram of the ASD of Virgo's primary output, that is, the gravitational wave strain channel. The growing instability appears around 155 kHz, during the locking phase of the apparatus. It eventually saturates the electronics. On the right, the amplitude of Virgo's primary output: the blue curve is the full signal, the red curve is the contribution of only the 155 kHz signal. Images done by Paola Puppo (INFN Roma).

between those modes can lead to an OPI. The definition given by Braginsky et al. can also be found in many articles: [63–68]. In [69], this expression is generalised to sum the contributions of all the transverse optical modes.

However, our computation does not use that expression, as it is not easy to implement numerically, but rather the one from [55], whose approach is described in the following.

I describe the approach developed by Evans et al. [55] to compute the parametric gain. In this framework, the whole interaction between the three implied modes is seen as a classical feedback system. This modular approach is very suitable since it can be adapted to many different interferometer configurations with the same analytical formulas. The parametric gain of the mechanical mode m is given by

$$R_m = \underbrace{\frac{8\pi Q_{\mathrm{m}} P}{M\omega_m^2 c\lambda}}_{\text{prefactor}} \sum_{n=0}^{\infty} \left(\underbrace{\mathrm{Re}\left[G_n\right]}_{\text{optical transfer coefficient}} \times \underbrace{B_{m,n}^2}_{\text{spatial overlap parameter}} \right), \tag{3.3}$$

where Q_m is the Q factor of the mechanical mode m and ω_m its frequency, P the arm cavity optical power, λ the optical wavelength, M the mirror mass, c the velocity of light; G_n is the optical transfer coefficient of the n^{th} optical mode and encapsulates the interferometer configuration; finally, $B_{m,n}$ is the spatial overlap integral between the three involved modes. A mechanical mode is amplified if $R_m > 0$ and damped if $R_m < 0$. It becomes unstable if $R_m > 1$, that is, if the resonant excitation of the mechanical mode by the radiation pressure force overcomes the mechanical losses.

3.3.1 The prefactor

Let us just recall the linear dependence of the parametric gain on the intracavity power. As well, it is directly proportional to the mechanical mode m's Q factor. The possibility of damping an OPI by reducing the unstable mechanical mode's Q factor has been studied in [65]. Indeed, one does not design mirrors with low mechanical Q factors, in order not to increase the thermal noise (see eq. (2.19)). Therefore, this is better to keep Q factors as high as possible because the thermal noise can strongly and continuously deteriorate the detector sensitivity, while the phenomenon of OPIs happens only for certain configurations.

To lower the parametric gain, trying to build heavier optics seems to be a better solution. This has been done from LIGO (11 kg) to aLIGO (40 kg) [70], and from Virgo (21 kg) to AdV (42 kg), as shown in table 2.1. This improvement is first meant to decrease the effect of the radiation pressure (improving, thus, the sensitivity), not to lower the odds of encountering an OPI; however, the former leads to the latter.

Note that the parametric gain is inversely proportional to the square of the mechanical mode frequency. However, contrary to what was expected, even a mechanical mode of very high frequency can lead to an OPI, as experimentally demonstrated in section 3.2.2.

3.3.2 The spatial overlap parameter

The spatial overlap parameter results from the overlap integral of the the three implied modes spatial profiles. It writes

$$B_{m,n} = \iint\limits_{\mathcal{S}} f_0 f_n \left(\mathbf{u_m} \cdot \mathbf{z}\right) d\mathbf{r}_\perp, \tag{3.4}$$

where $\mathcal{S}$ is the optic's coating surface, f_0 and f_n are the field distributions of respectively the fundamental mode and the n^{th} optical mode, and $\mathbf{u_m}$ is the displacement function of the mechanical mode. The field distributions are normalised as

$$\iint\limits_{\infty} |f_n|^2 \, d\mathbf{r}_\perp = 1 \tag{3.5}$$

Figure 3.6 shows various couples of mechanical modes and optical modes, together with their associated squared spatial overlap parameters. The two first couples are arbitrarily chosen for their weak spatial overlap. The two last couples show very good spatial overlaps. A large overlap parameter is however not a sufficient condition to get an instability, the resonance condition should also be verified. This is the subject of the next paragraph.

3.3.3 The optical transfer coefficient

The optical transfer function encapsulates the cavity response to the optical fields. The two carrier sidebands corresponding to the Stokes and anti-Stokes processes have different optical transfer coefficients G_n^- (lower sideband) and G_n^+ (upper sideband). The total optical transfer coefficient G_n is defined as

$$G_n = G_n^- - \overline{G_n^+}, \tag{3.6}$$

where $\overline{G_n^+}$ denotes the complex conjugate of G_n^+.

At low power, the mirror motion due to the radiation pressure is negligible. The propagation of optical fields at different frequencies are independent and can be treated separately. At high power, the radiation pressure depends on both sidebands, and the motion induced by the radiation pressure modifies the sidebands. Hence, a classical feedback system; according to Corbitt et al. in [71], the most convenient mathematical framework for this problem is the Caves-Schumaker *two-photon formalism* [72, 73].

Evans et al. built their method on this mathematical framework to calculate the scattering matrix $S_n^{\pm}$ that contains all the transfer coefficients for the n^{th} optical mode from one port of the optical system to the next one. Therefore, the scattering matrix is a square matrix whose size is the number of all considered fields of interest.

From the scattering matrices $S_n^{\pm}$ of the two sidebands, one can derive the optical transfer coefficients

$$G_{n,x}^{\pm} = \mathbf{e}_x^T \left(I - S_n^{\pm}\right)^{-1} \mathbf{e}_x, \tag{3.7}$$

where $\mathbf{e}_x$ is the x^{th} column of the identity matrix I, and $\mathbf{e}_x^T$ its transpose. The index $x = 1, 2, ..., 12$ denotes the fields of interest of figs. 3.7 and 3.8.

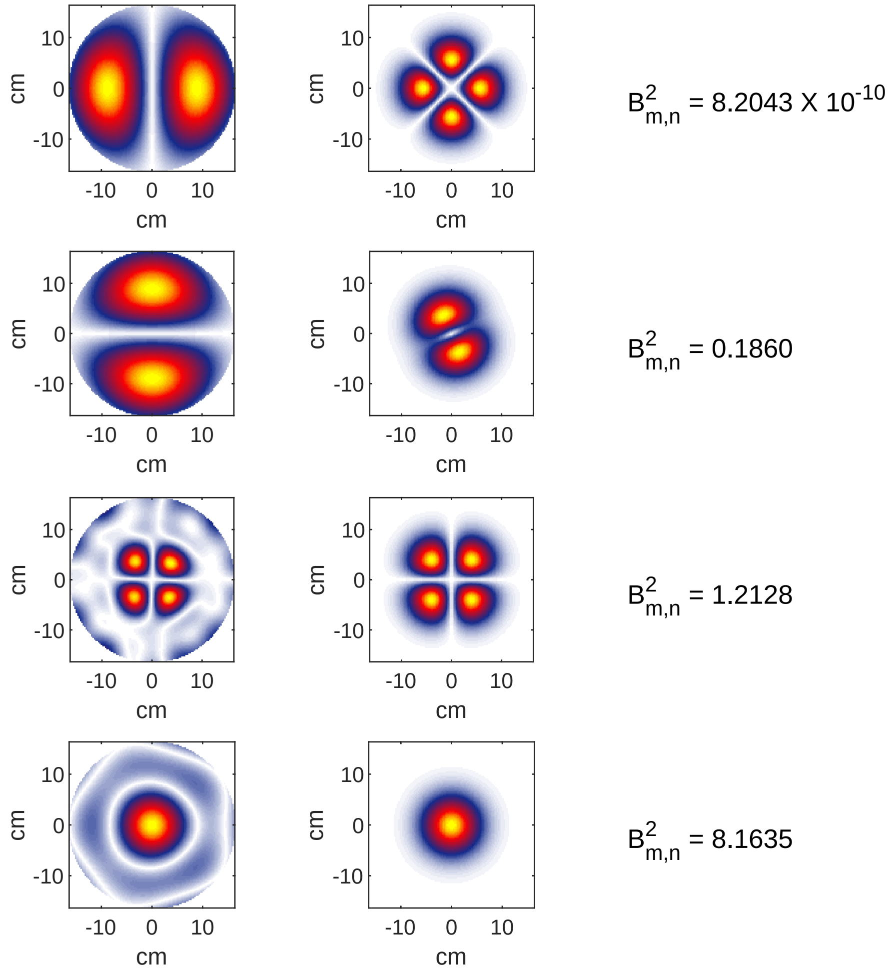

Figure 3.6: On the left, the surface displacements of various mechanical modes. In the middle, some optical modes. On the right, the associated squared spatial overlap parameters $B^2_{m,n}$. Downwards, the optical modes are respectively the FSMM(5) (order 2), the FSMM(3) (order 1), the FSMM(4) (order 2), and the FSMM(1) (order 0). The FSMM will be introduced in section 5.3.3.

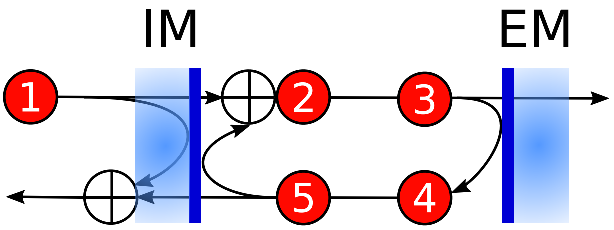

Figure 3.7: Fields of interest of an arm cavity.

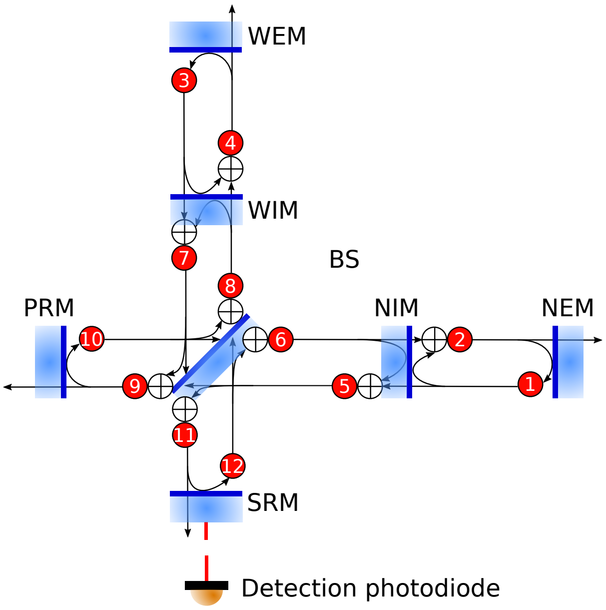

Figure 3.8: Fields of interest of a power and signal recycled of a Fabry-Perot interferometer. This is the most general configuration, that is, with a PRC, and an SRC cavity. One can 'suppress' a mirror (and thus its cavity) by setting its transmission to 1.

Single arm cavity

In the case of a single arm cavity of length L, one can use the following simpler formalism where the fields of interest are those of fig. 3.7; then, the size of the scattering matrix $S_n^{\pm}$ is 5×5 and writes

$$S_n^{\pm} = \begin{pmatrix} 0 & 0 & 0 & 0 & 0 \\ t_{\mathrm{IM}} & 0 & 0 & 0 & -r_{\mathrm{IM}} \\ 0 & p_L^{\pm} & 0 & 0 & 0 \\ 0 & 0 & -r_{\mathrm{EM}} & 0 & 0 \\ 0 & 0 & 0 & p_L^{\pm} & 0 \end{pmatrix}, \tag{3.8}$$

where t_{IM} is the amplitude transmission coefficient of Input Mirror (IM), r_{IM} and r_{EM} the amplitude reflection coefficients of the mirrors, and $p_L^{\pm}$ the propagation operator as

$$p_L^{\pm} = \exp\left[j\left(\phi_n \pm \frac{\omega_m L}{c}\right)\right]. \tag{3.9}$$

ϕ_n is the phase of the $\mathrm{n^{th}}$ HOM

$$\phi_n = \phi_0 - \psi_n, \tag{3.10}$$

where ϕ_0 is the propagation phase of the fundamental mode, and ψ_n the Gouy phase of the n^{th} optical mode. Further information on how the Gouy phase is obtained according to the optical mode basis will be be given in chapter 5.

Full interferometer and losses

Let us now introduce a more general formalism considering a full power- and signal-recycled interferometer, and the losses.

Figure 3.8 shows the fields of interest for an optical system corresponding to AdV; the size of the scattering matrix $S_n^{\pm}$ is then 12×12. One can write the scattering matrix as the product of a propagation matrix $P_n^{\pm}$, which is diagonal, and a mirror matrix M_n containing the amplitude reflection and transmission coefficients, as

$$S_n^{\pm} = M_n P_n^{\pm}, \tag{3.11}$$

where

$$P_n^{\pm} = \begin{pmatrix} p_{n,1}^{\pm} & 0 & \cdots \\ 0 & p_{n,2}^{\pm} & \\ \vdots & & \ddots \end{pmatrix}, \tag{3.12}$$

with

$$p_{n,x}^{\pm} = \exp\left[j\left(\phi_{n,x} \pm \frac{\omega_m L_x}{c}\right)\right]. \tag{3.13}$$

L_x is the propagation distance at the field point x, and $\phi_{n,x}$ the propagation phase of the n^{th} optical mode at x. The propagation factor yields constructive interferences when the total phase is $0\,[2\pi]$, that is to say when

$$\left.\begin{array}{rcccccc} & \phi_{0,x} & - & \psi_{n,x} & = & \omega_m \dfrac{L_x}{c} + 2k\pi \\ \Rightarrow & \dfrac{\phi_{0,x}}{\pi}\dfrac{c}{2L_x} & - & \dfrac{\psi_{n,x}}{\pi}\dfrac{c}{2L_x} & = & \nu_m + 2k\pi \\ \Rightarrow & \nu_{0,x} & - & \nu_{n,x} & = & \nu_m + 2k\pi, \end{array}\right\}\text{Stokes} \tag{3.14}$$

$$\left.\begin{array}{rcccccc} & \phi_{0,x} & - & \psi_{n,x} & = & -\omega_m \dfrac{L_x}{c} + 2k\pi \\ \Rightarrow & \nu_{n,x} & - & \nu_{0,x} & = & \nu_m + 2k\pi. \end{array}\right\}\text{anti-Stokes} \tag{3.15}$$

With these equations, one retrieves the condition for an OPI to occur: the mechanical mode frequency must be close to that of the optical beat note.

Now, if the mirror transmission coefficient is much smaller than one, one can further split the mirror matrix into a constant matrix M and a loss matrix C_n, which is diagonal, as

$$M_n = MC_n, \tag{3.16}$$

where

$$M = \begin{pmatrix}
\cdot & -r_{\text{NEM}} & \cdot & \cdot & \cdot & \cdot & \cdot & \cdot & \cdot & \cdot & \cdot & \cdot \\
-r_{\text{NIM}} & \cdot & \cdot & \cdot & \cdot & t_{\text{NIM}} & \cdot & \cdot & \cdot & \cdot & \cdot & \cdot \\
\cdot & \cdot & \cdot & -r_{\text{WEM}} & \cdot & \cdot & \cdot & \cdot & \cdot & \cdot & \cdot & \cdot \\
\cdot & \cdot & -r_{\text{WIM}} & \cdot & \cdot & \cdot & \cdot & t_{\text{WIM}} & \cdot & \cdot & \cdot & \cdot \\
t_{\text{NIM}} & \cdot & \cdot & \cdot & \cdot & r_{\text{NIM}} & \cdot & \cdot & \cdot & \cdot & \cdot & \cdot \\
\cdot & \cdot & \cdot & \cdot & \cdot & \cdot & \cdot & \cdot & \cdot & t_{\text{BS}} & \cdot & r_{\text{BS}} \\
\cdot & \cdot & t_{\text{WIM}} & \cdot & \cdot & \cdot & \cdot & r_{\text{WIM}} & \cdot & \cdot & \cdot & \cdot \\
\cdot & \cdot & \cdot & \cdot & \cdot & \cdot & \cdot & \cdot & \cdot & -r_{\text{BS}} & \cdot & t_{\text{BS}} \\
\cdot & \cdot & \cdot & \cdot & t_{\text{BS}} & \cdot & -r_{\text{BS}} & \cdot & \cdot & \cdot & \cdot & \cdot \\
\cdot & \cdot & \cdot & \cdot & \cdot & \cdot & \cdot & \cdot & -r_{\text{PRM}} & \cdot & \cdot & \cdot \\
\cdot & \cdot & \cdot & \cdot & r_{\text{BS}} & \cdot & t_{\text{BS}} & \cdot & \cdot & \cdot & \cdot & \cdot \\
\cdot & \cdot & \cdot & \cdot & \cdot & \cdot & \cdot & \cdot & \cdot & \cdot & -r_{\text{SRM}} & \cdot
\end{pmatrix} \tag{3.17}$$

and

$$C_n = \begin{pmatrix} t_{n,1} & \cdot & \cdots \\ \cdot & t_{n,2} & \\ \vdots & & \ddots \end{pmatrix}, \tag{3.18}$$

were $t_{n,x}$ is the amplitude transmission of the aperture of the each fields of interest, and $\cdot$ stands for 0.

Now that everything needed to compute the optical transfer coefficient has been presented, let us focus on the role played by this coefficient. By making the mechanical frequency artificially vary, one can obtain the optical transfer functions of an optical mode, as well as the parametric gain R_m of a given mechanical mode. The results for AdV's O3 configuration with the third couple

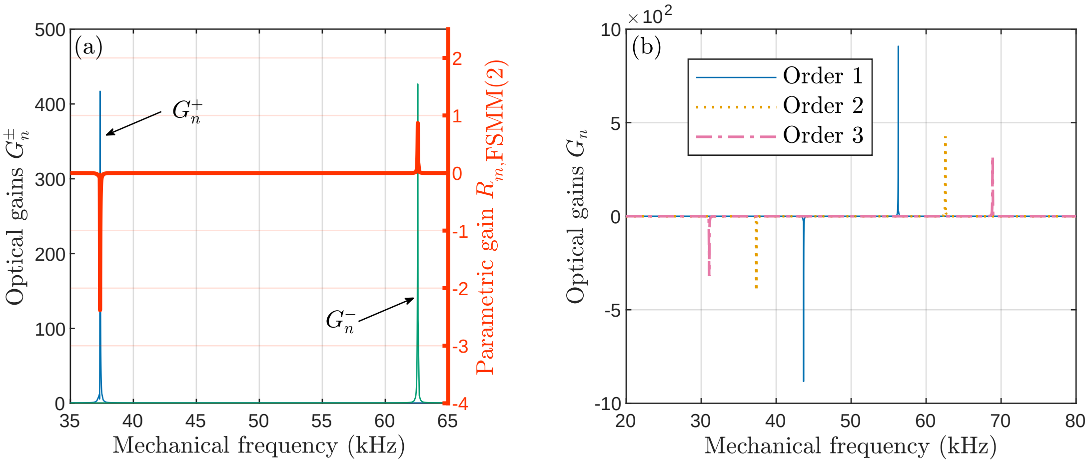

Figure 3.9: (a) G_n^+ (blue curve), G_n^- (green curve), and R_m (red curve) of the third couple from fig. 3.6, while artificially modifying the mechanical frequency. The upper sideband at 37 kHz has a negative optical transfer coefficient. The lower sideband at 63 kHz has a positive one, but the parametric gain is not high enough to lead to an OPI. (b) G_n of three optical modes of order 1, 2, and 3. The resonant frequencies are set by the optical mode phase, and, therefore, by the cavity Gouy phase and the optical mode order. One can also notice that the higher the optical mode order, the lower its gain, as expected.

of modes from fig. 3.6 are shown in fig. 3.9(a)[1]; all the optical values used in our simulations are summarised in table 6.1. One can see that the upper sideband indeed yields a negative parametric gain, while the lower one yields a positive parametric gain.

An interesting point is that although the spatial overlap parameter between those three modes is rather high, the optical transfer coefficient does not lead to an OPI. Hence the critical roles of the optical transfer coefficient and the mechanical mode frequency.

Figure 3.9(b) shows the optical transfer coefficient G_n for three optical modes of order 1, 2, and 3. Inasmuch as a cavity Gouy phase is fixed, only the mode order modifies the resonant frequency. Therefore, the main optical contributors to the parametric gain of a mechanical mode are all of the same order.

3.4 Summary

The OPI in gravitational-wave detectors is a well and long-studied phenomenon since the early 2000s. The OPI results from the interaction between two optical modes of the cavity and a mechanical mode of a mirror. The motion of a mirror at ω_m can scatter photons from the fundamental mode into two sidebands ($\omega_1 = \omega_0 \pm \omega_m$), which, in turn, interact with the mechanical mode via radiation pressure, and so on. This process can either lead to an exponential increase (lower sideband) of the mechanical motion or its damping (upper sideband). The former case can lead to a loss of the control of the interferometer and becomes more important and likely to happen if the available energy of the fundamental mode is higher. Indeed, such instabilities have already been observed at aLIGO and AdV. That is why we study their behaviours for AdV.

The interaction between a mechanical mode m and all the cavity optical modes can be quantified by its parametric gain R_m (eq. (3.3)). The mechanical mode is amplified if $R_m > 0$, and is damped if $R_m < 0$. The mechanical mode becomes unstable if $R_m > 1$. This parametric

---

[1] We are always interested to know the parametric gains for fields at mirror locations, that is to say the field points $x = \{1, 2, 3, 4\}$. Therefore, the given results will always be obtained from a mirror field. If the cavity name or the mirror names matter, then they will be specified.

gain comprises three terms: the prefactor, the optical transfer coefficient G_n, and the spatial overlap parameter $B_{m,n}$.

- The prefactor depends on the mechanical mode (Q factor and frequency), the mirror mass, the intracavity power, and the laser wavelength.
- The optical transfer function — according to both the fundamental mode (ω_0) and the HOM (ω_1) — sets the optical resonance (frequency $\omega_0 - \omega_1$, amplitude, and linewidth), which depends on both the fundamental mode and the HOM. The optical transfer coefficient (or optical gain) is the value of the optical transfer function at the mechanical mode frequency ω_m.
- The spatial overlap parameter depends on the amplitudes of the fundamental mode, the HOM, and the mechanical mode. This factor is higher if the shapes of the three implied modes match.

The optical gain and the overlap parameter are calculated for a specific HOM. The mechanical mode's parametric gain sums up the contributions of all the optical modes taken into account. Hence, the OPI study primary requires the computation of the arm cavity mirrors' mechanical modes and the arm cavities' optical modes. This will be the topic of the two following chapters.

Chapter 4

Mechanical modes of Advanced Virgo's arm cavity mirror

The mechanical modes were computed by means of finite element analysis (FEA) developed for the actual Input Mirror (IM) of Advanced Virgo (AdV) arm cavities. We used the program Ansys®Workbench$^{\text{TM}}$. The IM model includes the high-reflectivity coating of the front face, the flats and the bevels. Moreover the ears and the anchors attached by silicate bonding technique are included (see fig. 4.1). In the FEA, the multilayered optical coating is modelled as a solid 3D element having the total thickness corresponding to the sum of the thicknesses of the high reflective and low reflective materials and mechanical parameters averaged over the thicknesses of the layers. Instead of 3D *shell elements*, we have used 3D *solid elements*, for very thin materials as well, though more CPU time consuming, because they provide the shear deformations and energies, which are useful for getting the mechanical losses associated to the modes.

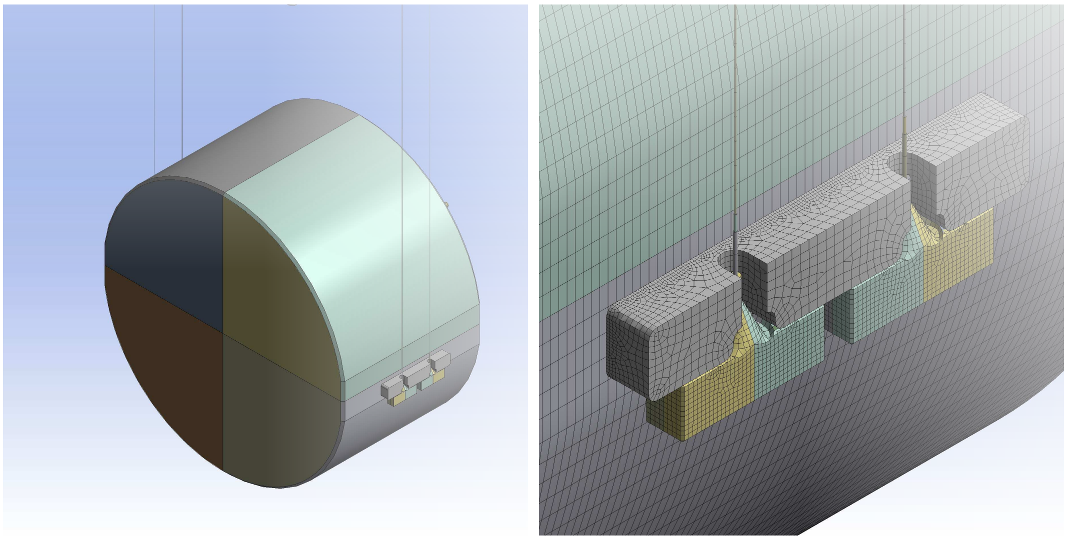

Figure 4.1: Geometry used for the FEA, including the ears, the anchors and the magnets attached on the mirror rear face. The suspension wires are just for sketching but not included in the simulation as they do not influence the modal frequencies.

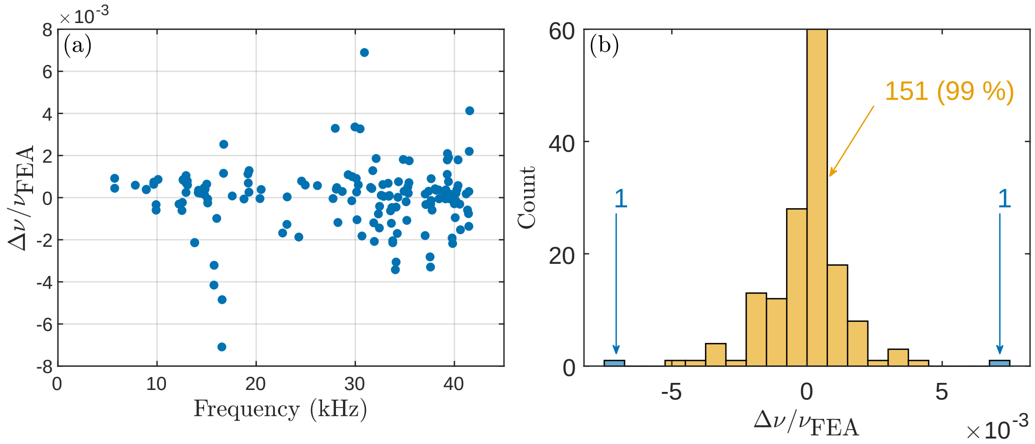

Figure 4.2: (a) Relative differences of measured frequencies with respect to frequencies obtained with the FEA vs the FEA frequencies. The standard deviation $\sigma(\nu_{\mathrm{meas}})$ is 0.15 %. (b) Distribution of the relative differences; the bin width is $\sigma(\nu_{\mathrm{meas}})/2$. There are 153 data, of which 151 (99 %) are comprised within $\pm 3.5\,\sigma(\nu_{\mathrm{meas}}) \approx \pm 0.50\,\%$.

4.1 Finite element analysis simulations results

The flats, the ears, and the anchors play an important role. In particular, since they break the cylindrical symmetry, they lift degeneracies and increase the number of distinct mode frequencies.

To estimate the accuracy of the model, we used a set of frequencies (ν_{meas}) measured from ring-down measurements of the North Input Mirror (NIM) up to 40 kHz. Figure 4.2(a) shows the relative differences $(\nu_{\mathrm{meas}} - \nu_{\mathrm{FEA}})/\nu_{\mathrm{FEA}}$ versus the frequency of the FEA ν_{FEA}. The standard deviation is 0.15 %. Figure 4.2(b) shows their distribution: 99 % are comprised within $\pm 3.5\,\sigma(\nu_{\mathrm{meas}}) \approx \pm 0.50\,\%$.

We estimated the quality factors (Q factors) of the mechanical modes of the IM taking into account several kinds of losses: losses of the fused silica (FS) substrate, anchors and supports of the magnets (loss angle ϕ_{FS}); coating losses (loss angle $\phi_{\mathrm{IMcoating}}$); losses of bonding layers used to attach the ears, the anchors, and the magnets (loss angle ϕ_{Bonding}). The bonding layers have a thickness of 60 nm and are modelled as 3D solid elements. Coating losses of the IM and End Mirror (EM) were recently measured [74]. Note that all the parameters used are given in table 4.1. Each loss contributor is related to the energy fraction stored in the lossy part and to the material loss angle, through the relationships

$$\begin{aligned} \phi_{\mathrm{Bonding}} \cdot E_{\mathrm{tot}} &= \phi_{\mathrm{HCB}} \cdot E_{\mathrm{bonds}} \\ \phi_{\mathrm{IMcoating}} \cdot E_{\mathrm{tot}} &= \phi_{\mathrm{CIM}} \cdot E_{\mathrm{CIM}} \\ \phi_{\mathrm{FS}} \cdot E_{\mathrm{tot}} &= \phi_{\mathrm{Suprasil}} \cdot E_{\mathrm{FS}}, \end{aligned} \tag{4.1}$$

where HCB stands for hydroxide-catalysis bonds. The overall loss angle for the IM is obtained by summing up all contributors: $\phi_{\mathrm{IM}} = \phi_{\mathrm{Bonding}} + \phi_{\mathrm{IMcoating}} + \phi_{\mathrm{FS}}$. The mechanical Q factor of the IM modes then writes

$$Q_m = 1/\phi_{\mathrm{IM}}. \tag{4.2}$$

Figure 4.3 shows the frequency dependence of the FS substrate loss and the effect of adding the optical coating and the bonding layers. The influence of the bonding term ϕ_{Bonding} is strongly mode shape dependent through the deformation of the ear and anchor bulks, and it is not negligible. In fact, its contribution to Q_m is dominant. For this reason, from a set of Q factor measurements, it is possible to infer the value of ϕ_{HCB} by using the energy fractions calculated with the FEA.

Figure 4.4(a) Q_m of the IM mass computed by fitting the loss angle ϕ_{HCB} by using the first set of five modes of the IM of the North arm and supposing that it is does not vary with the

IM Coating[1]		
Ta_2O_5 High index Layer Overall Thickness (t_H^{IM})	2080	nm
SiO_2 Low index Layer Overall Thickness (t_L^{IM})	727	nm
Loss angle (ϕ_{CIM})	$1.1 \cdot 10^{-4} f^{0.05}$	
EM Coating[1]		
Ta_2O_5 High index Layer Overall Thickness (t_H^{EM})	3766	nm
SiO_2 Low index Layer Overall Thickness (t_L^{EM})	2109	nm
Loss angle (ϕ_{CEM})	$2.2 \cdot 10^{-4} f^{0.01}$	
TM Suprasil		
Young modulus	72.251	GPa
Poisson ratio	0.166 49	
Density	2201	$\mathrm{kg\,m^{-3}}$
Loss angle ($\phi_{Suprasil}$)	$7.6 \cdot 10^{-12} f^{0.11}$	
Ear and anchors bonding [75]		
Young's modulus	72.9	GPa
Poisson ratio	0.17	
Density	2201	$\mathrm{kg\,m^{-3}}$
Thickness	60	nm
Loss angle	0.1	
IM and EM properties		
Mass	42	kg
Thickness	200	mm
Diameter	350	mm
Flats	50	mm

Table 4.1: Mechanical parameters used in the FEA

---

[1] For the FEA, the IM multilayered coating was replaced by one layer having the total thickness corresponding to the sum of the thicknesses of the high reflective and low reflective materials. The mechanical parameters used are the average values of this layer [74].

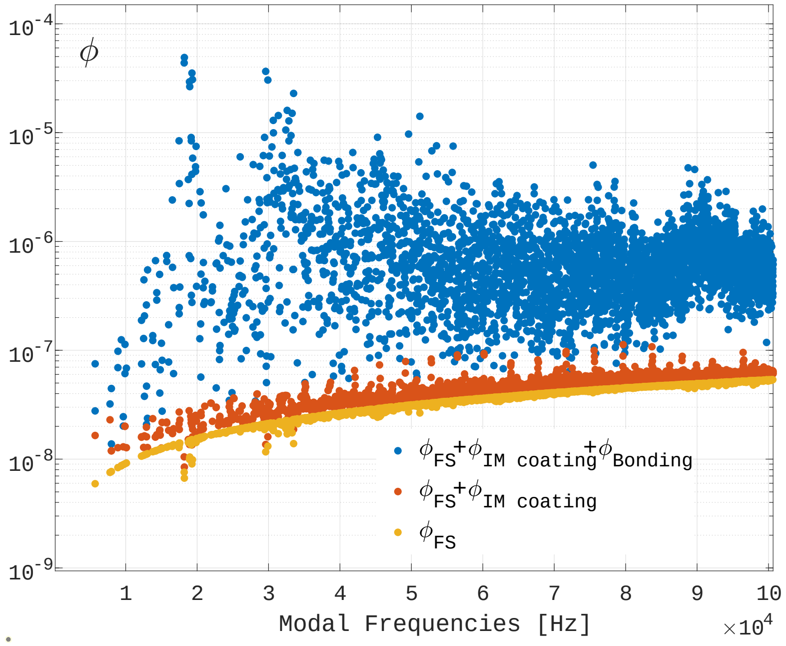

Figure 4.3: Losses present in the FEA model of the IM, computation up to 100 kHz.

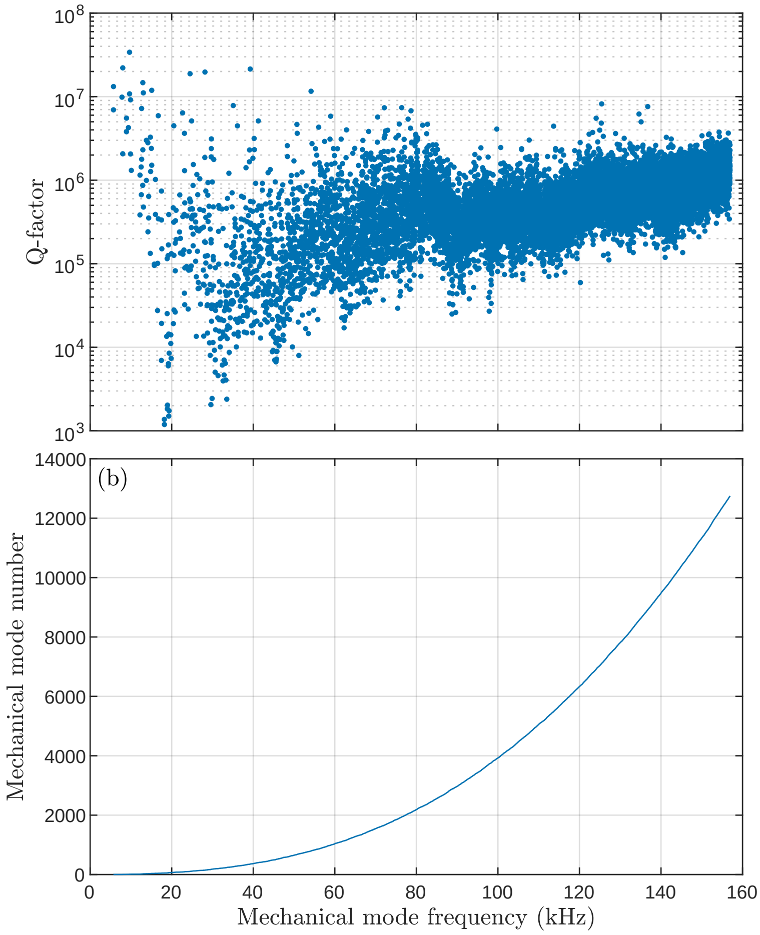

Figure 4.4: (a) Q factors of the mechanical modes up to 157 kHz. (b) Mechanical mode frequency vs Mechanical mode number. The mechanical mode density considerably increase at high frequency.

frequency. At frequencies higher than 10 kHz, the bondings have a strong damping effect, though they have a negligible effect on the the thermal noise of the IM. This is a very important result for the parametric gains computation and, consequently, for identification of the unstable modes.

Figure 4.4(b) shows the total number of mechanical modes with respect to their frequencies. We computed 12 750 mechanical modes up to 157 kHz. In chapter 6, I explain that we had first computed only 1600 mechanical modes, up to 70 kHz, but then, we needed to compute much higher-frequency modes.

Figure 4.5 shows some mechanical modes, arbitrarily chosen over the whole frequency range. Above each is indicated the measured frequency ν_{meas}.

4.2 Conclusion

The computation of the mechanical modes was done by Paola Puppo (INFN Roma), using 3D solid elements FEA simulation. It provided us with the mode shapes, the simulated frequencies ν_{FEA}, and the simulated Q factors Q_{FEA}. Paola Puppo also measured, on site the frequencies ν_{meas} and the Q factors Q_{meas} of the mechanical modes of the IMs from ring-down measurements. The measured frequencies allowed us to estimate the relative difference between the simulation and the measurements. The measured Q factors allowed us to fit the Q_{FEA} up to 157 kHz. The three cited parameters obtained by the FEA simulation and the measurements are sufficient to

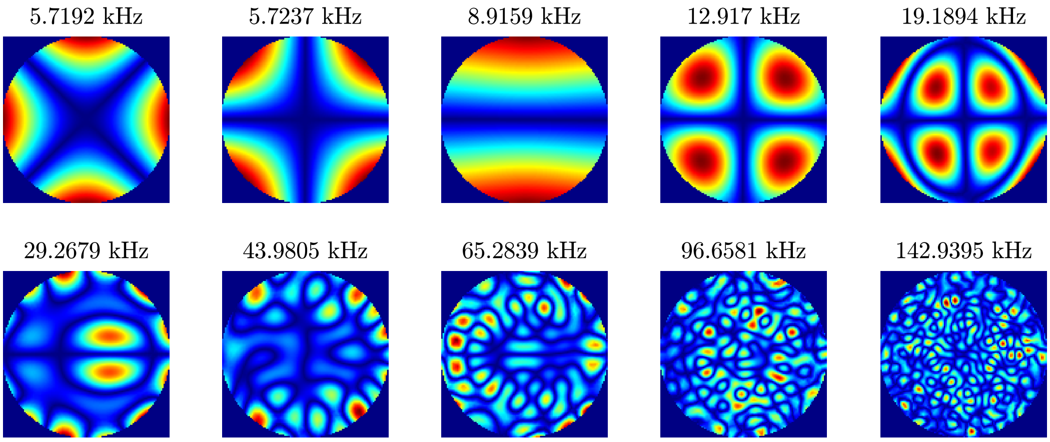

Figure 4.5: Some arbitrarily chosen mechanical modes.

characterise the mechanical modes that we need to compute the parametric gains in chapter 6.

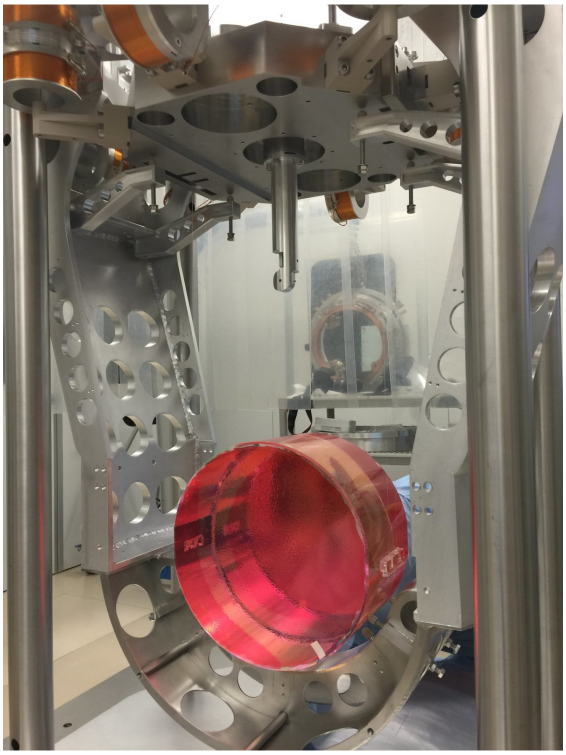

Figure 4.6: Photograph of a 42 kg AdV's arm cavity mirror suspended inside the payload by two thin wires of FS. The pink colour is due to a protecting film. Credits: Virgo collaboration.

Chapter 5

Optical modes of Advanced Virgo's arm cavities

The previous chapters showed basics of gravitational waves and ground-based interferometric gravitational-wave detection. It was explained how to improve the sensitivity of detectors with various techniques. Then, the optomechanical parametric instability (OPI) phenomenon was introduced, leading to the computation of the arm cavity mirrors' mechanical modes and the arm cavities' optical modes. This chapter will focus on the description of arm cavities' modes.

First is introduced some basic concepts of optical resonators. Then is presented the behaviour of Fabry-Perot resonators (plane-mirror resonators), which will help introduce essential quantities related to resonators. Then, the case of spherical-mirror cavities is treated. Two different models that can be used to compute optical modes are compared: a model considering the mirrors as infinite, and another one considering the real finite size of the mirrors. Optical modes of the former can be computed thanks to well-known and well-studied bases, such as the Hermite-Gaussian modes (HGM), whereas optical modes of the latter require a numerical computation. I will show the limits of the HGM with respect to the finite-sized mirror modes (FSMM). Finally, I introduce the effect, on optical modes, of the mirror deformation due to light absorption (sometimes referred to as 'thermal effects').

5.1 Wave optics conventions and notation

5.1.1 On light propagation in vacuum

An linearly polarized optical field can be described by a scalar complex *wavefuntion* $E(\mathbf{r}, t)$ of position $\mathbf{r}$ and time t. $E(\mathbf{r}, t)$ must satisfy the *wave equation*

$$\nabla^2 E(\mathbf{r}, t) - \frac{1}{c^2}\frac{\partial^2 E(\mathbf{r}, t)}{\partial t^2} = 0, \tag{5.1}$$

where c is the speed of light in vacuum.

In the following, we restrict ourselves to *monochromatic waves*. For a monochromatic wave propagating with the wavenumber $k = \frac{\omega}{c}$ at the instant t, the wavefunction is

$$E(\mathbf{r}, t) = A(\mathbf{r})\, e^{j(\omega t - \mathbf{k}\cdot\mathbf{r})}, \tag{5.2}$$

where $\omega = 2\pi\nu$ is the pulsation, ν the frequency, and $A(\mathbf{r})$ a complex function. Equation (5.2) can be rewritten

$$E(\mathbf{r}, t) = E(\mathbf{r})\, e^{j\omega t}, \quad E(\mathbf{r}) = A(\mathbf{r})\, e^{-j\mathbf{k}\cdot\mathbf{r}}, \tag{5.3}$$

where $E(\mathbf{r})$ is the *complex amplitude* and is time independent. In all the following, we will study the properties of $E(\mathbf{r})$, which is the spatial part of the wavefunction.

Substituting eq. (5.3) into eq. (5.1) yields

$$\nabla^2 E(\mathbf{r}) + k^2 E(\mathbf{r}) = 0 \tag{5.4}$$

known as the *Helmholtz equation*.

5.1.2 Incident, reflected, and transmitted waves

An incident wave reflecting on a mirror undergoes a π phase shift such that a possible convention for the scattering matrix is

$$\begin{pmatrix} E_{r_1} \\ E_{r_2} \end{pmatrix} = \begin{pmatrix} t & -r \\ -r & t \end{pmatrix} \begin{pmatrix} E_{i_3} \\ E_{i_4} \end{pmatrix} \tag{5.5}$$

where r is the amplitude reflection coefficient, and t the amplitude transmission coefficient (fig. 5.1).

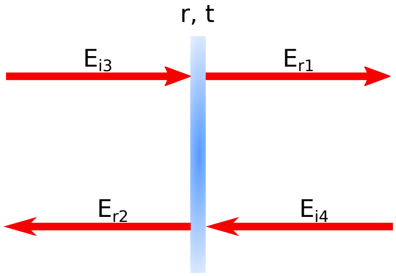

Figure 5.1: Incident, reflected, and transmitted field notations.

In the following, we use these results to calculate the different optical fields of a resonator.

5.1.3 Reflection, transmission, and losses

An optical element is characterised by three coefficients: its amplitude reflection coefficient r, its amplitude transmission coefficient t, and its amplitude losses. By squaring these quantities, one obtains respectively the intensity reflection coefficient (or reflectivity, or reflectance) $\mathcal{R} = r^2$, the intensity transmission coefficient (or transmissivity, or transmittance) $\mathcal{T} = t^2$, and the intensity losses $\mathcal{L}$. Hence, the energy conservation of the incident wave reads

$$\mathcal{R} + \mathcal{T} + \mathcal{L} = 1. \tag{5.6}$$

Losses can be of various types: absorption in the mirror coatings, scattering on mirrors due to imperfections, and diffraction loss due to the finite size of the mirrors. The diffraction loss will be referred to as $\mathcal{L}_d$, and all the others losses as[1] $\mathcal{L}_m$. Then comes

$$\mathcal{L} = \mathcal{L}_d + \mathcal{L}_m. \tag{5.7}$$

5.2 Fabry-Perot resonators

Interferometric gravitational-wave detectors have optical cavities on both of their arms to increase the sensitivity inasmuch as the phase shift induced by the passage of a gravitational wave is multiplied by a factor G_{AFPC}, as explained in section 2.2.2. To better understand longitudinal modes of these cavities, one can use the model of plane-mirror resonators, called *Fabry-Perot resonators*, which consist in two mirrors M_1 and M_2 with their associated reflection coefficients r_1, r_2, and transmission coefficients t_1, t_2[2], separated by a distance L, as shown in fig. 5.2.

---

[1] For '*mirror losses*'.

[2] Ideally, the end mirror must be perfectly reflective, whereas the input one should have a non-null transmissivity such that the light can enter the resonator. In the case of Advanced Virgo, the very small amount of transmitted light at the end mirror allows to obtain an information about the circulating light field and, thus, to control the Fabry-Perot resonator length during the acquisition of the global interferometer working point.

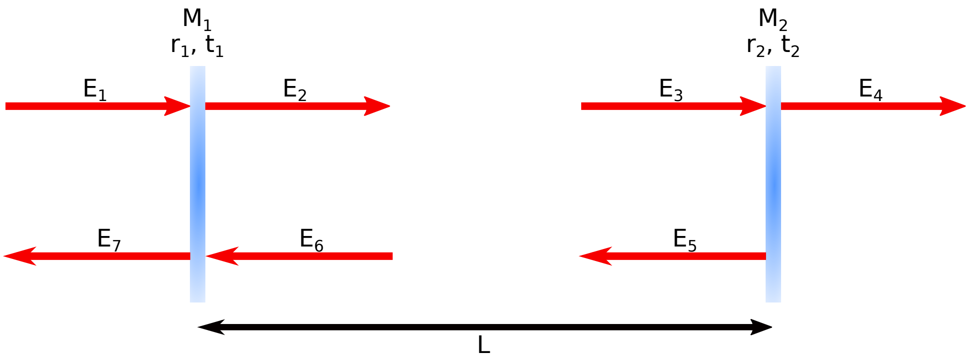

Figure 5.2: Optical fields of a Fabry-Perot resonator.

5.2.1 Optical fields and resonant frequencies

Considering the complex amplitude of the electromagnetic field entering the resonator $E_{\text{in}} = E_1$, the circulating amplitude $E_{\text{circ}} = E_2$, the transmitted amplitude $E_{\text{trans}} = E_4$, and the reflected amplitude $E_{\text{refl}} = E_7$ can be calculated. The circulating field is the sum of all the fields circulating within the resonator (see fig. 5.3) and can then be described as a geometric progression with common ratio $r_1\, r_2\, e^{-jk2L}$. In order that the electromagnetic fields constructively interfere, and, thus, build a mode, they need to be in phase; hence the *resonance condition*

$$2kL = q2\pi \iff k = q\frac{\pi}{L} \iff \nu = q\frac{c}{2L}, q \in \mathbb{Z}. \tag{5.8}$$

This shows that only certain frequencies can lead to standing waves within the resonator: in the following, these modes will be referred to as *longitudinal modes*. The electromagnetic fields at each point of the resonator are

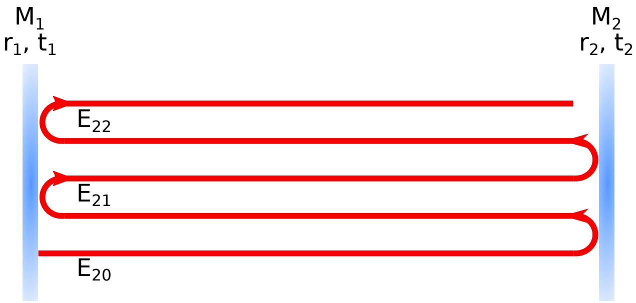

Figure 5.3: Travelling waves between both mirrors of a Fabry-Perot resonator.

$$\begin{aligned} E_2 &= t_1 E_1 - r_1 E_6 & E_5 &= -r_2 E_3 \\ E_3 &= E_2\, e^{-jkL} & E_6 &= E_5\, e^{-jkL} \\ E_4 &= t_2 E_3 & E_7 &= -r_1 E_1 + t_1 E_6. \end{aligned}$$

From these equations one can determine the electromagnetic fields inside the resonator of interest:

$$E_{\text{circ}} = \frac{t_1}{1 - r_1\, r_2\, e^{-jk2L}}\, E_{\text{in}} \tag{5.9}$$

In practice, the measurable quantity is the intensity (in W m^{-2}), obtained by squaring the modulus of the amplitude:

$$I_{\text{circ}} = |E_{\text{circ}}|^2 = E_{\text{circ}} \cdot E^*_{\text{circ}} = \frac{\mathcal{T}_1}{1 + r_1^2\, r_2^2 - 2r_1\, r_2\, \cos{(2kL)}} I_{\text{in}}, \tag{5.10}$$

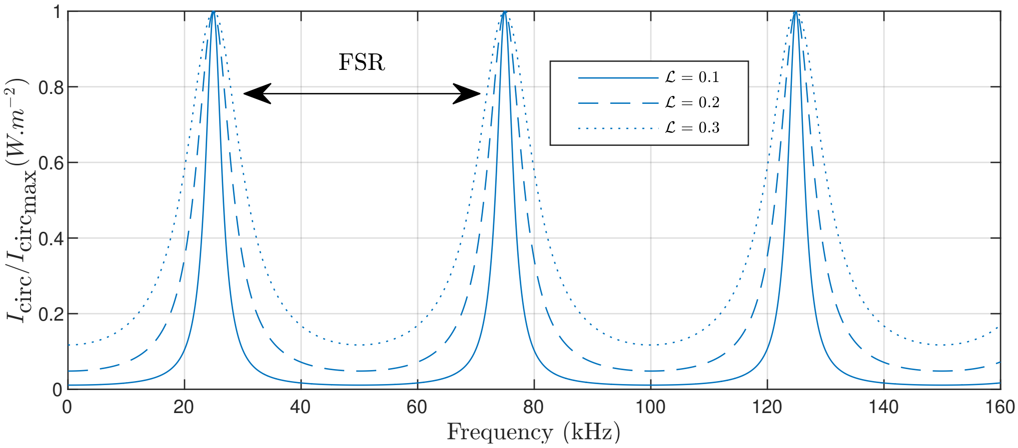

Figure 5.4: Circulating intensity within the resonator. The resonator acts as filter letting only some frequencies be resonant; these frequencies are separated by the Free Spectral Range represented by the arrow. The circulating intensity is normalised by $I_{\mathrm{circ}_{\max}}$ to show that $\delta\nu$ increases when $\mathcal{L}$ increases.

where $I_{\mathrm{in}} = |E_{\mathrm{in}}|^2$. The maximum power is

$$I_{\mathrm{circ}_{\max}} = \frac{\mathcal{T}_1}{(1 - r_1\, r_2)^2} I_{\mathrm{in}} \tag{5.11}$$

and is reached for $\cos(2kL) = 1$, the resonance condition already expressed by eq. (5.8). Equation (5.10) is called an *Airy function* (fig. 5.4) and depends on the losses accumulated during a resonator round trip. This function shows equally separated peaks representing the resonant frequencies of eq. (5.8) that can travel down the resonator. The frequency difference between two consecutive resonances is called *Free Spectral Range (FSR)*, and from eq. (5.8) arises

$$\Delta\nu_{\mathrm{FSR}} = \frac{c}{2L}. \tag{5.12}$$

Advanced Virgo (AdV)'s arms are 3 km long, then their FSR $\Delta\nu_{\mathrm{FSR}}$ is

$$\boxed{\Delta\nu_{\mathrm{FSR}} \approx 50.00\,\mathrm{kHz}.} \tag{5.13}$$

5.2.2 Effect of resonator losses

Mirrors cannot be perfectly reflective and show a non-null transmissivity $\mathcal{T}$ and energy losses $\mathcal{L}$. This modifies the travelling fields and relaxes the resonance condition, increasing, in turn, the Full Width at Half Maximum (FWHM). The FWHM is also known as the *linewidth* $\delta\nu$. Inasmuch as the finesse $\mathcal{F}$ can be defined as $\mathcal{F} = \Delta\nu_{\mathrm{FSR}}/\delta\nu$, from eq. (2.20) arises

$$\delta\nu \approx \Delta\nu_{\mathrm{FSR}} \frac{1 - r_1\, r_2}{\pi\sqrt{r_1\, r_2}}. \tag{5.14}$$

One can notice the dependence to the reflection coefficients: the higher they are (or the lower the losses), the thinner the linewidth. So, increasing losses broadens resonances (fig. 5.4).

Let us now introduce another more practical definition of the finesse:

$$\mathcal{F} = \frac{2\pi}{\mathcal{P}}, \tag{5.15}$$

where $\mathcal{P} = \mathcal{L}_1 + \mathcal{L}_2 + \mathcal{T}_1 + \mathcal{T}_2$ is the resonator total loss, including the mirror transmissions.

In summary, the lower the losses, the higher the finesse, the lower the linewidth. AdV's arm cavity[3] finesse have been measured on site [76]:

$$\boxed{\begin{aligned} \mathcal{F}_{\text{North}} &= 464(7) \\ \mathcal{F}_{\text{West}} &= 455(5) \end{aligned}} \tag{5.16, 5.17}$$

Consequently AdV's arm cavity linewidths are

$$\boxed{\begin{aligned} \delta\nu_{\text{North}} &\approx 108\,\text{Hz} \\ \delta\nu_{\text{West}} &\approx 110\,\text{Hz} \end{aligned}} \tag{5.18, 5.19}$$

The finesse contains all the information of the resonator losses, and eq. (5.9) can be rewritten

$$I_{\text{circ}} = \frac{I_{\text{circ}_{\max}}}{1 + G_{\text{AFPC}}^2 \sin^2(kL)}, \tag{5.20}$$

where $G_{\text{AFPC}} = 2\mathcal{F}/\pi$ is the optical gain of a Fabry-Perot resonator (see section 2.2.2) and is, for AdV, $G_{\text{AFPC}} \approx 300$.

5.3 Spherical-mirror resonators

In the previous section, I have derived resonant frequencies of Fabry-Perot longitudinal modes, and discussed the impact of losses on the resonance linewidth. In this section, I substitute plane mirrors with spherical mirrors and show their impact on the resonant frequencies and on the resonator stability.

5.3.1 Gaussian beam

Complex amplitude and beam properties

Here, I want to obtain a precise description of the complex amplitude $E(\mathbf{r})$. As the field propagates along the z direction, we have

$$E(\mathbf{r}) = A(\mathbf{r})e^{-jkz}. \tag{5.21}$$

Substituting eq. (5.21) into eq. (5.4) yields

$$\nabla^2 A - 2jk\frac{\partial A}{\partial z} = 0. \tag{5.22}$$

Insofar as the longitudinal envelope variation of the beam is very slow within a distance of a wavelength $\lambda = 2\pi/k$, one can use the *paraxial approximation*. It implies that angles to the optical axis of the system are rather small. Therefore, a Gaussian beam has its energy confined about its axis. The paraxial approximation helps further simplify eq. (5.22) by neglecting the second derivative in z of the complex envelope, yielding the *paraxial Helmholtz equation*

$$\nabla_T^2 A - 2jk\frac{\partial A}{\partial z} = 0, \tag{5.23}$$

where $\nabla_T^2 = \partial^2/\partial x^2 + \partial^2/\partial y^2$ is the transverse Laplacian operator. In the absence of boundary conditions, a well-known solution is the so-called *Gaussian beam*, whose complex amplitude writes [77]

$$E(\rho, z) = A_0 \frac{w_0}{w(z)} \exp\left[-\frac{\rho^2}{w^2(z)}\right] \exp\left[-j\left(kz + \frac{k\rho^2}{2R(z)} - \psi(z)\right)\right], \tag{5.24}$$

---

[3] Here, I speak in terms of cavity because these resonators are stable.

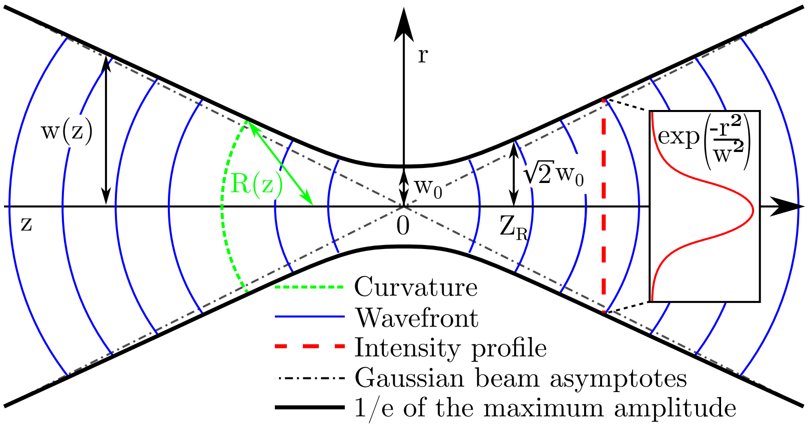

Figure 5.5: A Gaussian beam profile, together with its Gaussian function transverse projection. Around the beam waist, the wavefronts are approximately planar, afar they are approximately spherical. Image by ℵ (Aleph) `http://commons.wikimedia.org`, modified, under the terms of the Creative-Commons-License CC-BY-SA-2.5.

where $\rho^2 = x^2 + y^2$, $w(z)$ is the beam radius at which the amplitude falls to $1/e$ ($\sim 27\%$) of the maximum (which is on the axis) at z[4], $w_0 = w(0)$ is the *waist radius*, which is the beam radius at its focus, that is, where its radius is minimum, $R(z)$ the wavefront radius of curvature at z, and $\psi(z)$ is the *Gouy phase*, which is an extra phase accumulated along the z-axis.

Figure 5.5 shows a Gaussian beam along the z-axis, together with all parameters defining such a wave. Its transverse profile is indeed a Gaussian function. Longitudinally, this Gaussian function propagates along the z direction, and if one lets the origin of this axis be at the beam waist, the width of the beam becomes larger while increasing $|z|$ due to diffraction. Around the beam waist, the wavefronts are approximately planar; afar from the beam waist, they are approximately spherical. One can then define two approximate regions and a parameter called the *Rayleigh range* z_R (eq. (5.25)): *near field* when $z \ll z_R$ and the *far field* when $z \gg z_R$.

Let us summarise, here, all parameters defining a Gaussian beam:

- Rayleigh range z_R:

$$z_R = \frac{\pi w_0^2}{\lambda} \tag{5.25}$$

- Beam radius $w(z)$:

$$w(z) = w_0 \sqrt{1 + \left(\frac{z}{z_R}\right)^2} \tag{5.26}$$

- Wavefront radius of curvature $R(z)$:

$$R(z) = z\left[1 + \left(\frac{z_R}{z}\right)^2\right] \tag{5.27}$$

- Gouy phase $\psi(z)$:

$$\psi(z) = \arctan\left(\frac{z}{z_R}\right) \tag{5.28}$$

Equations (5.26) and (5.27) help understand better the longitudinal evolution of the beam radius and the wavefronts.

---

[4] An amplitude drop of $1/e$ corresponds to an intensity drop of $1/e^2 \approx 0.135$; therefore, since the intensity carried within a circle of radius $w(z)$ represents 86%, it is justified to call $w(z)$ the beam radius.

Regarding the beam radius, as described above, the minimum w_0 is at the beam focus and increases in both directions, linearly with z for $z/z_R \gg 1$ (eq. (5.26)). Its value at z_R is $\sqrt{2}w_0$.

Regarding the wavefronts, eq. (5.27) shows that $\lim\limits_{z \to 0^{\pm}} R(z) = \pm\infty$, that is, the wavefronts are planar. While $w(z)$ increases, $R(z)$ first decreases until it reaches its minimum at z_R: the beam is curved the most at the Rayleigh range. Then, $R(z)$ slowly increases, tending towards an $R(z) = z$ asymptote.

Gaussian beam stability in a spherical-mirror resonator

Considering a resonator with two spherical mirrors of different radii of curvature R_1 and R_2 and separated by a distance L, one can let the origin of the z-axis be at the beam waist, and the two mirrors be respectively located at z_1 and z_2. In the following, such a device will be referred to as an optical cavity.

If the wavefront of an incident Gaussian beam has the same radius of curvature than a spherical mirror, then its reflected beam from that mirror will exactly retrace the incident beam. Thus, a beam within the cavity will be reflected on a mirror and will retrace itself to the second mirror, where the same phenomenon will occur, and, so on, the beam exists self-consistently and can be travelling within the cavity. A Gaussian beam can thus be a stable mode of a spherical-mirror resonator.

Introducing the *g parameters* as

$$g_i = 1 - \frac{L}{R_i}, \quad i = \{1, 2\}, \tag{5.29}$$

and their product

$$g = g_1\, g_2, \tag{5.30}$$

it can be shown that the stability condition of an optical cavity writes [77]

$$0 \leq g \leq 1. \tag{5.31}$$

Figure 5.6 shows different optical resonator configurations, which are represented by a dot on the diagram. The green area highlights the stable configurations. If $R_1 = R_2$, the cavity is a *symmetrical resonator* and lies on the first bisector in fig. 5.6.

Here are values of AdV's cavity parameters for both North and West AdV's arm cavities [36]:

$$L_{\text{AFPC}} = 2999.8\,\text{m} \qquad R_{\text{IM}} = 1420\,\text{m} \qquad R_{\text{EM}} = 1683\,\text{m},$$

yielding

$$\boxed{g_{\text{AFPC}} = g_{\text{IM}} \cdot g_{\text{EM}} = 0.8705,} \tag{5.32}$$

with g_{IM} and $g_{\text{EM}} < 0$. The cavities are indeed stable and are not symmetric yet not that far from being symmetrical concentric ones, i.e. $R_1 \approx R_2 \approx -d/2$. In that case, the field is focused at the centre of the cavity.

Phase and resonant frequencies

From eq. (5.24), one can write the Gaussian beam phase as a function of the radial ρ and the axial z positions:

$$\phi(\rho, z) = kz + \frac{k\rho^2}{2R(z)} - \psi(z). \tag{5.33}$$

The first term is the accumulated phase during the propagation along the z-axis; the second one is the bending of the wavefront (see eq. (5.27)); and the last one is the Gouy phase: a Gaussian beam accumulates a delay compare to a planar wave (see eq. (5.28) and fig. 5.7).

From eq. (5.33), one can write the difference in phase on the axis after one round trip

$$2\Delta\phi(\rho = 0) = 2kL - 2\Delta\psi \tag{5.34}$$

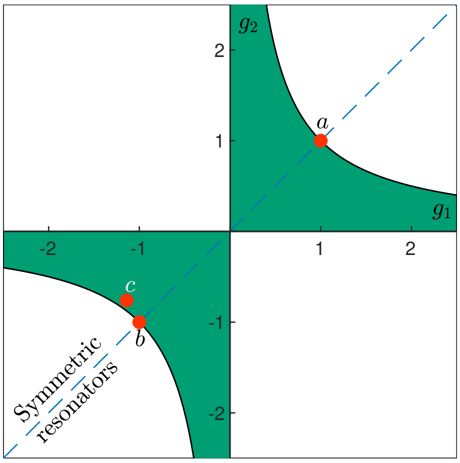

Figure 5.6: Representation of the hyperbola $g_1\, g_2 = 1$. Each resonator can be represented by a dot on this diagram. Given the stability condition $0 < g < 1$, any point located in the blueish green area represents a stable resonator. Three resonators of interest are highlighted: a represents a planar resonator (Fabry-Perot), b represents a symmetric concentric one, and c represents AdV's configuration, which is a quasi-symmetric-concentric one.

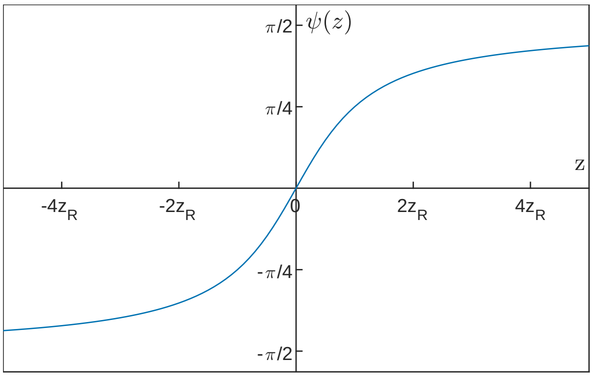

Figure 5.7: Gaussian beam's Gouy phase, which is the accumulated phase by a Gaussian beam along the z axis with respect to a planar wave. The farther away from the beam waist, the more phase is accumulated.

where $\Delta\phi(\rho = 0) = \phi(0, z_2) - \phi(0, z_1)$ is the Gouy phase shift accumulated during a single trip and is defined as [78, 79],

$$\Delta\psi = \psi(z_2) - \psi(z_1) = \arccos\left(\pm\sqrt{g}\right), \tag{5.35}$$

where the plus sign is chosen if g_1 and g_2 are positive, and the minus sign when g_1 and g_2 are negative. The approximate g parameter of AdV has been estimated to 0.8705, so the Gouy phase shift per single trip of AdV's arm cavity is

$$\boxed{\Delta\psi_{\text{AFPC}} = 2.774.} \tag{5.36}$$

Due to the Gouy phase, the resonance condition is modified compared to a planar resonator. The phase accumulated along a cavity round trip must verify

$$2\Delta\phi(\rho = 0) = q2\pi, q \in \mathbb{Z}, \tag{5.37}$$

which yields

$$\nu_q = \Delta\nu_{\text{FSR}}\left[q + \frac{\Delta\psi}{\pi}\right]. \tag{5.38}$$

5.3.2 Infinite-sized mirror modes: Hermite-Gaussian modes (HGM)

The equation satisfied by the wave function is the Helmholtz equation. One can find infinite, countable, and complete orthogonal sets of modes that are solutions of this equation (bases). The chapter 3 of [77] and the article [78] provide detailed mathematical developments to show that HGM, Laguerre-Gaussian modes, and Bessel-Gaussian modes are sets of solutions to the paraxial Helmholtz equation, considering infinite-sized mirrors. In the case of perfect spherical mirrors (radial symmetry), the Laguerre-Gaussian basis is a natural basis because these modes, too, have such a radial symmetry. Be that as it may, I will focus only on HGM, for they are the simplest and the most commonly used.

Hermite-Gaussian modes: amplitudes and orders

The HGM are an orthogonal set of modes that can be used to decompose a paraxial beam using Cartesian coordinates. The transverse profile is the product of a function in x and one in y, whose referred index is respectively l and m. The complex amplitudes of HGM are

$$\begin{aligned} E_{lp}(\rho, z) = & A_{lp}\, \frac{w_0}{w(z)}\, \exp\left[-\frac{\rho^2}{w^2(z)}\right] \\ & \times H_l\left(\frac{\sqrt{2}\,x}{w(z)}\right) H_p\left(\frac{\sqrt{2}\,y}{w(z)}\right) \\ & \times \exp\left[-j\left(kz + \frac{k\rho^2}{2R(z)} - (l+p+1)\,\psi(z)\right)\right], \end{aligned} \tag{5.39}$$

where A_{lp} is a normalisation constant depending on l and p, H_n are Hermite polynomials.

Comparing eqs. (5.24) and (5.39), one can notice that the HGM are waves whose complex envelope are modulated forms of the Gaussian beam and whose phase is shifted. Both of these modifications depend on the values of l and p. A Hermite-Gaussian mode's profile is determined by a Hermite polynomial multiplied by a Gaussian profile. One can first study the effect of a single Hermite-Gaussian function, which is defined by

$$G_n(u) = H_n(u) \exp\left(\frac{-u^2}{2}\right). \tag{5.40}$$

Figure 5.8 shows the shapes of the first Hermite-Gaussian functions. First, note that the index n is the number of zeros of the polynomial; hence, an odd index yields an odd function, and an even index yields an even function. Then, a very important piece of information is that the profile becomes broader when n increases.

The two numbers l and p define the order N of the Hermite-Gaussian mode as

$$N = l + p, \quad l, p \in \mathbb{N} \tag{5.41}$$

and give its name HG_{lp}. There are always $N+1$ modes of order N. From eq. (5.39) letting $l = p = 0$ arises the same expression as eq. (5.24); therefore the HG_{00}, or the *fundamental mode*, is described by eq. (5.24) just as the free space Gaussian beam. The other modes are called *higher-order modes (HOMs)*. Figure 5.9 shows HGM for $l, p \in \{1, 2\}$. One can see the zeros of each polynomial according to the index values; these zeros correspond to dark fringes on the beam transverse profiles. Moreover, one can see, as well, the broadening of the beam profiles for increasing N.

Hermite-Gaussian modes: Gouy phases and resonant frequencies

Another interesting point yielded by eq. (5.39) is that the cavity Gouy phase increases with the mode order as

$$\boxed{\Delta\psi_N = (N+1)\,\Delta\psi.} \tag{5.42}$$

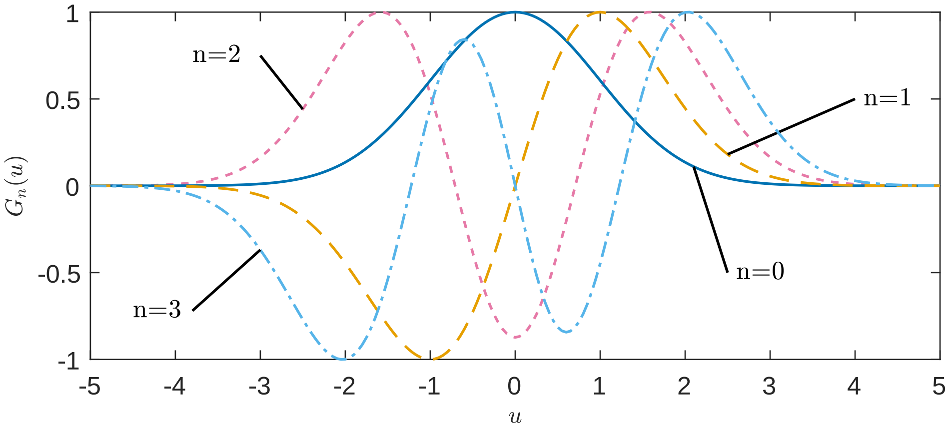

Figure 5.8: Normalised $G_n(u)$ for $n = \{0, 1, 2, 3\}$. The profile becomes broader when n increases.

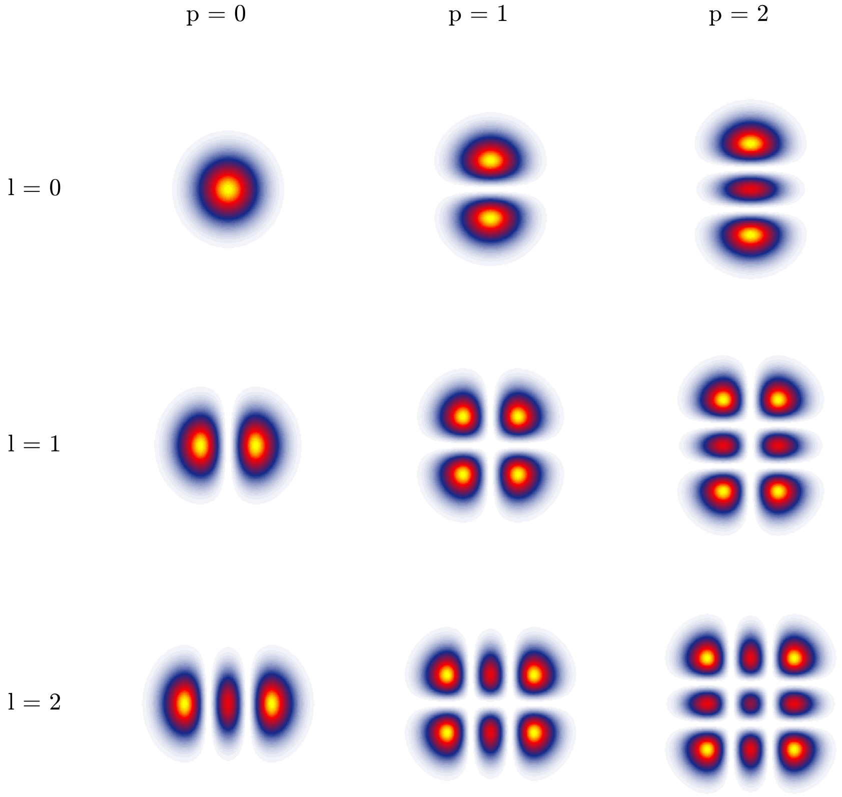

Figure 5.9: HGM intensity profiles for $l = 0, 1, 2$ and $p = 0, 1, 2$. One can see the zeros of the polynomials corresponding to the anti-nodes.

The higher the mode order, the more phase the beam will accumulate along the propagation direction. In chapter 3, the beat note that can lead to an OPI is defined as the frequency difference between the fundamental mode and an HOM; therefore, when it comes to compute the parametric gains, we are only interested in the frequency difference rather than the true frequency of an HOM. That is why we set the fundamental mode frequency to 0 and use $\Delta\psi_N = N\Delta\psi$.

From eqs. (5.38) and (5.42) comes the expression of the resonant frequencies:

$$\nu_{lp,q} = \Delta\nu_{\text{FSR}} \left[q + \frac{(N+1)\Delta\psi}{\pi} \right]. \tag{5.43}$$

For $l = p = 0$, this expression yields the same as eq. (5.38). The frequency difference between two adjacent orders is the Transverse Mode Spacing (TMS) $\delta\nu_{\text{TMS}}$ and writes

$$\delta\nu_{\text{TMS}} = \Delta\nu_{\text{FSR}} \frac{\Delta\psi}{\pi}. \tag{5.44}$$

The HGM basis is easy to implement as the mode shapes are provided by simple analytical formulas, but it does not include the effects of the deviations from the spherical shape due to fabrication imperfections or light absorption within the coating. Finally, it does not include finite size effects such as the diffraction loss, which must be estimated separately.

Hermite-Gaussian modes: diffraction loss estimation

Diffraction loss[5] stems from the finite size of the cavity mirrors. We evaluate diffraction losses for HGM like in [55], by evaluating the ratio of the light flux within the AdV's mirrors' coating radius R_{coating} to the total flux. To do so, we first create a disc mesh larger than the coating diameter by a factor C — this is the red circle in fig. 5.10. Secondly, we compute the intensity of the mode over this mesh. Then, we truncate the mode at the disc of the coating diameter — the green circle in fig. 5.10. Finally, we calculate the energy fraction that is not within the green disc, that is, the energy that is lost, leading to the diffraction loss:

$$\text{diffraction loss} = 1 - \frac{\text{intensity in small disc}}{\text{intensity in large disc}} \tag{5.45}$$

Convergence with respect to C The factor C enables an artificial infinite circle. To make the circle infinite-like, it only needs be large enough so that it comprises most of the energy of the larger considered HGM. To find this minimum value of C, we compute the diffraction loss of the HG_{44} for different values of C at a fixed Γ, where Γ is the number of pixels on the coating diameter. Γ is set to 3500 ($\Delta x \approx 10\,\mu\text{m}$) so that it is high enough to ensure that the results not be biased. The result is shown in fig. 5.11 (a). A convergence is reached from $C = 1.5$. We, therefore, endorse that 1.5 times R_{coating} is enough to use order-8 modes.

Convergence with respect to the grid size Making Γ vary instead of C, which is now fixed to 1.5, we can perform the same process. Figure 5.11 (b) shows the diffraction loss of the same HG_{44} with respect to Γ at a fixed $C_0 = 1.5$. From $\Gamma = 650$, a convergence is reached.

Conclusion We can estimate HGM's diffraction losses as in [55], setting $C \geq 1.5$ to mimic an infinite disc, providing that we compute the HGM with $\Gamma \geq 650$. One can now plot the diffraction losses of the HGM, shown in fig. 5.12. The diffraction losses do increase while increasing the optical mode order. The diffraction loss of the HG_{00} (or TEM_{00}) is 3.23×10^{-2} ppm. The arm cavity finesse is determined by the total losses of the arm cavity fundamental mode (eq. (5.15)). The transmissivities of AdV's Input Mirrors (IMs) are around 13 760 ppm, dominating the total arm cavity losses and yielding an arm cavity finesse of approximately 455 ; it matches the measured AdV's finesses.

---

[5] Sometime referred to as *clipping loss*

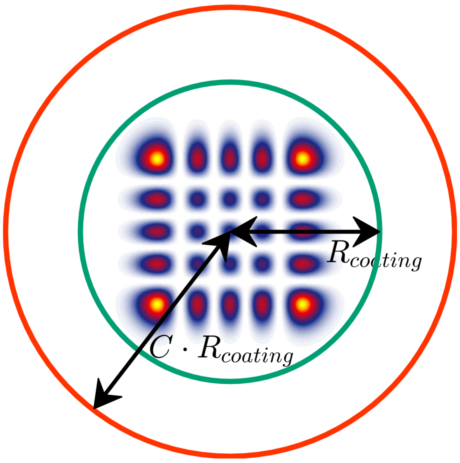

Figure 5.10: Method to estimate the diffraction losses of the HGM. This one is the HG_{44}. The green circle highlights the coating radius R_{coating} of the mirrors of AdV's arm cavities. The red circle highlights a larger radius built to mimic an infinite mirror and is C times larger than R_{coating}.

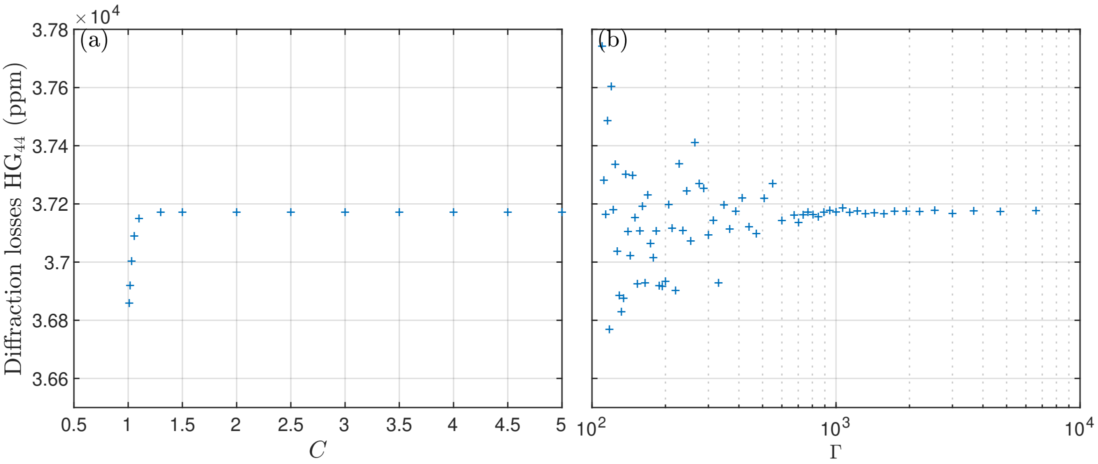

Figure 5.11: Convergence tests for the HG_{44} diffraction loss. (a) Diffraction loss while making C vary, with a fixed $\Gamma_0 = 3500$. A convergence is reached for $C = 1.5$. (b) Diffraction loss while making Γ vary, with a fixed $C_0 = 1.5$. A convergence is reached from $\Gamma = 650$.

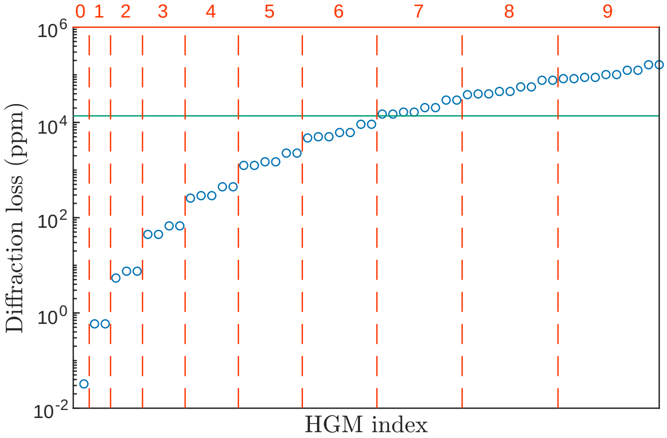

Figure 5.12: Diffraction losses of HGM. The green line shows the IM transmissivity ($\simeq 13\,760$ ppm). The red dashed lines represent the mode orders. Modes are sorted first by order, then, within an order, by increasing diffraction loss.

5.3.3 Finite-sized mirror modes (FSMM)

The HGM are solutions to the paraxial Helmholtz equation considering infinite-sized-mirror spherical resonators. In reality, mirrors have a finite size that originates diffraction losses; inasmuch as the transverse beam profile is broadening while increasing the mode order, high order modes will suffer even more from this effect. Therefore, HGM may not be good enough approximations to describe the transverse optical modes of a finite-sized-mirror resonator. In the following, I numerically find solution of the paraxial Helmoltz equation with arbitrary boundary conditions (arbitrary mirror size and shape).

Amplitudes, Gouy phases, and diffraction losses

Consider the linear system introduced in fig. 5.2, where the input is the optical field to the right of M_1 (that is to say the input wave after its transmission through M_1), and the output the same wave after a single round trip; respectively, their complex amplitudes correspond to E_{20} and E_{21} in fig. 5.3, which will be recalled E_1 and E_2 here for convenience. The conditions for a wave to be a mode is that it retraces both its amplitude (to within a constant) and phase (to within an integer multiple of 2π) after a cavity round trip, i.e.,

$$E_2(x,y) = \mu\, E_1(x,y), \tag{5.46}$$

$$arg(\mu) = q\, 2\pi, \tag{5.47}$$

where μ is then the multiplicative factor of a single round trip, i.e., $r_1\, r_2\, e^{jk2L}$. On the other hand, the linear system can be written as [77]

$$E_2(x,y) = \iint\limits_{-\infty}^{+\infty} K^{12}(x,y;x',y')\, E_1(x',y')\, dx'dy', \tag{5.48}$$

where $K^{12}(x,y;x',y')$ represents the contribution of the input at x' and y' to the output at x and y. In linear systems theory, such a function is called the *impulse-response function*, for it is the output of the system if the input is an impulse signal (Dirac delta function). Substituting eq. (5.46) in eq. (5.48) yields

$$\iint_{-\infty}^{+\infty} K^{12}(x, y; x', y')\, E_1(x', y')\, dx'dy' = \mu\, E_1(x, y). \tag{5.49}$$

This becomes an eigenvalue problem where the eigenfunctions E_{lp} are the transverse optical modes' amplitudes, and the eigenvalues μ_{lp} are the associated multiplicative factors, from which can be extracted the diffraction losses and the Gouy phases. The determination of the transverse optical modes is not straightforward, but, considering some crucial simplifying assumptions, which are actually very-well describing this problem, the eigenvalue problem becomes tractable. These assumptions are *(i)* the dimensions of the resonator are much larger than the wavelength (paraxial approximation), and *(ii)* the field travelling within the cavity is essentially transverse electromagnetic (TEM) [78]. This eigenvalue problem is solvable insofar as the function $K^{12}(x, y; x', y')$ is known. After a single trip, the contribution of the optical field at x' and y' to the optical field at x and y is described by the propagator $K^{12}(x, y; x', y')$ as

$$K^{12}(x, y; x', y') = \frac{jk}{2\pi}\, \frac{\exp\left[-jk\, \rho(x, y; x', y')\right]}{\rho(x, y; x,' y')}, \tag{5.50}$$

where $\rho(x, y; x,' y')$ is the optical path length between the input position and the output position.

However, solving the integral equation is tedious and only yields low-loss modes [80]. That is why another technique has been developed and is introduced in [80]. The idea is to convert the integral equation to a matrix equation by kernel expansion. The eigenvalue problem becomes

$$K\, E = \mu\, E \iff (K - \mu\, \mathbb{I})\; E = 0, \tag{5.51}$$

where K is the propagator matrix, and $\mathbb{I}$ is the identity matrix. The propagator matrix is the operator for which the eigenfunctions and the eigenvalues need to be found. Using eq. (5.50) in eq. (5.49), one can then identity K from eq. (5.51):

$$K(x, y; x', y') = K^{12}(x, y; x', y')\, dx'dy', \tag{5.52}$$

where $K(x, y; x'y')$ is the value of the matrix K at the indices representing the passage from the position (x, y) to the position (x', y'), dx' and dy' are the mesh spacing on which the input field is computed, towards the x axis and the y axis respectively; in the following $dx = dy = dx' = dy'$.

Let us again specify a bit more the problem: what has been called *input* and *output* so far, are, in our case of an optical cavity, the mirrors IM and End Mirror (EM) already introduced in chapter 2. Thus, the propagation from the input mirror to the end mirror can be represented by the propagator matrix $K^{\mathrm{IM}\to\mathrm{EM}}$, and the propagator of a cavity round trip is

$$K^{\text{round trip}} = K^{\mathrm{EM}\to\mathrm{IM}}\, K^{\mathrm{IM}\to\mathrm{EM}}. \tag{5.53}$$

Once the propagator matrix is known, the eigenvalue problem

$$K^{\text{round trip}}\, E_i^{\mathrm{IM}} = \mu_i\, E_i^{\mathrm{IM}} \tag{5.54}$$

is tractable: the eigenvector E_i^{IM} is the amplitude fields of the i^{th} transverse optical mode at the input mirror, and from the eigenvalue μ_i are calculated the diffraction loss $\mathcal{L}_{d,i}$ and the Gouy phase ψ_i [78], as

$$\boxed{\begin{aligned} \mathcal{L}_{d,i} &= 1 - |\mu_i|^2, && (5.55)\\ \psi_i &= \arg{(\mu_i)}. && (5.56) \end{aligned}}$$

From the Gouy phase, the resonant frequencies in FSR unit $\nu_{i|_{\mathrm{FSR}}}$ are

$$\nu_{i|_{\mathrm{FSR}}} = \frac{\psi_i}{\pi}. \tag{5.57}$$

Then, to obtain the transverse optical modes at the end mirror, it suffices to multiply the eigenvectors of the input mirror by the propagator $K^{\mathrm{IM}\to\mathrm{EM}}$.

The simplification into a matrix eigenvalue problem allows us to compute the transverse optical modes of AdV's arm cavities. This mode basis will be referred to as 'FSMM'. For the study of OPIs in the next chapter, the optical modes of the cavities play an important role and the question that arises now is *'Does the choice between a finite-sized-mirror set of modes and an infinite-sized-mirror one yield notable different results?'*. That is what is going to be studied in section 5.4. But, first, some crucial tests need to be performed: convergence tests.

Required computation mesh size

A numerical computation forces a discretisation of the problem. Hence, the need of choosing a proper mesh on which to compute data: too thin and the computation will be too long or lead to a memory overflow, too wide and the computation will yield erroneous results. In the following, different tests of convergence will be shown for the HGM and the FSMM, and for two of the three quantities characterising a transverse optical mode, namely the diffraction loss, and the Gouy phase.

Notes on computation All of our computations and simulations are implemented in MATLAB® version 9.8.0.1323502 (R2020a) [81]. The diagonalisation of the kernel for the computation of the FSMM is done thanks to the function `eigs` [82].

Notation of the FSMM Unlike the HGM, the FSMM cannot be labelled with the two indices p and l. However, we are still able to define what the closest HGM order is (all of this will be shown in section 5.4). I sort the FSMM first by increasing mode order, and then, within an order, by increasing diffraction loss. Hence, the notation FSMM(n), with n starting from 1.

Diffraction losses The diffraction losses of FSMM are directly obtained from the eigenvalues of the numerical diagonalisation of the propagation kernel over a cavity round trip (see section 5.3.3); unlike the HGM's, they need not be estimated separately. To look for a convergence, I computed the diffraction losses of one hundred FSMM for different mesh sizes, namely for Γ from 30 to 210 (see section 5.3.2 for the definition of the grid thinness). The left panel of fig. 5.13 shows those diffraction losses for some FSMM; ten modes, chosen from low-order modes to high-order ones, representing the behaviour of all the sixty-five computed FSMM. Clearly, the grid thinness must be higher than 50. The right panel shows a zoom in of the left panel in order to better discern the small variations of non-absurd values; a grid thinness higher than 100 seems preferable; and if one were to be very picky, one would demand at least 150.

Gouy phase Regarding the FSMM Gouy phases, the same method as for the diffraction losses can be used. The results are shown in fig. 5.14. The behaviours of the Gouy phases with respect to the grid thinness are similar to those of the diffraction losses. One can do the same conclusions.

Convergence tests: conclusion According to what I have just showed, a grid thinness of more than 50 is required, more than 100 is preferable, and more than 150 would be optimal. In the following simulations, I use 120.

5.4 Comparison between Hermite-Gaussian modes and finite-sized mirror modes

A first benefit of the FSMM is that they do consider the finite (or the real) size of the mirrors, which better describes the real problem. Moreover, the diagonalisation of the kernel directly provides one with the diffraction losses of the modes, being more accurate as well. But a second benefit is that mirror shapes can be chosen arbitrarily, which enables one to introduce any deformation of

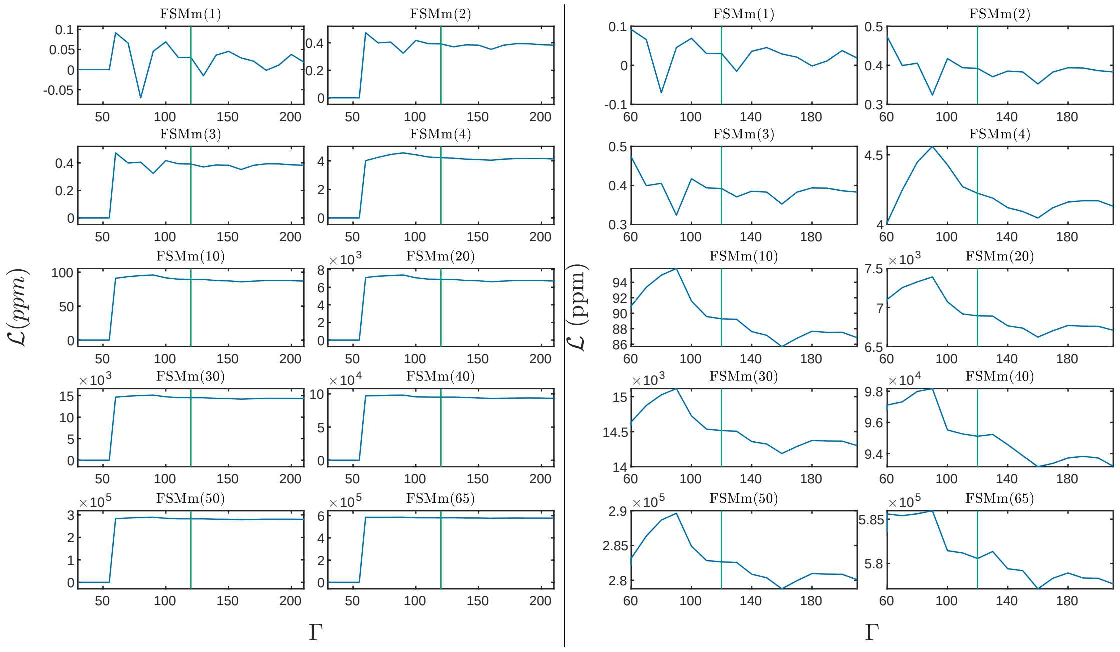

Figure 5.13: FSMM diffraction loss convergence tests: diffraction losses of ten FSMM for Γ from 30 to 210; the modes are arbitrarily chosen from low to high-order modes, and are representative of the whole. The right panel is a zoom (Γ from 60 to 210) of the left panel.

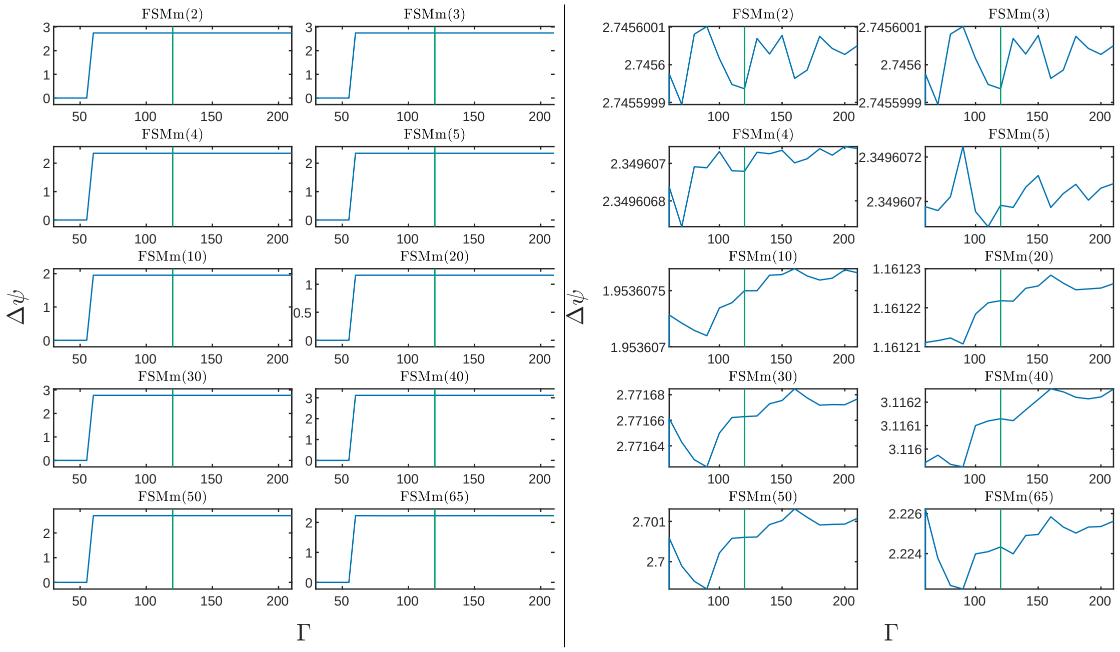

Figure 5.14: FSMM Gouy phase convergence tests: Gouy phases of ten FSMM for Γ from 30 to 210; the modes are arbitrarily chosen from low to high-order modes, and are representative of the whole. Note that the FSMM(1), which is the HG_{00}, is not shown because we set its Gouy phase to 0. The right panel is a zoom (Γ from 60 to 210) of the left panel.

the mirrors due to thermal effects or fabrication imperfections (genuine mirror maps characterised at the Laboratoire des Matériaux Avancés, Lyon, France). Note that fabrication imperfections were not included in this thesis and will be the subject of future work.

In the following, I analyse the differences in diffraction loss, mode amplitude, and Gouy phase between the HGM and FSMM basis sets. To do so, I sort the HGM following the same rule that I use for sorting the FSMM, that is to say first by increasing mode order, then, within a mode order, by increasing diffraction loss. Thus, we can use a single index as well (for instance HGM(1) stands for HG_{00}).

All the following results and conclusions on the comparison between these two sets of modes are part of an article submitted to *Physical Review A* [83].

5.4.1 Diffraction losses

Figure 5.15(a) shows the diffraction losses for both sets of modes. Figure 5.15(b) shows the linewidth differences between the two sets of modes, in unit of arm cavity linewidth. Except for the HG_{00}, the estimation method depicted in section 5.3.2 underestimates all HGM's diffraction losses. Note that the total losses of low-order modes are dominated by the input mirror transmittance $\mathcal{T}_{\mathrm{IM}} \approx 13\,760\,\mathrm{ppm}$ [84–87] (green line in fig. 5.15(a)). The mirror losses $\mathcal{L}_m$ for a cavity round trip are estimated to be around 75 ppm [62]. Hence, one can write $\mathcal{P} \approx \mathcal{T}_{\mathrm{IM}}$ (see section 5.1.3), and the difference in diffraction loss $\mathcal{L}_d$ between HGM(1) and FSMM(1) does not cause a significant difference in $\mathcal{P}$. According to fig. 5.15(a), the difference between the diffraction losses of FSMM and those evaluated for HGM amounts to about 10 % of the input mirror transmittance for mode orders greater than 4. Therefore, the linewidths of all HGM and FSMM of order lower than 5 are dominated by the input mirror transmittance: they are close to the measured cavity linewidth, which is 107 Hz for AdV (see eq. (5.19)). The diffraction losses of HGM and FSMM of order greater than 4, however, are no longer negligible compared to the input mirror transmittance; then, diffraction loss discrepancies between the two basis sets will lead to significantly different linewidths.

5.4.2 Mode amplitudes

In order to compare the mode amplitudes of FSMM and HGM, we decompose the vectors of one basis set onto the other, by using the decomposition coefficient c_{ij} of any FSMM (index i) with any HGM (index j):

$$c_{ij} = \iint\limits_{\mathcal{S}} dx\,dy\; u_i^*(x,y)\, v_{\mathrm{j}}(x,y), \tag{5.58}$$

where i and j are mode integer indices, u_i (resp. v_j) are the FSMM (resp. HGM) mode amplitudes and $\mathcal{S}$ is the mirror coating surface. Note that the energy of FSMM is distributed over a disc (mirror coating), whereas HGM's energy is distributed over the whole space such that a linear superposition of FSMM will never exactly match a HGM.

In fig. 5.16(a), I represent $|c_{ij}|^2$ for $i = 2$, and $j \in \{1, 2, ..., 36\}$. This figure is a representation of the decomposition of FSMM(2) on the HGM basis set. We find that FSMM(2) is a linear combination of the two order-one HGM: the HG_{01} and the HG_{10}. Additionally, we noticed that this is true for all low-order FSMM. It shows that the low-order FSMM amplitudes are always very close to the HGM ones, as they can always be decomposed within a family of HGM with same order. Conversely, as shown in fig. 5.16(b), the higher order FSMM(36) (high order mode arbitrarily chosen) mode cannot be decomposed on only a single order of HGM. In the presented case, it is a mixture of all odd orders from 7 on, though the higher the order, the lower their contribution.

After plotting the decomposition of all the FSMM up to the ninth order, we notice that this deviation initiates after order 6.

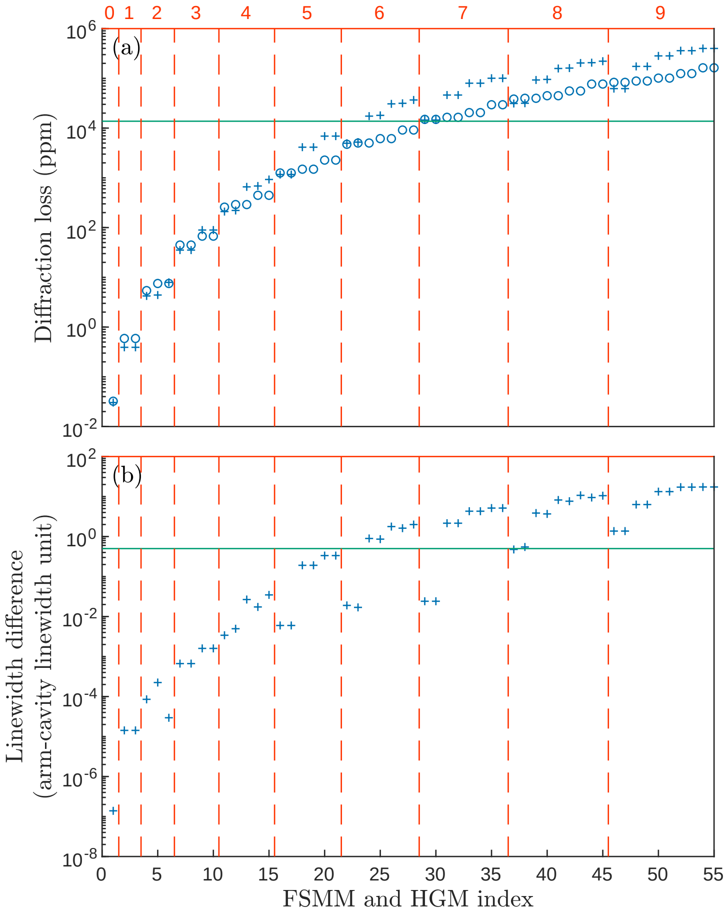

Figure 5.15: (a) Diffraction losses of FSMM (crosses) and HGM (circles). The green line shows the IM transmissivity. The red dashed lines represent the mode orders. Modes are sorted first by order, then, within an order, by increasing diffraction loss. (b) Linewidth difference between FSMM and HGM. It is shown in arm cavity linewidth unit, which is around 110 Hz. The green line highlights a linewidth difference of half an AdV's cavity linewidth.

5.4.3 Gouy phases

In section 5.4.2, I showed that, unlike low-order modes, high-order FSMM could not be described by a linear combination of HGM of a single order. Here, I show that unlike the HGM, the FSMM resonant frequencies cannot be determined simply by multiplying the HG_{00} Gouy phase shift by the order, as in eqs. (5.42) and (5.43).

Figure 5.17 shows the difference between HGM's and FSMM's Gouy phases, expressed in units of FSR (50 kHz) on the left vertical axis, and in units of cavity linewidth $\delta\nu$ (110 Hz) on the vertical right axis. To obtain this curve, the Gouy phases have been wrapped within an interval of length π, which allows to fold all the modes within a single FSR. The green line splits the graph into two regions: in the above region, for orders higher than 8, the deviation is more than half a cavity linewidth.

In chapter 3, we saw that the Gouy phase is definitely an important parameter, in that it sets the OPI resonance condition. We expect that, if the Gouy phase shift amounts to a frequency shift of less than half of the cavity linewidth, it will marginally impact the OPI gains.

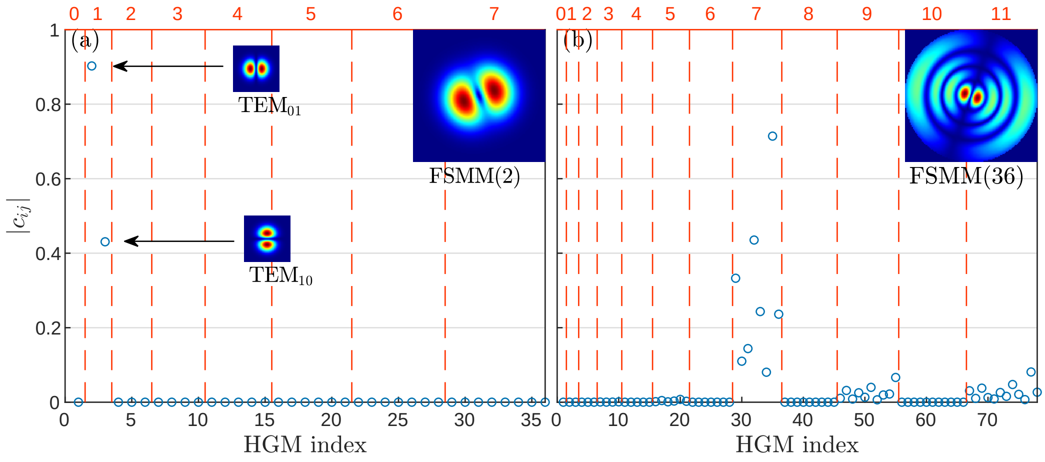

Figure 5.16: Decomposition of two FSMM on the HGM basis. The blue dots are the values of c_{ij}. The red dashed lines demarcate the mode orders. (a) c_{ij} of the low-order FSMM(2). Non-null values are all of order 1. (b) c_{ij} of the high-order FSMM(36).

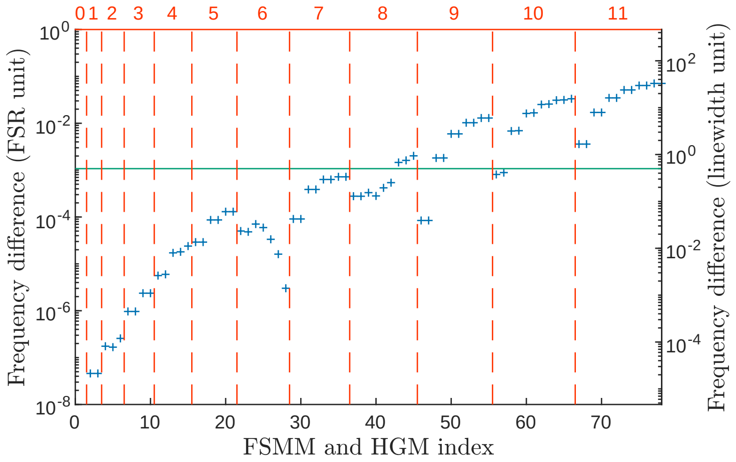

Figure 5.17: Frequency differences between the FSMM and their HGM partners. The left axis gives the difference in FSR unit (50 kHz) while the right axis gives it in cavity linewidth unit (110 Hz). The green horizontal line highlights a frequency difference of 0.5 linewidth unit.

5.4.4 Conclusion

For modes of order lower that 5, discrepancies between the two transverse optical mode basis sets do not lead to any consequence in terms of linewidth, mode shapes, and Gouy phases. Thus, there should be no consequences on the OPI gains. For mode orders of at least 5, the HGM basis might lead to wrong results in the OPI gains calculation. Therefore, we consider that for orders higher than 4, the more resource-consuming FSMM should be required.

5.5 Thermal effect

The laser energy is partially absorbed both by coatings and in the bulk of mirrors. This causes a temperature gradient, which originates two effects. First, a gradient of refractive index in the bulk of input mirrors modifies the mode matching condition but affects neither the cavity linewidth nor the mode frequencies. Second, a deformation of the mirror surface, which modifies the mode shapes and frequencies. In this section, I evaluate the impact of this second effect on the properties of cavity modes by comparing FSMM obtained for purely spherical mirrors with FSMM obtained for thermally deformed mirrors.

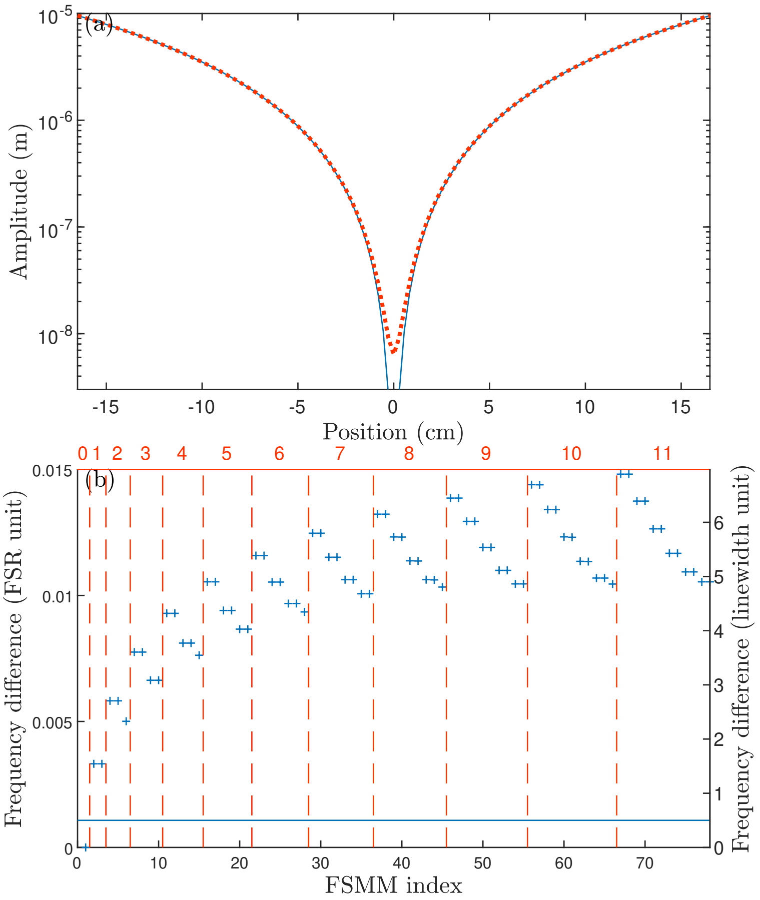

Figure 5.18: (a) Input mirror profiles with (dashed red line) and without thermal effect (blue solid line). (b) Frequency difference between FSMM modes with and without thermal effect. It is expressed in FSR unit (50 kHz) on the left axis, and in cavity linewidth unit (110 Hz) on the right axis.

The deformation profile is obtained by solving the linear thermoelastic equations [88]. Figure 5.18(a) shows the purely spherical and thermally deformed profiles of an AdV input mirror[6], for an intracavity power of 300 kW[7]. In the second case, we fit the centre part of the mirror to extract a radius of curvature. The results are shown in table 5.1.

In order to evaluate the incidence of this effect on the optical cavity parameters, we compute the FSMM with and without thermal effect on the two cavity mirrors. Figure 5.18(b) shows the frequency differences between the two situations. We see that optical modes acquire a different Gouy phase among a similar order, and that the frequency shift starts to be significant already for very low orders.

---

[6] The deformations profiles were obtained thanks to a code provided by Mikhaël Pichot du Mezeray (Artemis, Nice, France).

[7] This intracavity power is obtained for an input laser power of 50 W, which is the Observing Run 3 (O3) nominal value. Let us recall here eq. (2.35): $\mathcal{P}_{\text{intracavity}} \approx 6000\,\mathcal{P}_{\text{input power}}$.

Table 5.1: Radii of curvature of the NIM and the glsnem, with (blue) and without (red) taking into account the thermal effects.

	No thermal effect	With thermal effect
NIM	1424.6 m	1432.1 m
North End Mirror (NEM)	1695.0 m	1702.3 m

5.6 Summary

The arm cavities of AdV are built to improve the detector sensitivity by increasing the available optical power and effective length. The laser beam injected into the interferometer is a Gaussian beam, which will continue travelling within the cavities by bouncing back and forth between the two mirrors of the cavities, if the cavity is stable (see eq. (5.31)), and if the beam frequency matches the resonance condition (see eq. (5.8)). Thus, the circulating field sums up with the constantly entering field so that the cavity acts as an amplifier for selected frequencies (the different beam frequencies allowed in the cavity are the longitudinal modes). The optical gain of AdV's arm cavities is about 300.

In reality, the Gaussian mode, or fundamental mode, can scatter to higher-order transverse modes for various reasons, such as imperfections on the mirrors or a possible displacement of a mirror. The latter will be of interest in the next chapter. The photon energy levels that are authorised by the cavity are those respecting eq. (5.43). The beams fulfilling this equation can be calculated by solving the paraxial Helmholtz equation (eq. (5.23)). Considering a perfect spherical-mirror cavity whose mirrors are of infinite size, the HGM is one of the complete, countable, and infinite sets of modes solving the equation. It is a rather simple basis to use and it does not consume too much resource in terms of numerical computation. But it does not allow to consider fabrication imperfections for instance. Moreover, it cannot provide diffraction losses that must then be estimated. Here comes the interest of computing the transverse optical modes by a numerical resolution of the paraxial equation with finite-sized mirrors: we refer to this basis as FSMM. This basis has the advantage of better describing the modes of the cavity but is much more complex to solve and therefore requires more computing time.

The scattering from the fundamental mode to a higher-order one from the motion of a mirror is the source of the OPI of the next chapter. This instabilities are driven by the interaction between these aforementioned optical modes and a mechanical mode. That is why the choice of the transverse optical mode basis is crucial in our study. Hence, I have compared the two transverse optical mode bases with respect to three parameters characterising an optical mode: its diffraction loss (losses playing on the resonance linewidth), its amplitude shape, and its Gouy phase (setting the resonant frequency). I have shown that low-order modes (up to 5) HGM and FSMM behave similarly and the choice of the basis does not change anything in terms of resonance linewidth, nor in terms of Gouy phase. Furthermore, for low-order modes, the passage from a basis to another can be done via a finite matrix: it is possible to decompose a FSMM of low order into a linear combination of HGM of the same order. Therefore, any operation on a FSMM can be transposed onto an operation of a finite linear combination of HGM, and vice versa. However, none of this is true for high-order modes. I have shown that the two bases eventually depart from each other and the HGM basis is no longer precise enough to describe the transverse optical modes of the cavities. That is why we have chosen to use the FSMM basis, although it is much more resource-consuming.

Chapter 6

Optomechanical parametric instability gain computation in the Advanced Virgo configuration

In chapter 3 was introduced the phenomenon of optomechanical parametric instability (OPI) within the interferometric gravitational-wave detectors. I defined the mechanical parametric gain thanks to which we can now estimate the potential unstable mechanical modes of Advanced Virgo (AdV) in the Observing Run 3 (O3) and Observing Run 4 (O4) configurations.

This chapter focuses on these computations. First, an introduction on the numerical computation that we performed is given: the code and its input parameters, the validation of our framework, and the various configurations. Second, the impacts and effects on the OPIs of various parameters, namely the mirrors' radii of curvature, the diffraction losses, and the optical mode bases are discussed. Then, I confront the impact of the arm cavities, the Power Recycling Cavity (PRC), and the Signal Recycling Cavity (SRC). The simulation results are shown in the last sections of this chapter. They allowed us to track the OPI event observed by AdV in January 2020. Then, as O4 has not started yet, the Virgo collaboration needs to know the interferometer's OPI behaviour considering O4 parameters.

6.1 Numerical computation and its validation

6.1.1 Program and parameters

I have written an object-oriented MATLAB® program implementing the classical feedback system method that has been introduced in section 3.3. All the results presented in the following are obtained with this program. It requires a few inputs: mechanical modes that are obtained by finite element analysis (FEA) simulations combined with quality factor (Q factor) measurements (see section 4.1); optical modes obtained with different mirror models (see section 5.3). Ultimately, the program provides us with the prefactors, the optical transfer coefficients G_n, the spatial overlap parameters $B_{m,n}$, from which it derives the parametric gains R_m for all mechanical modes m. A block diagram in fig. 6.1 helps visualise the whole OPI computation process.

The parameters that are used are those of table 4.1 and table 6.1. The mechanical Q factors are those labelled as Q_{inf} in fig. 6.1, which are the Q_{FEA} inferred by the Q_{meas} (see chapter 4). We chose this set of Q factors, for they are the most accurate ones. When the interferometer configuration considered is that of O3, the transmittance of Signal Recycling Mirror (SRM) is set to 1 and SRC's Gouy phase is set to 0 to mimic the absence of SRC.

6.1.2 Comparison with the Finesse software

To validate our code, we compared its results with those obtained with the Finesse software [89,90]. The parametric gain obtained with Finesse for one mechanical mode and two arm cavity mirrors

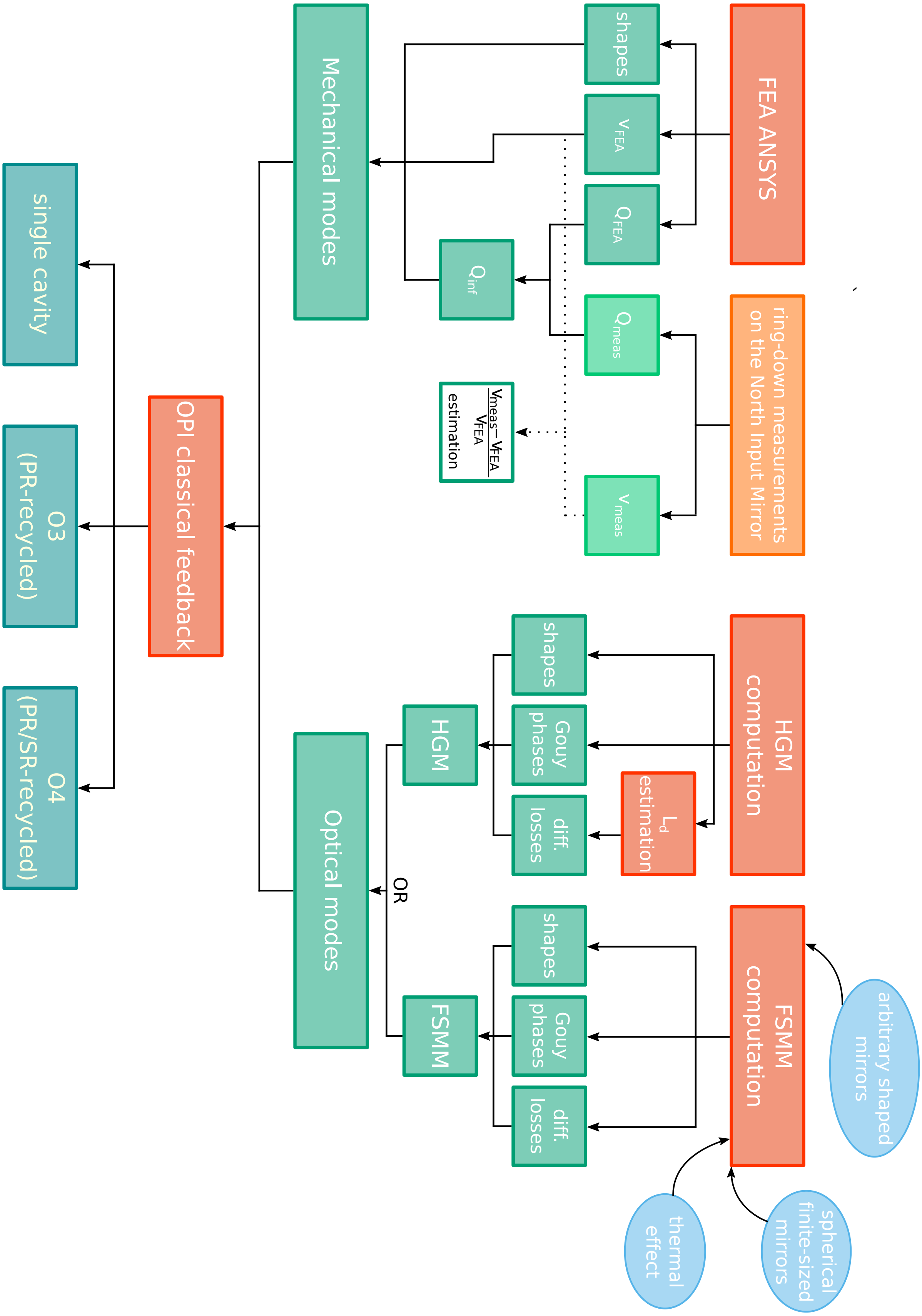

Figure 6.1: Block diagram summarising the links between computations and their outputs.

Advanced Virgo's O3 and O4 optical configuration parameters		
Arm lengths	2999.8	m
Transmittance NIM	13 770	ppm
Transmittance NEM	4.4	ppm
Transmittance WIM	13 750	ppm
Transmittance WEM	4.3	ppm
Transmittance PRM	48 400	ppm
Transmittance SRM	400 000	ppm
Round trip loss	75	ppm
Distance from BS to NIM ($L_{\text{BS-NIM}}$)	6.0167	m
Distance from BS to WIM ($L_{\text{BS-WIM}}$)	5.7856	m
Distance from BS to PRM ($L_{\text{BS-PRM}}$)	6.0513	m
Distance from BS to SRM ($L_{\text{BS-SRM}}$)	6.015	m
Intracavity power	300	kW
Laser wavelength	1064	nm
Gouy phase of PRC	1.8	mrad
Gouy phase of SRC	1.8	mrad
Radius of curvature of NIM	1424.56	m
Radius of curvature of WIM	1424.58	m

Table 6.1: OPI simulation optical parameters. For convenience, all acronyms have been used in this table. If they are not defined yet, please refer to the acronym table at the end of this thesis.

is shown in fig. 6.2(a). In fig. 6.2(b), I plot the relative difference between the OPI gain obtained by Finesse and the OPI gain obtained by eq. (3.3), using finite-sized mirror modes (FSMM) and Hermite-Gaussian modes (HGM). We note a difference of a few percent at maximum. The asymmetry between the blue (North End Mirror (NEM)) and red (West End Mirror (WEM)) curve stems from the small parameter differences between the two arm cavities. This comparison has been performed with many other mechanical modes and showed similar results. Note that using eq. (3.3) is much faster than using Finesse.

6.1.3 Comparison with Evans et al. article

In [55], **Fig. 4** shows the optical gains $G_n^{\pm}$ of a HG_{11} and the parametric gain $R_{m,\text{HG11}}$ of a mechanical mode (shown in fig. 6.3) with this HG_{11} optical mode, considering a single arm cavity. The aforementioned figure from [55] is given in fig. 6.4(a), while fig. 6.4(b) shows the outcome of our program, fed by aLIGO's input parameters provided in [55]. Note that [55] contains an error of a factor 2 in the parametric gain (as mentioned in [56]): to obtain this figure, one shall use the erroneous parametric gain formula.

6.2 Some interesting effects on the optomechanical parametric instability

6.2.1 Effect of the optical losses

In this section, I demonstrate a counter-intuitive effect of optical losses on the OPI gains. Intuitively, if optical losses increase, the parametric gains become lower since the optical linewidths increase as well. Here, I show that, if the OPI resonance condition is not exactly fulfilled, broadening the optical mode response can increase the gain such that the gain variation does not vary monotonously with the diffraction loss. This is best shown in fig. 6.5(a), where the parametric gain of a mechanical mode is plotted against the optical diffraction losses of the main optical contributor. In this example, the gain first increases from around 0.04 below 10^2 ppm to 0.1 at 2×10^4 ppm, before decreasing at higher loss values, as expected. This appears also in fig. 6.5(b),

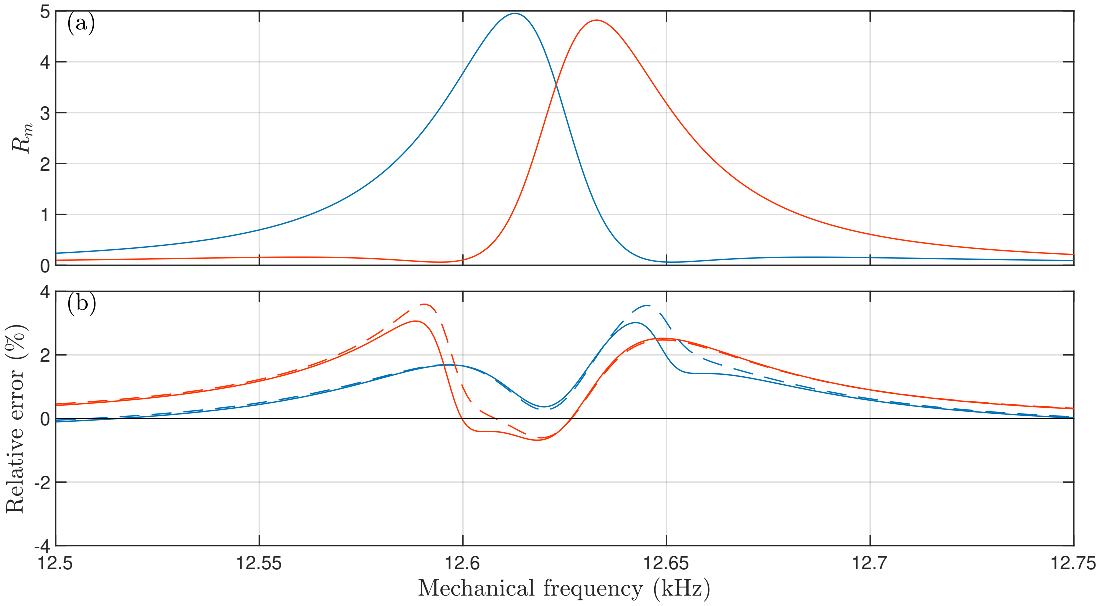

Figure 6.2: (a) OPI gain obtained with Finesse for one mechanical mode on mirror NEM (blue) and WEM (red). (b) Relative difference between (a) and the OPI gain obtained with eq. (3.3) using FSMM (solid lines) and HGM (dashed lines).

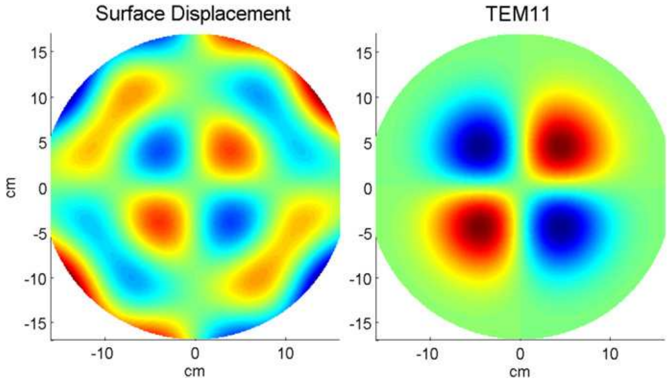

Figure 6.3: On the left: surface displacement amplitude normal to the surface $\mathbf{u_m} \cdot \mathbf{z}$ of a mechanical mode of an aLIGO arm cavity mirror near 30 kHz. On the right: basis function f_{HG11} of a HG_{11} optical mode. From [55].

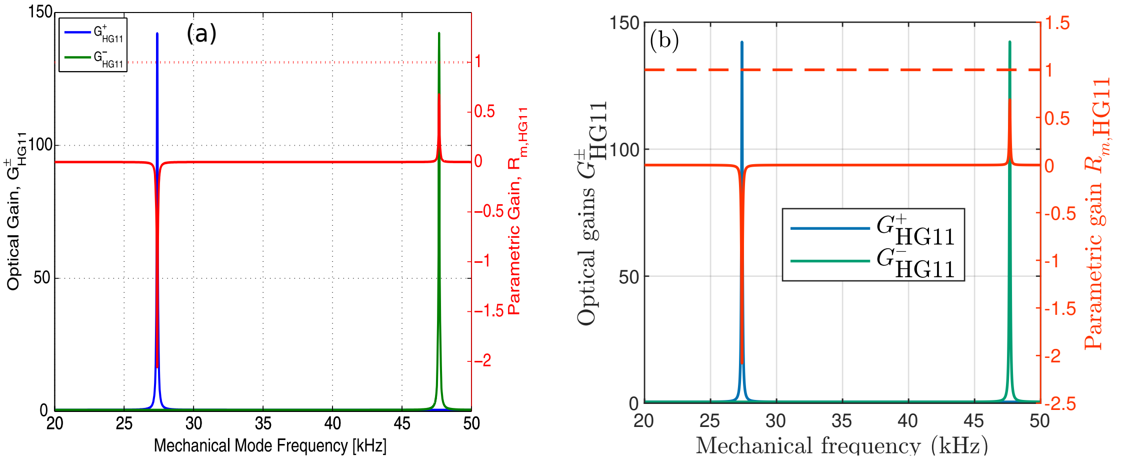

Figure 6.4: (a) **Fig. 4** from [55]: optical gains G^+_{HG11} and G^-_{HG11}, and parametric gain $R_{m,\mathrm{HG11}}$. m is a LIGO's mirror mechanical mode shown in **Fig. 3** of [55]. (b) Same data obtained by our program.

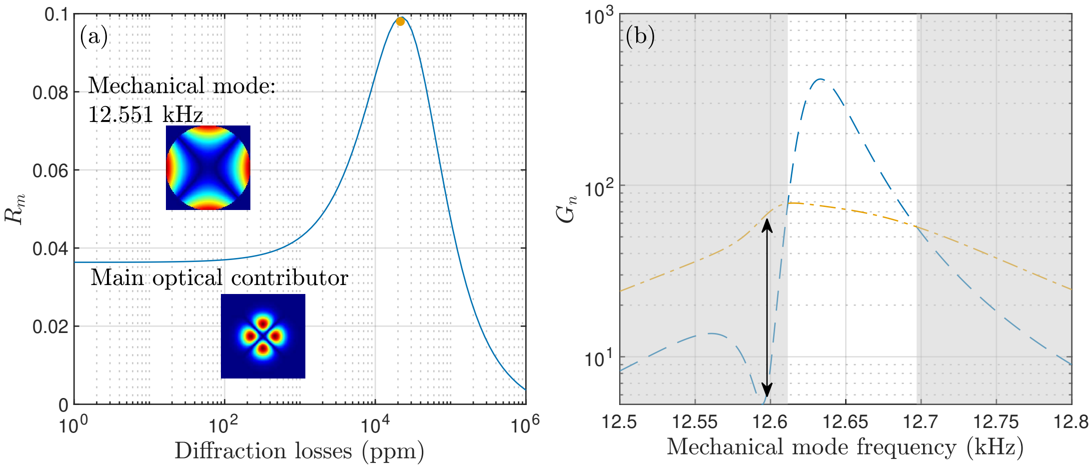

Figure 6.5: (a) R_m of a mechanical mode of frequency 12.552 kHz while varying artificially the diffraction losses of optical modes. (b) Optical gain G_n of the 12.552 kHz FSMM mode versus mechanical frequency for two arbitrary diffraction losses: the blue line is for a diffraction loss of 0 ppm, and the red one is for 21 540 ppm (red bullet at the peak on (a)). The arrow points the minimum between the two resonances on the blue curve and the disappearance of that minimum on the red curve. The grey-shaded area highlights a frequency band in which G_n is higher when the diffraction loss is higher.

where the optical gain G_n of the main optical contributor to the parametric gain of the mechanical mode of fig. 6.5(a) is represented as a function of the mechanical mode frequency, for two different values of diffraction losses. There exists a whole frequency region where the gain is higher for higher diffraction losses. At low losses, the two resonance peaks are well separated such that there is a minimum in between (black arrow). A loss increase from 0 to 21540 ppm (red bullet at maximum of fig. 6.5(a)) broadens the peaks and lead to the red curve, which has no minimum any more (black arrow), and which shows higher values in a whole frequency region (grey-shaded area on fig. 6.5(b)). Finally, if the losses were increased further, the red curve would start lowering and the grey-shaded area would vanish.

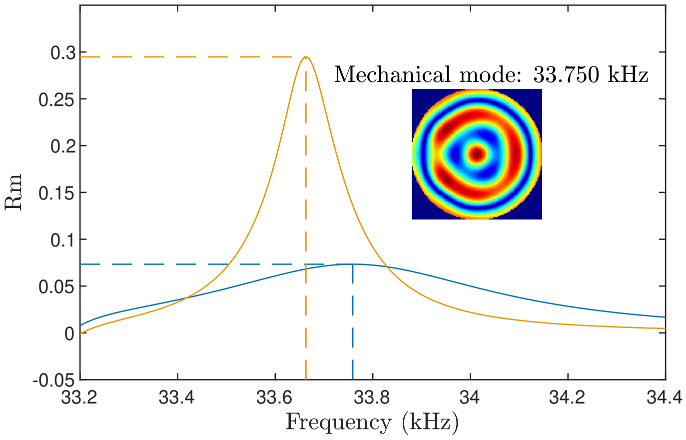

Figure 6.6: R_m of the 33.750 kHz mechanical mode (see inset) while artificially modifying the mechanical frequency, using the two different optical mode basis (red: HGM, blue: FSMM). The dashed lines point the maximums of the two curves, and emphasise the height and frequency change.

6.2.2 Impact of the optical mode basis

In this paragraph, I study the impact of the model used to compute the optical modes. I compare the OPI gains obtained with the HGM and FSMM bases. As explained in section 5.4, the HGM and the FSMM show significant discrepancies from order 5 and should give significantly different parametric gains at high order. Indeed, a Gouy phase shift causes a resonant frequency shift of the optical function transfer; a diffraction loss difference implies different linewidths, and, thus, a different optical gain; different shapes lead to different overlap parameters.

As expected, we find that there is only a marginal difference between the two models if optical modes of order below 5 are involved. In fig. 6.6, I plot the gain of a mechanical mode versus its frequency using the two optical mode basis sets. This mode has been chosen because the main optical contributor to the OPI gain is an order 6 mode. There is a factor 3 between the two gain maximums, and the two peaks are shifted by around 100 Hz, which corresponds to the optical linewidth. This is in agreement with the conclusions of section 5.4; therefore, the FSMM basis should be used.

6.2.3 Impact of a radius-of-curvature shift

Here, I study the impact on the gain of the radii of curvature of the optics. This will be useful to estimate how the uncertainty on the radii of curvatures propagates. Within a cavity, the radii of curvature R_{IM} and R_{EM} set the resonant frequency, in that they set the cavity Gouy phase: eqs. (3.10), (5.29), (5.30) and (5.35) for the HGM, and eqs. (3.10) and (5.56) for the FSMM. It is interesting to quantify the resonant frequency shift with respect to the radius-of-curvature shift. For this purpose, let us restrict to the HGM, since we have analytical formulas.

To do so, we calculate the derivative of the frequency expressed as a function of the radius of curvature of the End Mirror (EM). With eqs. (3.10) and (5.42) and setting the fundamental mode frequency to 0, the frequency in unit of Free Spectral Range (FSR) is

$$\nu_n(R_{\mathrm{EM}}) = -\frac{N_n \times \arccos\left(-\sqrt{g_{\mathrm{IM}} g_{\mathrm{EM}}}\right)}{\pi}, \tag{6.1}$$

and its derivative

$$\frac{d\nu_n}{dR_{\mathrm{EM}}} = \frac{N_n\, L_{\mathrm{AFPC}}}{2\pi R_{\mathrm{EM}}^2} \sqrt{\frac{g_{\mathrm{IM}}}{g_{\mathrm{EM}}}} \frac{1}{\sqrt{1 - g_{\mathrm{IM}} g_{\mathrm{EM}}}}. \tag{6.2}$$

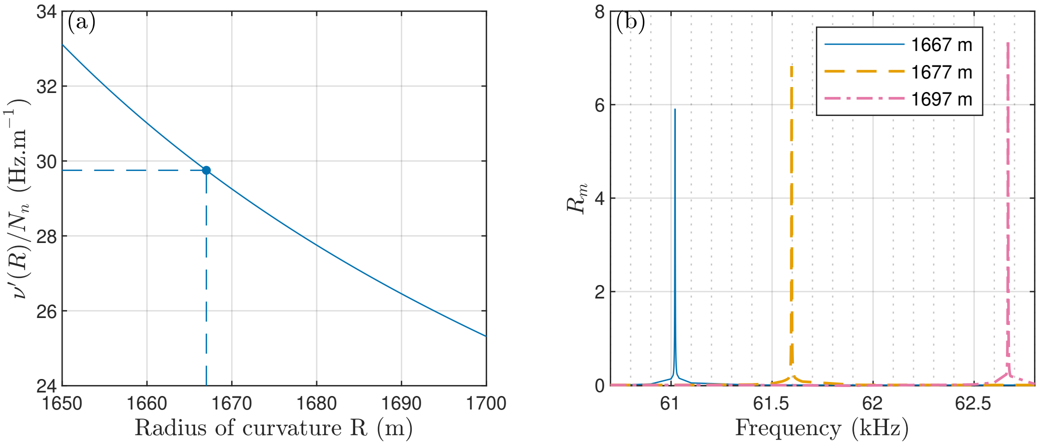

Figure 6.7: (a): $\nu'_n(R_{\mathrm{EM}})/N_n$ for an arm cavity, in AdV's configuration ($x = \{1, 2, 3, 4\}$, $L_{1,2,3,4} =$ 2999.8 m, and FSR ≈ 50 kHz). (b) parametric gain R_m of the mechanical mode of the third couple of fig. 3.6 for various radii of curvature. A radius-of-curvature shift ultimately leads to a frequency shit of the HOM, which, in turn, modifies the beat note, and then the optical resonant frequency. The optical mode is an order 2, then the frequency shift matches the one expected by (a).

Figure 6.7(a) shows the function $\frac{d\nu_n}{dR_{\mathrm{EM}}}$ for a Virgo arm cavity, i.e. $L_{\mathrm{AFPC}} = 2999.8\,\mathrm{m}$ and FSR $\approx 50\,\mathrm{kHz}$. Roughly, the frequency derivative is around $30 N_n\,\mathrm{Hz\,m^{-1}}$.

Figure 6.7(b) shows the parametric gain of the mechanical mode of the third couple of fig. 3.6 (again) against its frequency for different radii of curvature. There is a shift of around 600 Hz when the radius of curvature is shifted by around 10 m. This matches the expected value: the main optical contributor to this mechanical mode is an order 2 ($N_n = 2$); therefore the expected frequency shift is around $30 \times 2 \times 10 = 600\,\mathrm{Hz}$ for a 10 m-shift of the radii of curvature. However, the resonance not only is shifted, but also the maximum gain is modified. The reason is that a radius-of-curvature shift causes a beam radius shift, and the optical mode shapes are consequently modified; therefore, both the optical gain and the overlap parameter are modified.

6.3 Accounting for mechanical frequency and optical working point uncertainties

In chapter 4, it is shown that the frequency uncertainty standard deviation is $\sigma_{\mathrm{FEA}} = 0.15\,\%$. This uncertainty is equivalent to an uncertainty on the radii of curvature. We can assume that 99 % of the population is included within $\pm 3.5\sigma_{\mathrm{FEA}} = 0.5\,\%$ (see section 4.1). We have computed mechanical modes up to 157 kHz. Therefore, the highest uncertainty on the mechanical frequencies is around ±780 Hz, which can be much larger than optical resonance linewidths. Inasmuch as the mechanical frequency sets the actual optical gain, those uncertainties can strongly distort the OPI results.

In the end, we must then take into account both the uncertainty on the radii of curvatures and the uncertainty on the mechanical mode frequencies. This can be done by doing the simulation for a range of end mirror radii of curvatures around the nominal values. A frequency shift of 780 Hz matches a radius-of-curvature shift of around 25 m for the fundamental mode. Therefore, instead of looking for instabilities close to the estimated radii of curvature, we should compute the parametric gains for a radius-of-curvature range of approximately 50 m centred at the expected radius of curvature.

Another reason for scanning the radii of curvature of the EMs is that the envisioned OPI mitigation technique relies on a system that enables the tuning of the mirrors' radii of curvature.

It comprises Ring Heaters (RHs) that are around the mirrors: a surface deformation stemming from induced thermal gradients is used to fine tune the radii of curvature of the arm mirrors. Only the EMs are heated because if the substrate of the Input Mirrors (IMs) is heated, the mode matching condition is modified [91].

Note that in the O3 configuration, the designed radii of curvature of EMs are 1683 m [36]. However, the last measurement on site estimated it to be around 1667 m [62]. That is why the following OPI simulations will be shown over a range centred at that radius of curvature. This working point will be referred to as *'estimated working point'*.

6.4 Parametric gains for different optical configurations

I study here the impact of the different optical configurations, namely the single arm cavity, the full interferometer (interferometer with arm cavities), the power-recycled interferometer, and the power- and signal-recycled interferometer.

Figure 6.8 shows the positive parametric gains of all mechanical modes up to 70 kHz for the four configurations. The working point is 1669.3 m because it is a working point at which at least a mechanical mode is unstable in AdV's O3 and O4 configurations. This mode will be labelled D in the following. This logarithmic representation enables to distinguish some sort of lines on which more mechanical modes get higher gains; they are separated by the Transverse Mode Spacing (TMS) of about 6 kHz of AdV's arm cavities.

The impact of the full interferometer is not relevant compare to the impact of the recycling cavities, which multiply by more than 10 the parametric gain of the mechanical mode D. This is better shown in fig. 6.9, where only the parametric gain of the mechanical mode D is plotted, while artificially varying its frequency. The peaks of the parametric gain resonances in fig. 6.9 correspond to the parametric gains of fig. 6.8 because the working point corresponds to the resonant frequency (see table 6.5).

6.5 Observing Run 3 (O3): power-recycled interferometer

The O3 configuration is that of fig. 6.10. The O3 was actually split into two sub-runs: Observing Run 3a (O3a) from 1st April 2019 to 1st October 2019, and Observing Run 3b (O3b) from 1st November 2019 to 27th March 2020. In the meantime, AdV was being commissioned to increase the input laser power from 18.5 W to 27 W, which is still twice less than the AdV's O3 nominal input power. The OPI event observed by AdV occurred during O3b, after the input power increase. Until then, Virgo had probably never faced any OPI because its mirror Q factors are very low ($< 10^7$).

Prior to that experimental observation of an OPI, we computed 1600 mechanical modes, from 5.7 kHz to 70 kHz. We did not think it would be useful to compute more modes as aLIGO experienced its instability at 15.54 kHz (fig. 3.4) and as the parametric gain is inversely proportional to the square of the mechanical frequency (eq. (3.3)). But, an OPI was finally observed around 155 kHz; therefore, we expanded the mechanical mode computation up to 157 kHz, adding, thus, 11 150 more mechanical modes to the simulation. The mechanical frequency limit at 157 kHz is minorised by the need to include sufficient mechanical modes whose frequencies are around 155 kHz, and majorised by the increase of mechanical mode density at high frequency.

6.5.1 O3: up to 70-kHz mechanical modes

In the following, I show two sets of results. Each figure is the result of the same parametric gain calculation but using a different set of optical modes. Figure 6.11(a) shows the results for FSMM, fig. 6.11(b) for FSMM including thermal effects due to coating absorption (see section 5.5). The input power is the nominal one (50 W). NEM and WEM are scanned over a five-meter range, which is within reach of the mirror RH system. In each OPI plot, the colour code is chosen such that the grey-shaded scale is for gains lower than 1 (no instability), and the colourful scale

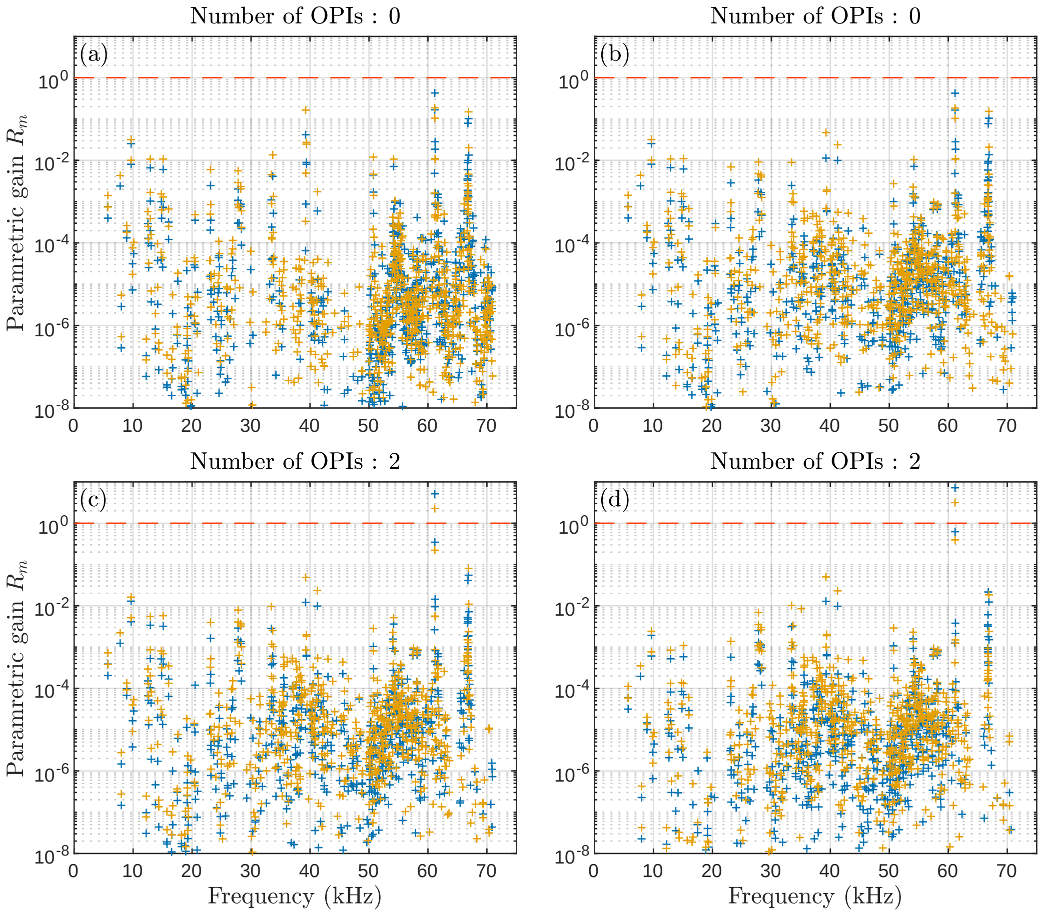

Figure 6.8: Parametric gains R_m for all mechanical modes up to 70 kHz of the IM (blue crosses) and EM (red crosses), at 50 W input power. The red dashed lines highlight $R_m = 1$. (a) Single arm cavity. (b) Full interferometer. (c) Power-recycled interferometer. (d) Power- and signal-recycled interferometer.

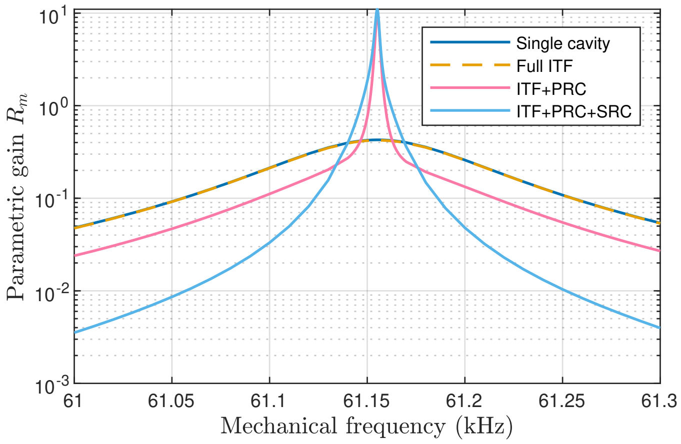

Figure 6.9: parametric gain R_m of a mechanical mode near 61.15 kHz while artificially modifying its frequency, for the four different configurations, at 50 W input power.

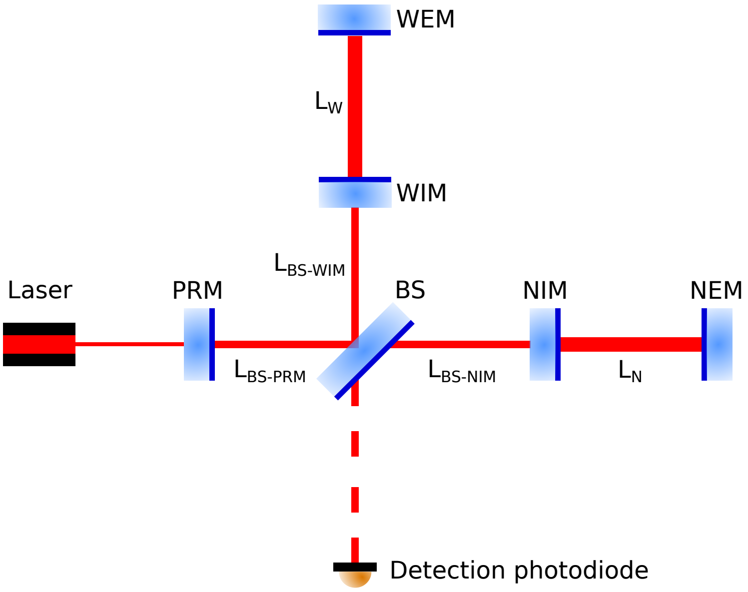

Figure 6.10: AdV's O3 configuration.

is for $R_m > 1$ (instability). The involved mechanical modes are indicated by the arrows and corresponding letters; they are represented together with their main optical modes contributors at the bottom, in fig. 6.11(c resp. f). Note that the results obtained with HGM are indistinguishable from that of fig. 6.11(a); therefore, I did not include the corresponding figure. Indeed, only low order optical modes are involved here such that HGM and FSMM give the same result. In fig. 6.11(c resp. f), I plot the number of unstable modes (red solid line) in the range of fig. 6.11(a resp. d) versus the optical power for FSMM without (resp. with) thermal effect. Modes that ring on different mirrors are counted only once; it is referred to as *'Number of unstable modes'*. The blue curve is the ratio of the area filled by instabilities $\mathcal{S}_{R_m>1}$ to the total area $\mathcal{S}_{\text{tot}}$ in fig. 6.11 (a resp. d) versus the optical power[1].

The three unstable mechanical modes without thermal effects are labelled D, E, and L; their frequencies are respectively 61.154 kHz, 61.160 kHz, and 66.784 kHz. The mechanical modes D and E ring with an optical mode of order 2, while the mechanical mode L rings with an order 3. They become unstable from an optical input power of respectively 9 W, 26 W, and 27 W; as the parametric gain is proportional to the input power, one can retrieve the parametric gains at any input power from those power values (at which $R_m = 1$).

Taking into account the thermal effects, three modes are unstable at the nominal input power: they are labelled M, N, and F; their frequencies are respectively 66.888 kHz, 66.912 kHz, and 61.216 kHz. They become unstable from an optical input power of respectively 4.6 W, 35 W, and 42 W. Two other mechanical modes, becoming unstable from an input power of respectively 51 W and 57 W; they are respectively labelled G and L, and their frequencies are respectively 61.231 kHz and 66.784 kHz. The contributions of each optical mode to the cited mechanical modes, together with the input power at which they become unstable ('critical input power'), are summarised in tables 6.2 and 6.3.

These results show that an OPI whose frequency is at most 70 kHz could have been observed at the nominal power of O3a, although it would have been easily escaped with the end mirror RHs since $\mathcal{S}_{R_m>1}/\mathcal{S}_{\text{tot}} \simeq 0.2$ at 300 kW intracavity power. They also show that the thermal effect caused by coating absorption has an important impact on the results at such high optical powers.

These results, too, are part of the article cited in section 5.4 [83].

---

[1] The maximum input power of 100 W is twice the nominal power of O4. Note, however, that O4 will have a different interferometer configuration.

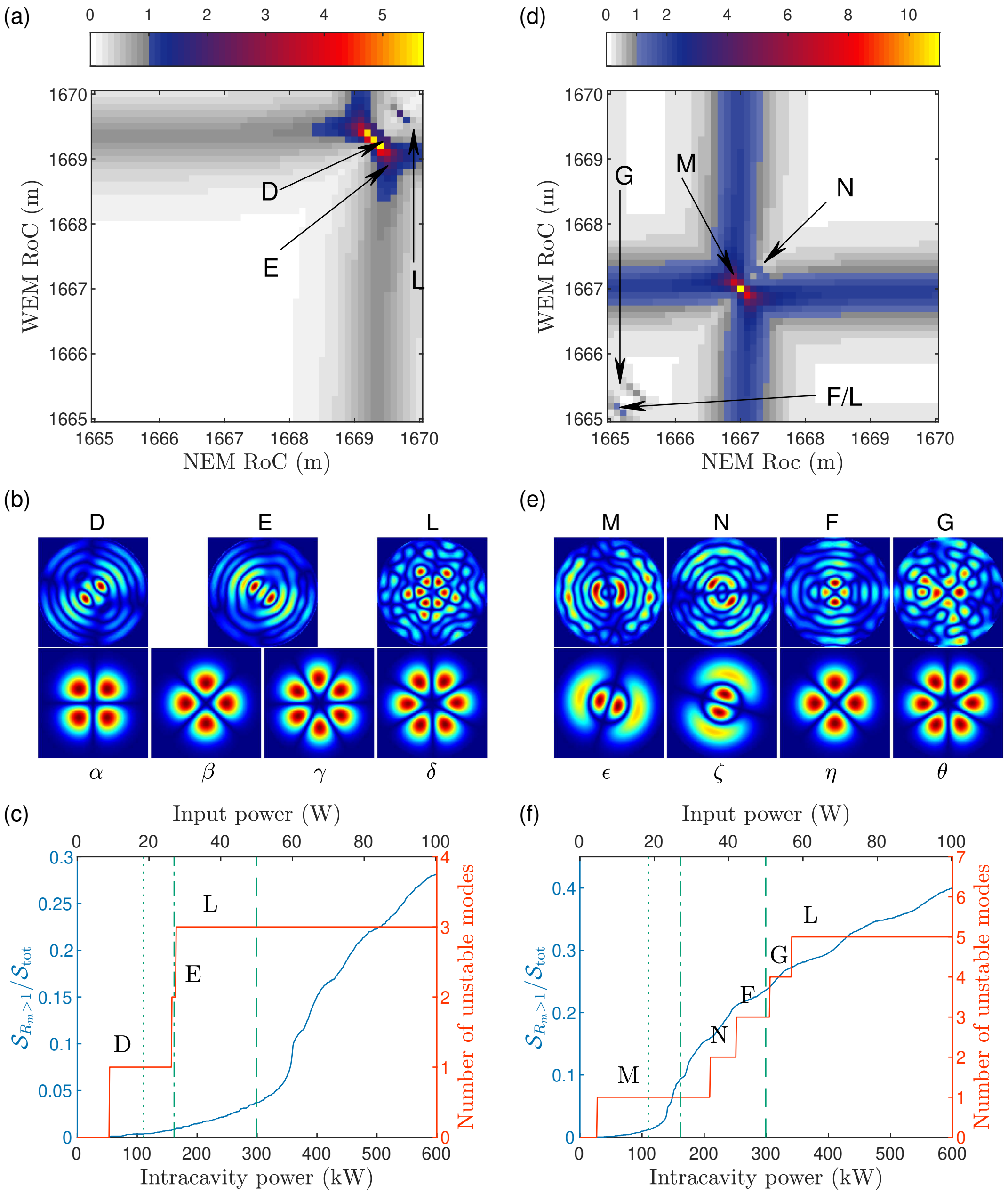

Figure 6.11: (a) R_m versus radii of curvature of NEM and WEM, using FSMM without thermal effect, for an input power of 50 W. The grey-shaded scale highlights the parametric gains lower than 1, while the colourful scale highlights the instabilities ($R_m > 1$). (b) The mechanical mode shapes and associated transverse optical mode contributing the most to the aforementioned instabilities. (c) The red solid line is the number of unstable modes in the radius of curvature range of (a), with respect to the optical input power (top) or intracavity power (bottom). The blue curve is the ratio of the area filled by instabilities $\mathcal{S}_{R_m>1}$ to the total area $\mathcal{S}_{\text{tot}}$ in fig. 6.11 (a resp. b) versus the optical power. The three dashed green lines highlight the input powers 18.5 W (O3a actual), 27 W (O3b actual), and 50 W (O3 nominal). The figures (d) resp. (e) resp. (f) are the same than (a) resp. (b) resp. (c), but taking into account the thermal effect.

	α (%)	β (%)	γ (%)	δ (%)	Critical input power (W)
D	93.3	5.5			9
E	77.3	15.2			26
L			89.3	10.2	27

Table 6.2: Optical contributions (in %) of O3 unstable mechanical modes, without thermal effect. Last column: input power at which the corresponding mechanical mode becomes unstable (in W).

	ϵ (%)	ζ (%)	η (%)	θ (%)	Critical input power (W)
M	83.7	16.3			4.6
N	24.3	75.7			35
F			99.9		42
G			99.9		51
L				97.1	57

Table 6.3: Optical contributions (in %) of O3 unstable mechanical modes, with thermal effect. Last column: input power at which the corresponding mechanical mode becomes unstable (in W).

6.5.2 O3b: OPI observation at Virgo around 150-kHz mechanical modes

On 7th January 2020 (during the O3b), an instability arose after a tuning of the working point with the RHs: the detection electronics saturated due to an exponentially growing up 155.408 kHz oscillation. It was soon identified as an OPI [92, 93] (article being written [62]). The rise time enables to retrieve both the mechanical Q factor (estimated at around 2×10^6) and the parametric gain (estimated as $1.4 < R_m < 10$); they will be referred to as respectively the *'estimated mechanical Q factor'* and the *'estimated parametric gain range'*.

Furthermore, the optical signal was visible on a phase camera of the arm cavity and let us know that this instability rang with an optical mode of order 1. This is an interesting piece of information, in that it enables to check whether an optical order 1 presents a resonance at around 155.4 kHz at a working point of around 1667 m; indeed, the radius of curvature sets the Gouy phase, and, thus, the resonant frequency, which varies according to the optical mode order (eq. (6.1)). Figure 6.12(a) shows the optical gain functions G_n for orders 1, 2, and 3: AdV's arm cavities indeed present an order-1 resonance ringing at around 155.4 kHz. It can be better seen in fig. 6.12(b). These resonances have been obtained numerically for a radius of curvature of 1666.25 m, which is pretty close to the measured working point (1667 m).

Then, we can compute the parametric gain of a custom mechanical mode. By *custom*, I mean that its Q factor is set to the estimated one (2×10^6), and its overlap with the two implied optical modes is set to 1, to mimic a good-enough spatial matching. Thus, we can compare this parametric gain to the estimated range ($1.4 < R_m < 10$). Figure 6.13(a) shows this parametric gain against the mechanical frequency; the estimated mechanical Q factor can yield an OPI that is within the estimated range. Should the overlap parameter be even lower, the parametric gain could still be within the estimated range. In fig. 6.13(b) is shown the same type of 2D map already shown in the previous section, except this time, only a single mechanical mode is considered, and its frequency and Q factor are set to the estimated values. The same conclusion arises as the highest parametric gain on the map is also within the expected range. In addition, it provides a second verification of the working point yielding a resonance at 155.408 kHz.

Finally, to further investigate, we can plot again fig. 6.13(a) but using the computed mechanical modes (and not the *custom* one). Thus, we can see whether there is at least a computed mechanical mode that has a parametric gain between 1.4 and 10 ringing with an order-1 optical mode, at a 155.408 kHz beat note (this type of plot allows to dispose of the computed mechanical mode frequency, and, thus, of its uncertainty too). In fig. 6.14, one can see that there are actually

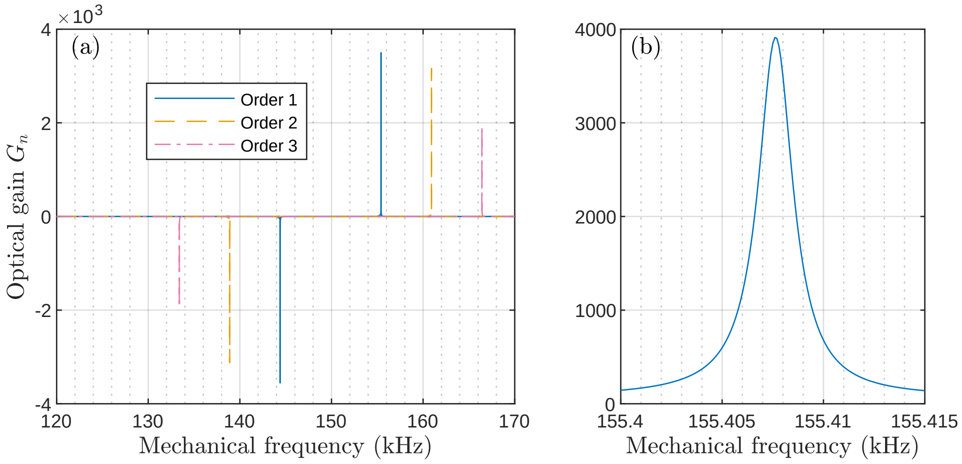

Figure 6.12: (a) The optical gains G_n of three modes: an order 1, an order 2, and an order 3. The order 1 has indeed a positive resonance around 155 kHz. (b) Zoom centred at the OPI event frequency 155.408 kHz. These resonances have been obtained for a working point at 1666.25 m.

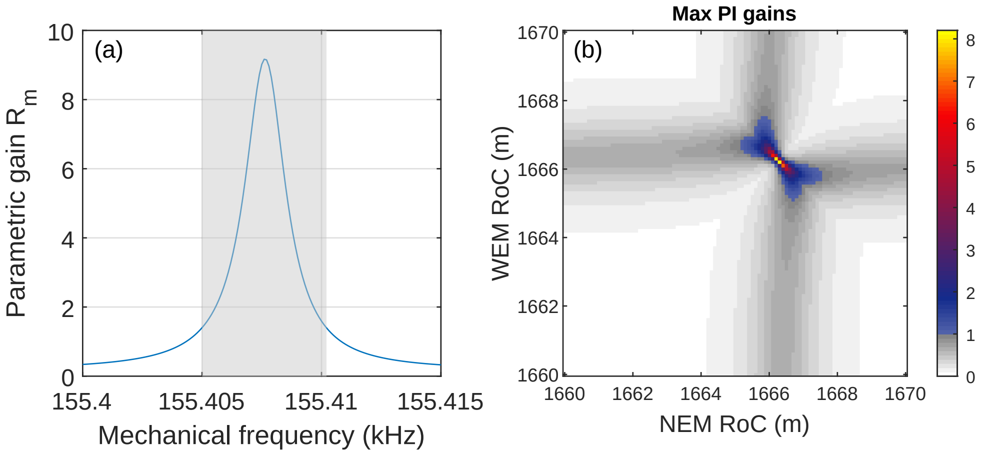

Figure 6.13: (a) Parametric gain R_m, while artificially modifying the mechanical frequency, for a custom mechanical mode with a 155.408 kHz frequency, a 2×10^6 Q factor, and an overlap of 1 with the two optical modes in play. Considering all the measured parameters of the OPI of 7th January 2020, our simulation indeed yields a parametric gain as $1.4 < R_m < 10$ (greyed area). (b) The maximum parametric gain of the same custom mechanical mode for different working points. Again, the parametric gain matches that expected, and the resonant Gouy phase is around the measured working point as well.

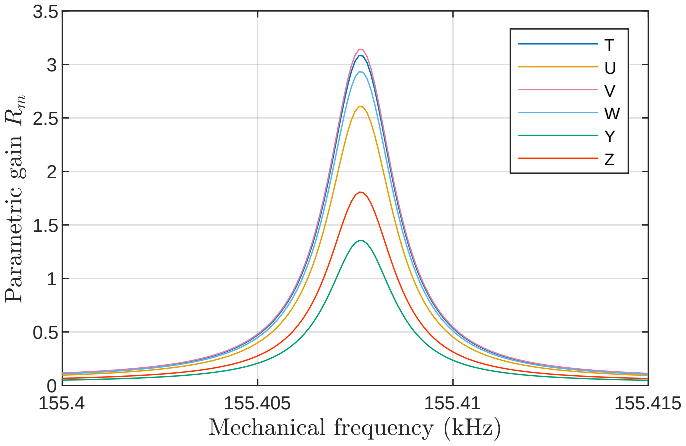

Figure 6.14: Parametric gain R_m, while artificially modifying the mechanical frequency, for all computed mechanical modes whose resonance rings with a gain R_m as $1.4 < R_m < 3.7$. The frequencies of these computed mechanical modes are comprised from 155.756 kHz to 155.827 kHz, which is roughly 385 Hz away from the measured frequency.

some of them: the frequencies of all these modes are comprised from 155.756 kHz to 155.827 kHz. Therefore, we can estimate the unstable mechanical frequency uncertainty to be around 385 Hz; endorsing the expected uncertainty.

6.5.3 O3: conclusion

From the simulation of O3a, first, we learn that the AdV's OPI density is very low; therefore, even though AdV could have experienced an OPI during O3a, it would have been easily mitigated thanks to the RHs. Also, AdV did not experience any OPI during O3a. The OPI density can be drastically increased if the mechanical Q factors are 10 to 100 times higher. For example, fig. 6.15 is the same as fig. 6.11(a) except that all mechanical Q factors have been set to 10^7. One can see that the OPI density is much higher: there is almost no working point zone at which no mechanical mode is unstable. That might explain why Virgo is less likely to face an OPI. Furthermore, we are comparing two interferometers in two different configurations: AdV's O3 configuration has no SRC, whereas aLIGO does. Therefore, it can be understandable that aLIGO faces OPIs while AdV does not, even with a lower input power. Second, we learn that the thermal effects have a non-negligible impact at such high powers.

The OPI experimental observation of 7th January 2020 permitted us to compare our code to genuine data. By setting our simulation parameters to the values measured from these data, we find that we do have mechanical modes that could be good candidates, that is, that have a Q factor around 2×10^6, a resonance with an order-1 optical mode at the measured frequency of 155.408 kHz, around the measured working points of 1667 m, and whose parametric gain is between 1.4 and 10. Moreover, it provides us with a good estimation of the unstable mechanical mode frequency error, confirming that we must perform simulations over a range of at least 30 m for the EM radii of curvature to take all possible uncertainties into account. So one could say that what was an issue for Virgo, was actually a marvellous opportunity for the OPI team.

6.6 Observing Run 4 (O4): power- and signal-recycled interferometer

After the end of O3, the AdV detector is being upgraded in two different phases, called Advanced-Virgo+ Phase I and Phase II, which will respectively lead to O4 and O5. During the first upgrade, an additional mirror (SRM) will be included in the optical configuration and the input power

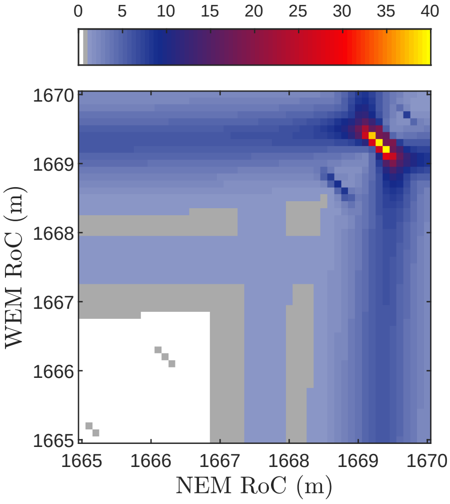

Figure 6.15: R_m versus radii of curvature of NEM and WEM, using FSMM without thermal effects, at 50 W input power (nominal power). All mechanical Q factors are set to 1×10^7. The grey-shaded scale highlights the parametric gains lower than 1, while the colourful scale highlights the instabilities ($R_m > 1$).

will be doubled. Subsequently, the installation of larger END mirrors will be performed, and the optical configuration will be redesigned during the AdV+ Phase II. In both cases, the optical configuration of the interferometer will be different with respect to the current one, and a new simulation campaign is being performed in order to study the possibility that new OPIs could arise.

The main new feature of O4 is the insertion of the SRM (see section 2.2.2). The AdV's O4 optical scheme is represented in fig. 6.16. As explained in section 2.2.2, the SRC is designed in such a way that the sidebands are resonant, whereas the arm cavities are designed so that the carrier is resonant. Therefore, intuitively, one can imagine that certain HOMs could 'live' longer within the interferometer by being resonant in the SRC. Hence, optical modes with lower diffraction losses, implying thinner resonances but higher gains. Gurkovsky et al. confirmed in [94] that a signal-recycled interferometer is less likely to fall into an OPI trap because its optical linewidths are smaller.

Figure 6.17, like fig. 6.11, shows the maximum parametric gains while making the END mirrors' radii of curvature vary, considering the same input power, that is to say 50 W. Indeed, although the actual input power will be doubled from O3 to O4, the nominal one is finally the same. But, the main interest lies in the fact that, this way, the only visible impact is that of the SRC; to ensure this, we also take into account the same mechanical modes as in section 6.5.1 in the computation. The three unstable mechanical modes are labelled D, E, and L; they are the same ones as in fig. 6.11, as expected. Their frequencies are respectively 61.164 kHz, 61.160 kHz, and 66.784 kHz. They become unstable from an optical input power of respectively 6.7 W, 17 W, and 24 W. Table 6.4 summarises these critical input powers, together with the optical mode contributions. We do observe what was expected: the maximum parametric gains are higher, and the resonances are sharper. The former statement can also be verified by noticing that the critical input powers are lower than those of O3. The latter causes a lower density of instabilities, which can be verified thanks to the ratio $\mathcal{S}_{R_m>1}/\mathcal{S}_{\text{tot}}$ in fig. 6.17(b). Note that the instability density profile evolution in 'steps' is a direct effect of the sharper resonances.

This first study of O4 permitted to endorse our intuitions on the SRC impact, as well as what was foreseen in [94]. The next step is to compute the parametric gains of all the mechanical modes that we have obtained, that is, the 12 750 modes up to 157 kHz. Also, due to the mechanical frequency uncertainties, we need to compute for many more working points: an interesting range

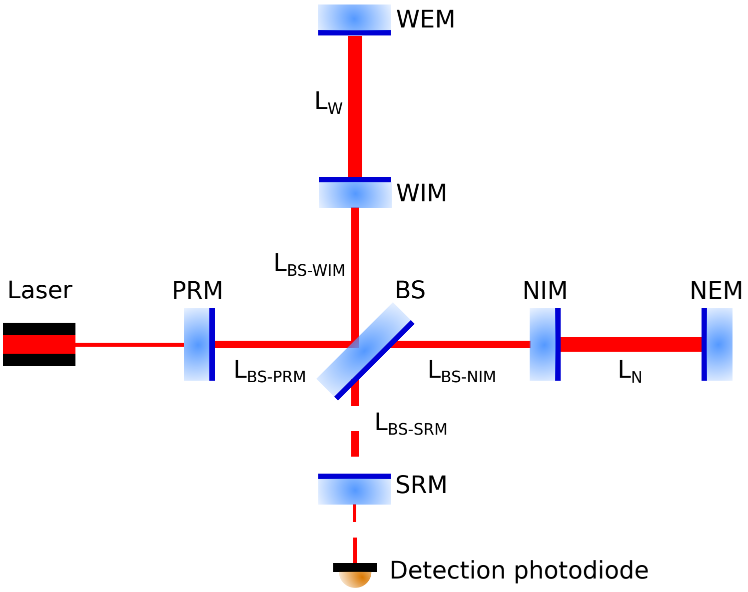

Figure 6.16: AdV's O4 configuration.

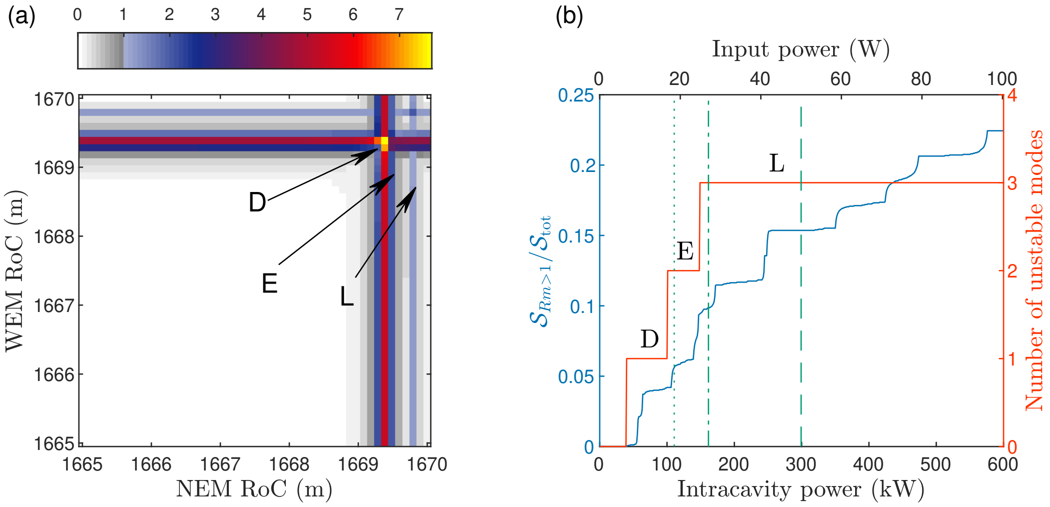

Figure 6.17: (a) R_m versus radii of curvature of NEM and WEM, using FSMM without thermal effect, at 50 W input power (nominal power); the mechanical modes are the same 1600 modes up to 70 kHz. The grey-shaded scale highlights the parametric gains lower than 1, while the colourful scale highlights the instabilities ($R_m > 1$).
(b) The red solid line is the number of unstable modes in the radius of curvature range of (a), with respect to the optical input power (top) or intracavity power (bottom). The blue curve is the ratio of the area filled by instabilities $\mathcal{S}_{R_m>1}$ to the total area $\mathcal{S}_{\text{tot}}$ in (a) versus the optical power. The three dashed green lines highlight the input powers 18.5 W (O3a actual), 27 W (O3b actual), and 50 W (O3 and O4 nominal). The O3 powers are left for comparing with fig. 6.11.

	α (%)	β (%)	γ (%)	δ (%)	Critical input power (W)
D	93.3	5.5			6.7
E	77.8	15.3			17
L			2.7	96.7	24

Table 6.4: Optical contributions (in %) of O3 unstable mechanical modes. Last column: input power at which the corresponding mechanical mode becomes unstable (in W).

would be ±25 m around the expected working point, that is, from 1640 m to 1690 m. However, inasmuch as the computation time is roughly proportional to the number of mechanical modes and the number of working points, such a simulation would be approximately 200 times longer than the simulation[2] for fig. 6.11! Hence fig. 6.18: only five consecutive $5\,\mathrm{m} \times 5\,\mathrm{m}$ ranges along the diagonal have been chosen to compute the parametric gains of the 12 750 mechanical modes. This should provide enough information, in that the maximum gains (and the minimum ones) are more or less on the diagonal on the one hand, and the AdV's working point is usually more or less on the diagonal on the other hand.

The potential unstable mechanical modes are summarised in table 6.5. This table also shows the maximum possible deviation due to uncertainties (±0.5 %) from the calculated mechanical frequency, together with the associated radius-of-curvature deviation, which takes the optical contributor order into account. This allows us to dismiss some mechanical modes if the working point remains the same during O4; these modes are those for which $|R_{|m} - 1667| > \Delta R_{\max}$ (dark blueish green). One can recognise that all of these modes were already in play previously: those that ring very close to the measured working point and those among which one, at least, has an frequency uncertainty making it ring at our measured working point. But, they all have higher parametric gains.

We can conclude that, in O4, the odds that AdV experience another OPI are rather high: the resonances are at the same frequencies than for O3 and their amplitudes are even higher. If the working point remains the same, we will be close to the same instability of January 2020 except that the parametric gain will be higher, which decrease the rising time of the OPI eq. (3.2). By the way, due to all the commissioning work in progress, the working point might be pretty different once O4 is started. Be that as it may, another interesting conclusion of these simulations is that, indeed, the resonance linewidths are much sharper, both in terms of frequency or radius of curvature; therefore, crossing over an instability should even be easier than in O3.

6.7 Summary and conclusion

The study of OPIs within the Virgo Collaboration was made first for O3 configuration; it was actually mostly performed during the run and had to pass a series of validation tests and others; hence, it could not be used as a prevision of AdV's OPI behaviour. However, it helps us understand that if AdV had never faced any OPI, it not only was a lucky strike, but also a behaviour that seems to be pretty general in the O3 configuration. Regarding the intracavity power of O3 (relatively high compare to that of aLIGO when they encountered an OPI for the first time), the main criterion that can explain such low parametric gains is then the fact that mechanical AdV's Q factors are much lower than aLIGO's. We did see how the instability density increases when we artificially increase the mechanical Q factors to one or two higher orders.

On 7th January 2020, Virgo, 'at last', encountered an OPI following a working point tuning. This event allowed us to confront our code to a real situation and we did find an agreement between them. This is how we eventually feel highly confident in our simulations and results.

For the next Observing run (O4), AdV's configuration will be rather different that the previous one, as the SRC will be installed. This extra cavity, resonant for the sidebands and anti-resonant

---

[2] This simulation takes about 2–3 days.

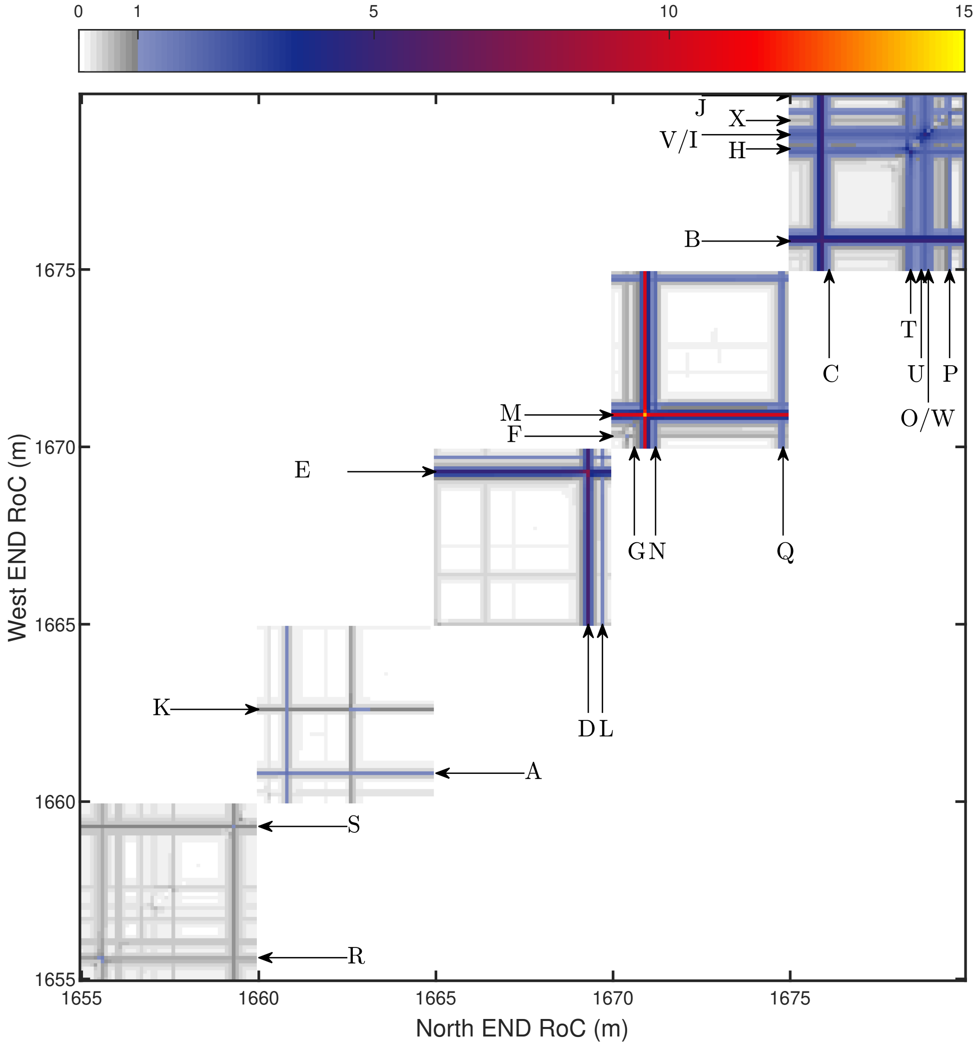

Figure 6.18: (a) R_m versus radii of curvature of NEM and WEM, using FSMM without thermal effect, at 50 W input power (nominal power), for the O4 configuration; the mechanical modes are all the 12 750 modes up to 157 kHz. The grey-shaded scale highlights the parametric gains lower than 1, while the colourful scale highlights the instabilities ($R_m > 1$). Any mechanical mode's resonance can be seen on both arm cavities; however, for a matter of clarity, only a single arm cavity is pointed for each unstable mechanical mode, and the choice of the pointed axis is motivated by nothing but clarity.

Label	Frequency (kHz)	$\Delta\nu_{\text{max}}$ ($\pm 10^2$ Hz)	Optical order	R (m)	ΔR_{max} ($\pm$m)	R_m
A	16.015	0.80	3	1660.8	0.89	1.7344
B	23.128	1.2	4	1675.9	1.0	5.3664
C	23.258	1.2	4	1676.1	1.0	1.3776
D	61.154	3.1	2	1669.3	5.2	7.6253
E	61.160	3.1	2	1669.4	5.2	2.9983
F	61.216	3.1	2	1670.4	5.2	1.0805
G	61.231	3.1	2	1670.6	5.2	1.3914
H	61.676	3.1	2	1678.4	5.2	2.5652
I	61.705	3.1	2	1679.0	5.2	3.3382
J	61.759	3.1	2	1679.9	5.2	2.6389
K	66.150	3.3	3	1662.7	3.7	1.1813
L	66.784	3.3	3	1669.7	3.7	2.0182
M	66.888	3.3	3	1670.9	3.7	14.0449
N	66.912	3.3	3	1671.2	3.7	2.4578
O	67.567	3.4	3	1678.9	3.8	0.8203
P	67.616	3.4	3	1679.5	3.8	2.1297
Q	72.971	3.6	4	1674.8	3.0	1.7454
R	105.112	5.3	1	1655.6	18	1.4159
S	115.812	5.8	3	1659.3	6.4	1.0308
T	155.756	7.8	1	1678.4	26	4.4221
U	155.765	7.8	1	1678.7	26	3.2889
V	155.768	7.8	1	1678.8	26	4.6354
W	155.770	7.8	1	1678.9	26	3.9399
X	155.780	7.8	1	1679.2	26	1.3523

Table 6.5: All unstable mechanical mode frequencies of O4 over the the chosen range. $\Delta\nu_{\text{max}}$ is the maximum possible frequency deviation due to uncertainties. R is the radius of curvature at which the mechanical mode rings. R_m is the maximum parametric gain all over the range. The optical order is the order of the main optical contributor to that OPI, that is to say at that radius of curvature (or cavity Gouy phase). ΔR_{max} is the maximum possible radius-of-curvature deviation due to mechanical frequency uncertainties (it takes account of the optical mode order). The dark blueish green rows point the mechanical modes that could be unstable even at the measure working point of 1667 m. H, I, J, O, P, and Q could be in the vicinity of this working point (in light blueish green); therefore, they might raise an OPI in case of working point tuning.

for the carrier, will trap more HOMs within the interferometer; an HOM living longer means a mode with less losses; less losses induce a smaller linewidth; then resonances are much sharper and their maximum gains are much higher. A double-recycled interferometer presents higher instabilities but that can be crossed over more easily by slightly modifying the radii of curvature of the EMs. After simulating, this is what we indeed notice. We can give the conclusion that approximately 15 mechanical modes can be unstable in O4. We obtain all necessary information upon these unstable modes, such as their frequencies, radius of curvature at which it rings, their parametric gains (which can help know what is the minimum power at which the mode becomes unstable), and the order of the main optical contributors.

Conclusion

The OPI has now been observed at both Virgo and LIGO. Its study in AdV is of crucial importance for at least two reasons: first, it is a power-proportional phenomenon and the power will continue being increased in the next commissioning phases; second, given the characteristic detection time of gravitational wave events lasts, at most, a few tens of seconds and the rather low frequency of these events, one must try not to encounter any instability, lest one looses the apparatus control.

Within the Virgo Collaboration, a dozen of people work on three aspects of the OPI: the OPI computation, the OPI mitigation, and the precursors[3]. We have seen that this thesis treats of the OPI computation, requiring first the computation of the arm cavity mirrors' mechanical modes and that of the arm cavities' optical modes.

Regarding the optical modes, I studied two different bases: one considering the finite size of the mirrors (FSMM), and the HGM. The former demands to solve an eigenvalue problem but directly provides us with the diffraction losses of the optical modes, while they need to be estimated for the HGM. We showed that optical modes are significantly distinct from order 5. In all simulations of chapter 6, we can see that some OPI ring with order-4 optical modes. Then, we consider that we should use the FSMM for the OPI computation. Especially given that we also showed that a higher-diffraction-loss optical mode, that is a higher-order mode, can be more likely to cause an OPI due to its larger linewidth.

Another advantage of the FSMM is that they can be obtained with any custom mirror shape, namely including thermal effect or considering the real maps of the mirrors rather than perfectly spherical ones. A team of the Laboratoire des Matériaux Avancés (LMA), Lyon, France, mapped the AdV's mirrors. I tried to use these maps, but the results were not satisfying; this work is still to be done.

We[4] computed the mechanical modes via a FEA simulation that provided us with the mechanical Q factors. A series of measurements on site allowed us to estimate a limit for the mechanical frequency uncertainties, of which certain happen to be higher than the optical resonance linewidths. We showed to what extent a mechanical frequency uncertainty can be transposed into a working point uncertainty. Hence, we present data taking into account various radii of curvature of both end mirrors.

Having the optical modes and the mechanical modes enables to calculate the optical gains, which set the optical resonances, and the parametric gain of each mechanical mode thanks to an object-oriented program that we have implemented. It is a remarkable tool given its flexibility, but the process of computing the overlap parameters and the parametric gain between each couple of optical and mechanical mode can take a non-negligible CPU time. And this process is all the longer if we include various working points. That is why, the code is being updated to make it lighter and faster. Also, an interesting technique that we have not used so far is, first, to determine the optical resonant frequencies up to a certain order, for example 5 or 6, and then to select, beforehand, the mechanical modes whose parametric gains need calculating according to their frequencies. This technique would drastically decrease the number of mechanical modes to include in the OPI computation.

Our first preliminary results arrived after O3 started. We performed a simulation using that configuration regardless, for we, thus, could verify whether the results matched the observation; or

---

[3] Study of the state of some interferometer variables to try to predict an OPI before it arises.

[4] Here 'we' stands for the group, tough I did not participate to this part.

I should say, the non-observation. Indeed, the first experimental observation of an OPI at Virgo happened during O3b. We profited from this observation to perform more accurate simulations that helped endorse the OPI nature of the observation on the one hand, and that gave even more credit to our simulations for the future on the other hand.

This assurance permitted me to perform a set of simulations for AdV's O4 configuration. This configuration adds an extra optical cavity (SRC) and is foreseen to start in 2022. Therefore, we can try to make our simulations as predictive as possible. That is why, I try to compute the mechanical parametric gains over a larger range of working points. The simulations shows that this extra cavity should not noticeably change the potential unstable mechanical modes from an O3 configuration. It also shows, as expected, that the optical resonances are much thinner because losses are lower, and, thus, the peaks of the resonances are higher, which, in turn, make the parametric gains of already resonant modes higher. In definitive, during O4, AdV is likely to face an OPI whose gain would be higher (increasing the speed of the instability), but it would be easier to mitigate by slightly modifying the radius of curvature of an EM. As a very near future work, a simulation with an even larger range and including the thermal effect could be an interesting improvement.

The main improvement of Observing Run 5 (O5) will be the modification of the IMs: they will get heavier and larger. The size and the mass of the mirror directly impact its natural modes. Therefore, a new series of FEA simulations is needed; it is ongoing. As well, the optical modes will be modified; we have not yet started the computation of these new optical modes. From a parametric gain prospective, the heavier the mirror, the lower the gain. However, we cannot state anything before computing at least all the modes. Indeed, the mechanical mode density can increase, so can the optical mode one. Simulations need performing, also including the thermal effect because the input power will be again increased.

Index & List of Acronyms

Bibliography

[1] O. Heaviside. A gravitational and electromagnetic analogy. *The Electrician*, 31(18):5125–5134, 1893. 9

[2] H. Poincaré. Notes de Sur la dynamique de l'électron. *Comptes rendus hebdomadaires des séances de l'Académie des sciences*, 150:1504–1508, 1906. 9

[3] A. Einstein. Die Grundlage der Allgemeinen Relativitätstheorie. *Annalen der Physik*, 354(7):769–822, 1916. 9

[4] B. P. Abbott et al. (LIGO Scientific Collaboration and Virgo Collaboration). GW150914: First results from the search for binary black hole coalescence with Advanced LIGO. *Physical Review D*, 93(12):122003, 2016. 9

[5] R. A. Hulse and J. H. Taylor. Discovery of a pulsar in a binary system. *The Astrophysical Journal*, 195:L51–L53, 1975. 9

[6] B. P. Abbott et al. (LIGO Scientific Collaboration and Virgo Collaboration). GW151226: Observation of Gravitational Waves from a 22-Solar-Mass Binary Black Hole Coalescence. *Physical Review Letters*, 116(24):241103, 2016. 9

[7] B. P. Abbott et al. (LIGO Scientific Collaboration and Virgo Collaboration). GW170104: Observation of a 50-Solar-Mass Binary Black Hole Coalescence at Redshift 0.2. *Physical Review Letters*, 118(22):221101, 2017. 9, 30

[8] C. W. Misner, K. S. Thorne, and J. A. Wheeler. *Gravitation*. Macmillan, 1973. 9, 10

[9] R. M. Wald. *General Relativity*. The University of Chicago Press, 1984. 10

[10] E. D. Black and R. N. Gutenkunst. An introduction to signal extraction in interferometric gravitational wave detectors. *American Journal of Physics*, 71(4):365–378, 2003. 10, 20

[11] N. Arnaud. *Contrôle global de la partie centrale du détecteur d'ondes gravitationnelles Virgo. Recherche de signaux impulsionnels: application aux coincidences entre interféromètres*. PhD thesis, Université Paris Sud - Paris XI Orsay, 2002. 10, 11, 20, 23, 24

[12] M. Kasprzack. *Thermally Deformable Mirrors: a new Adaptive Optics scheme for Advanced Gravitational Wave Interferometers*. PhD thesis, Université Paris-Sud 11, 2014. 10, 11, 20, 23

[13] P. R. Saulson. *Fundamentals of Interferometric Gravitational Wave Detectors*. World Scientific, 1994. 11

[14] R. C Tolman. Static Solutions of Einstein's Field Equations for Spheres of Fluid. *Physical Review*, 55(4):364, 1939. 12

[15] J. R. Oppenheimer and G. M. Volkoff. On massive neutron cores. *Physical Review*, 55(4):374, 1939. 12

[16] I. Bombaci. The maximum mass of a neutron star. *Astronomy and Astrophysics*, 305:871, 1996. 12

[17] V. Kalogera and G. Baym. The maximum mass of a neutron star. *The Astrophysical Journal Letters*, 470(1):L61, 1996. 12

[18] S. Bonazzola and J.-A. Marck. Efficiency of gravitational radiation from axisymmetric and 3 d stellar collapse. i-polytropic case. *Astronomy and Astrophysics*, 267:623–633, 1993. 12

[19] J. Abadie et al. (The LIGO Scientific Collaboration and The Virgo Collaboration). Search for Gravitational Waves from low Mass Compact Binary Coalescence in LIGO's Sixth Science Run and Virgo's Science Runs 2 and 3. *Physical Review D*, 85(8):082002, 2012. 12

[20] A. Lartaux-Vollard. *Beating the standard quantum limit for the gravitational wave detector Advanced Virgo*. PhD thesis, Université Paris-Saclay, 2020. 12, 26

[21] C. M. Will. Henry Cavendish, Johann von Soldner, and the deflection of light. *American Journal of Physics*, 56(5):413–415, 1988. 13

[22] J. Soldner. Über die Ablenkung eines Lichtstrahls von seiner geradlinigen Bewegung durch die Attraktion eines Weltkörpers, an welchem er nahe vorbei geht. *Annalen der Physik*, 370(15):593–604, 1921. 13

[23] F. W. Dyson, A. S. Eddington, and C. Davidson. IX. A determination of the deflection of light by the Sun's gravitational field, from observations made at the total eclipse of May 29, 1919. *Philosophical Transactions of the Royal Society of London. Series A, Containing Papers of a Mathematical or Physical Character*, 220(571-581):291–333, 1920. 13

[24] W. S. Adams. The relativity displacement of the spectral lines in the companion of Sirius. *Proceedings of the National Academy of Sciences of the United States of America*, 11(7):382, 1925. 13

[25] D. M. Popper. Red Shift in the Spectrum of 40 Eridani B. *The Astrophysical Journal*, 120:316, 1954. 13

[26] J. Weber. Detection and Generation of Gravitational Waves. *Physical Review*, 117(1):306, 1960. 15

[27] A. Abramovici, W. E. Althouse, R. W. P. Drever, Y. Gürsel, S. Kawamura, F. J. Raab, D. Shoemaker, L. Sievers, R. E. Spero, K. S. Thorne, et al. LIGO: The Laser Interferometer Gravitational-Wave Observatory. *Science*, 256(5055):325, 1992. 15

[28] J. L. Levine. Early Gravity-Wave Detection Experiments, 1960-1975. *Physics in Perspective*, 6(1):42–75, 2004. 15

[29] V. Fafone. Resonant-mass detectors: status and perspectives. *Classical and Quantum Gravity*, 21(5):S377, 2004. 15

[30] A. De Waard, L. Gottardi, M. Bassan, E. Coccia, V. Fafone, J. Flokstra, A. Karbalai-Sadegh, Y. Minenkov, A. Moleti, G. V. Pallottino, et al. Cooling down MiniGRAIL to milli-Kelvin temperatures. *Classical and Quantum Gravity*, 21(5):S465, 2004. 15

[31] M. E. Gerstenshteĭn and V. I. Pustovoĭt. On the detection of low frequency gravitational waves. *Journal of Experimental and Theoretical Physics*, 16(2):433–435, 1963. 15

[32] R. Weiss, D. J. Muehlner, R. L. Benford, D. K. Owens, N. A. Pierre, and M. Rosenbluh. Gravitation research. Technical report, 1972. 15

[33] B. Bryson. *A short history of nearly everything*. 2003. 16

[34] G. Vajente. Interferometer configurations. VESF School on Advanced Gravitationnal Wave Detectors 2012, 2012. 17, 20, 24

[35] `http://public.virgo-gw.eu/the-virgo-collaboration`, `https://apps.virgo-gw.eu/vmd/public/institutions`. 18

[36] The Virgo Collaboration. Advanced Virgo Technical Design Report. VIR-O128A-12, 2012. `https://tds.virgo-gw.eu/ql/?c=8940`. 20, 22, 27, 28, 57, 80

[37] R. Bonnand. *The Advanced Virgo Gravitational Wave Detector: Study of the optical design and development of the mirrors*. PhD thesis, Université de Lyon, 2012. 23

[38] J. Casanueva Diaz. *Control of the Gravitational Wave Interferometric Detector Advanced Virgo*. PhD thesis, Université Paris Saclay, 2017. 23, 28

[39] G. Vajente. *Analysis of sensitivity and noise sources for the Virgo gravitational wave interferometer*. PhD thesis, Scuola Normale Superiore di Pisa, 2008. 24

[40] F. Acernese et al. ((Virgo Collaboration), H. Vahlbruch, M. Mehmet, H. Lück, and K.) Danzmann. Increasing the Astrophysical Reach of the Advanced Virgo Detector via the Application of Squeezed Vacuum States of Light. *Physical Review Letters*, 123(23):231108, 2019. 26

[41] M. Bawaj, M. Barsuglia, M. Bazzan, E. Calloni, G. Ciani, L. Conti, B. D'Angelo, M. De Laurentis, R. De Rosa, S. Di Pace, et al. Study and experiment on the alternative technique of frequency–dependent squeezing generation with EPR entanglement for Virgo. 1468(1):012215, 2020. 26

[42] LIGO Scientific Collaboration B. P. Abbott et al. (KAGRA Collaboration and Virgo Collaboration). Prospects for observing and localizing gravitational-wave transients with Advanced LIGO, Advanced Virgo and KAGRA. *Living Reviews in Relativity*, 21(1):3, 2018. 29

[43] B. P. Abbott et al. (LIGO Scientific Collaboration and Virgo Collaboration). Observation of Gravitational Waves from a Binary Black Hole Merger. *Physical Review Letters*, 116(6):061102, 2016. 29

[44] B. P. Abbott et al. (LIGO Scientific Collaboration and Virgo Collaboration). GW170814: A Three-Detector Observation of Gravitational Waves from a Binary Black Hole Coalescence. *Physical Review Letters*, 119(14):141101, 2017. 30

[45] B. P. Abbott et al. (LIGO Scientific Collaboration and Virgo Collaboration). GW170817: Observation of Gravitational Waves from a Binary Neutron Star Inspiral. *Physical Review Letters*, 119(16):161101, 2017. 30

[46] B. P. Abbott et al. (LIGO Scientific Collaboration and Virgo Collaboration). GWTC-1: A Gravitational-Wave Transient Catalog of Compact Binary Mergers Observed by LIGO and Virgo During the First and Second Observing Runs. *Physical Review X*, 9(3):031040, 2019. 30

[47] R. Abbott et al. (The LIGO Scientific Collaboration and the Virgo Collaboration). GWTC-2: Compact Binary Coalescences Observed by LIGO and Virgo During the First Half of the Third Observing Run. *arXiv preprint arXiv:2010.14527*, 2020. 30

[48] R. Abbott et al. (LIGO Scientific Collaboration and Virgo Collaboration). GW190412: Observation of a binary-black-hole coalescence with asymmetric masses. *Physical Review D*, 102(4):043015, 2020. 30

[49] B. P. Abbott et al. GW190425: Observation of a Compact Binary Coalescence with Total Mass 3.4 Msun. *The Astrophysical Journal Letters*, 892(1):L3, 2020. 30

[50] R. Abbott et al. (LIGO Scientific Collaboration and Virgo Collaboration). GW190521: A Binary Black Hole Merger with a Total Mass of 150 Msun. *Physical Review Letters*, 125(10):101102, 2020. 30

[51] B. P. Abbott et al. (LIGO Scientific Collaboration and Virgo Collaboration). Astrophysical implications of the binary black hole merger GW150914. *The Astrophysical Journal Letters*, 818(2):L22, 2016. 30

[52] B. P. Abbott et al. (The LIGO Scientific Collaboration and the Virgo Collaboration). Binary black hole population properties inferred from the first and second observing runs of advanced LIGO and advanced Virgo. *The Astrophysical Journal Letters*, 882(2):L24, 2019. 30

[53] LIGO Scientific Collaboration, Virgo Collaboration, 1M2H Collaboration, Dark Energy Camera GW-EM Collaboration, DES Collaboration, DLT40 Collaboration, Las Cumbres Observatory Collaboration, VINROUGE Collaboration, MASTER Collaboration, et al. A gravitational-wave standard siren measurement of the hubble constant. *Nature*, 551(7678):85–88, 2017. 30

[54] V. B. Braginsky, S. E. Strigin, and S. P. Vyatchanin. Parametric oscillatory instability in Fabry–Perot interferometer. *Physics Letters A*, 287(5-6):331–338, 2001. 33, 34, 36

[55] M. Evans, L. Barsotti, and P. Fritschel. A general approach to optomechanical parametric instabilities. *Physics Letters A*, 374(4):665–671, 2010. 33, 36, 37, 61, 75, 76, 77

[56] M. Evans, S. Gras, P. Fritschel, J. Miller, L. Barsotti, D. Martynov, A. Brooks, D. Coyne, R. Abbott, R. X. Adhikari, et al. Observation of parametric instability in Advanced LIGO. *Physical Review Letters*, 114(16):161102, 2015. 33, 34, 36, 75

[57] L. Brillouin. Diffusion de la lumière et des rayons x par un corps transparent homogène. *AnPh*, 9(17):88–122, 1922. 33

[58] L. I. Mandelstam. Light scattering by inhomogeneous media. *Zhurnal Russkogo fiziko-khimicheskogo obshchestva*, 58:381, 1926. 33

[59] S. P. Vyatchanin and S. E. Strigin. Parametric oscillatory instability in gravitational wave laser detectors. *Physics-Uspekhi*, 55(11):1115, 2012. 34, 35

[60] W. Kells and E. D'Ambrosio. Considerations on parametric instability in Fabry–Perot interferometer. *Physics Letters A*, 299(4):326–330, 2002. 34

[61] V. B. Braginsky, S. E. Strigin, and S. P. Vyatchanin. Analysis of parametric oscillatory instability in power recycled LIGO interferometer. *Physics Letters A*, 305(3-4):111–124, 2002. 34, 36

[62] A. Allocca, G. Bogaert, D. E. Cohen, T. Jacqmin, and P. Puppo. personal communication. 36, 67, 80, 84

[63] C. Zhao, L. Ju, J. Degallaix, S. Gras, and D. G. Blair. Parametric Instabilities and Their Control in Advanced Interferometer Gravitational-Wave Detectors. *Physical Review Letters*, 94(12):121102, 2005. 37

[64] L. Ju, C. Zhao, S. Gras, J. Degallaix, D. G. Blair, J. Munch, and D. H. Reitze. Comparison of parametric instabilities for different test mass materials in advanced gravitational wave interferometers. *Physics Letters A*, 355(6):419–426, 2006. 37

[65] L. Ju, D. G. Blair, C. Zhao, S. Gras, Z. Zhang, P. Barriga, H. Miao, Y. Fan, and L. Merrill. Strategies for the control of parametric instability in advanced gravitational wave detectors. *Classical and Quantum Gravity*, 26(1):015002, 2008. 37

[66] F. Liang, C. Zhao, S. Gras, L. Ju, and D. G. Blair. Study of three-mode parametric instability. 228(1):012025, 2010. 37

[67] C. Zhao, L. Ju, Q. Fang, C. Blair, J. Qin, D. Blair, J. Degallaix, and H. Yamamoto. Parametric Instability in Long Optical Cavities and Suppression by Dynamic Transverse Mode Frequency Modulation. *Physical Review D*, 91(9):092001, 2015. 37

[68] Y. B. Ma, J. Liu, Y. Q. Ma, C. Zhao, L. Ju, D. G. Blair, and Z. H. Zhu. Thermal modulation for suppression of parametric instability in advanced gravitational wave detectors. *Classical and Quantum Gravity*, 34(13):135001, 2017. 37

[69] H. S. Bantilan and W. P. Kells. Investigating a Parametric Instability in the LIGO Test Masses. *LIGO Document: LIGO-T060207-00-Z*, 2006. 37

[70] A. V. Cumming, A. S. Bell, L. Barsotti, M. A. Barton, G. Cagnoli, D. Cook, L. Cunningham, M. Evans, G. D. Hammond, G. M. Harry, et al. Design and development of the advanced LIGO monolithic fused silica suspension. *Classical and Quantum Gravity*, 29(3):035003, 2012. 37

[71] T. Corbitt, Y. Chen, and N. Mavalvala. Mathematical framework for simulation of quantum fields in complex interferometers using the two-photon formalism. *Physical Review A*, 72(1):013818, 2005. 38

[72] C. M. Caves and B. L. Schumaker. New formalism for two-photon quantum optics. I. Quadrature phases and squeezed states. *Physical Review A*, 31(5):3068, 1985. 38

[73] B. L. Schumaker and C. M. Caves. New formalism for two-photon quantum optics. II. Mathematical foundation and compact notation. *Physical Review A*, 31(5):3093, 1985. 38

[74] M. Granata, A. Amato, L. Balzarini, M. Canepa, J. Degallaix, D. Forest, V. Dolique, L. Mereni, C. Michel, L. Pinard, B. Sassolas, J. Teillon, and G. Cagnoli. Amorphous optical coatings of present gravitational-wave interferometers. *Classical and Quantum Gravity*, 37(9):095004, 2020. 46, 47

[75] L. Cunningham, P. G. Murray, A. Cumming, E. J. Elliffe, G. D. Hammond, K. Haughian, J. Hough, M. Hendry, R. Jones, I. W. Martin, S. Reid, S. Rowan, J. Scott, K. A. Strain, K. Tokmakov, C. Torrie, and A. A. van Veggel. Re-evaluation of the mechanical loss factor of hydroxide-catalysis bonds and its significance for the next generation of gravitational wave detectors. *Physics Letters A*, 374(39):3993–3998, 2010. 47

[76] A. Allocca and A. Chiummo. Logbook entry at `https://logbook.virgo-gw.eu/virgo/?r=42806`. 55

[77] B. E. A. Saleh and M. C. Teich. *Fundamentals of Photonics*. John Wiley & Sons, 2007. 55, 57, 59, 63

[78] H. Kogelnik and T. Li. Laser Beams and Resonators. *Applied Optics*, 5(10):1550–1567, 1966. 58, 59, 64

[79] K. F. Renk. *Basics of Laser Physics*. Springer, 2012. 58

[80] W. Streifer. Optical Resonator Modes—Rectangular Reflectors of Spherical Curvature. *Journal of the Optical Society of America*, 55(7):868–875, 1965. 64

[81] The Mathworks, Inc., Natick, Massachusetts. *MATLAB® version 9.8.0.1323502 (R2020a)*, 2020. 65

[82] MathWorks. *MATLAB®: Function Reference*, volume 1, pages 3279–3295. `https://fr.mathworks.com/help/pdf_doc/matlab/matlab_ref.pdf`. 65

[83] D. E. Cohen, A. Allocca, G. Bogaert, P. Puppo, and T. Jacqmin. Optomechanical parametric instabilities simulation in advanced virgo. *arXiv preprint arXiv:2102.11070*, 2021. 67, 82

[84] L. Pinard. Advanced Virgo Input Mirror Characterization report- IM02 (coatings C14081+C14087). *Virgo Internal Note*, VIR-0543A-14, 2014. https://tds.virgo-gw.eu/ql/?c=10649. 67

[85] L. Pinard. Advanced Virgo Input Mirror Characterization report- IM04 (coatings C14081+C14087). *Virgo Internal Note*, VIR-0544A-14, 2014. https://tds.virgo-gw.eu/ql/?c=10650. 67

[86] L. Pinard. Advanced Virgo End mirror Characterization report- EM01 (coatings C14042/10 + C14035/10). *Virgo Internal Note*, VIR-0269A-15. https://tds.virgo-gw.eu/ql/?c=10990. 67

[87] L. Pinard. Advanced Virgo End mirror Characterization report- EM03 (coatings C14042/20 + C14035/20). *Virgo Internal Note*, VIR-0270A-15, 2015. https://tds.virgo-gw.eu/ql/?c=10991. 67

[88] The Virgo Collaboration. The Virgo Physics Book, vol. II, optics and related topics, 2005. 70

[89] D. D. Brown and A. Freise. Finesse, may 2014. The software and source code is available at http://www.gwoptics.org/finesse. 73

[90] A. C. Green, D. D. Brown, M. Dovale-Álvarez, C. Collins, H. Miao, C. M. Mow-Lowry, and A. Freise. The influence of dual-recycling on parametric instabilities at Advanced LIGO. *Classical and Quantum Gravity*, 34(20):205004, 2017. 73

[91] J. Degallaix, C. Zhao, L. Ju, and D. Blair. Thermal tuning of optical cavities for parametric instability control. *Journal of the Optical Society of America B*, 24(6):1336–1343, 2007. 80

[92] A. Allocca. ITF (Parametric?) Instability. *Virgo Internal Note*, VIR-0018A-20, 2020. https://tds.virgo-gw.eu/ql/?c=15132. 84

[93] A. Allocca and P. Puppo. Observation of Parametric Instability in Virgo. *Virgo Internal Note*, VIR-0287A-20, 2020. https://tds.virgo-gw.eu/ql/?c=15408. 84

[94] A. G. Gurkovsky, S. E. Strigin, and S. P. Vyatchanin. Analysis of parametric oscillatory instability in signal recycled LIGO interferometer. *Physics Letters A*, 362(2-3):91–99, 2007. 87

Remerciements / Acknowledgements

Voilà arrivé à la fin, quasiment quatre années se sont écoulées. Avant de remercier dignement toutes les personnes qui m'ont soit permis d'arriver jusqu'ici, ou qui ont simplement rendu ma vie plus belle, je veux changer ici les codes habituels.

Je veux remercier du fond du cœur ma maman qui, paix à son âme, s'est battue contre le cancer pendant les trois années de mon doctorat, mais qui n'a pas pu voir l'aboutissement de ce travail. On se soutenait mutuellement, et on croyait tous les deux à nos réussites respectives. Tu as toujours été une maman formidable, autant pour l'éducation de tes enfants, que dans ta vie personnelle. Je suis fier que t'avoir vue si forte face à ces difficultés, et que tu aies cru en la vie jusqu'au bout. Je ne serais clairement pas où je suis, et, surtout, qui je suis sans toi. Merci pour tout !

À côté de cette épreuve qui a rendu ces dernières années très difficiles pour moi, la vie, comme toujours, a également montré ses plus beaux atours. Et après la mémoire d'évènements tristes, il est bon de se rappeler les moments joyeux.

Tout d'abord, je tenais à exprimer à quel point je suis reconnaissant que mon parcours académique et professionnel m'ait permis de rencontrer Nicolas Arnaud, mon directeur de thèse. En effet, dès notre premier entretien téléphonique, pour un stage de M2, j'ai senti que tu serais une personne très intéressante. Et la suite n'a fait que le confirmer. Tu as toujours su être présent ou distant comme il le fallait, autant d'un point de vue professionnel que personnel. Et bien qu'on ne travaillait pas sur le même projet, tu m'as remis *on track* lorsqu'il le fallait. Merci de m'avoir fait confiance et de m'avoir soutenu !

À partir du moment où mon intégration au groupe PI a été entérinée, j'ai commencé à travailler en étroite collaboration avec Thibaut Jacqmin, qui, très rapidement, a accepté de jouer le rôle d'un encadrant alors que cette tâche ne lui était pas du tout initialement incombée ; et c'est pour cela qu'il m'a paru judicieux de lui proposer de devenir officiellement mon coencadrant de thèse. Donc, je tiens tout particulièrement à te remercier pour ton aide scientifique, et également pour ton soutien moral. Je regrette sincèrement que la situation sanitaire ait empêché à chaque fois que l'on puisse travailler réellement ensemble, et pas seulement par email ou visioconférence. Mais ce fut tout de même un réel plaisir de collaborer avec toi.

Et petit message commun à tous les deux, je vous remercie pour votre franchise, autant pour « me remonter les bretelles » que pour me féliciter.

Trouver une personne qui accepte de devenir son directeur de thèse est une première étape très importante pour commencer un doctorat, mais, également, le laboratoire en question doit être d'accord : je remercie Achille Stocchi pour m'avoir accepté au sein de son établissement, le Laboratoire de l'Accélérateur Linéaire (LAL) lorsque j'ai commencé, puis qui est devenu l'Institut de Physique des 2 Infinis Irène Joliot-Curie (IJCLab) suite à la fusion de plusieurs laboratoires.

Mais que serait un doctorat sans École doctorale ? ! Et c'est pour cela que j'aimerais exprimer toute ma gratitude à Patrice Hello, directeur de PHENIICS, qui non seulement a accepté chaque année que mon travail se poursuive, mais aussi m'a souvent donné de très bons conseils en ce qui concerne le déroulement de la thèse. Merci Patrice ! et aussi pour avoir toujours répondu à mes innombrables questions lorsque je me perdais si souvent dans les démarches administratives.

I would like to express my heartfelt gratitude to all the members of the jury. I will now switch into each member's own native language.

Je tiens à remercier Frédérique Marion qui a accepté de faire partie des rapporteurs, et donc d'avoir pris le temps de lire ma thèse, d'approuver la validité de la soutenance, et pour ses commentaires.

Poi vorrei ringraziare Ettore Majorana per aver letto la mia tesi e per le suoi commentari che l'hanno migliorata. Pure, sono molto grato in generale per la tua disponibilità, le tue risposte, e il tuo supporto.

J'aimerais exprimer une toute particulière attention à Sophie Kazamias, qui, pour cette thèse, a accepté avec plaisir d'être examinatrice de ma soutenance, mais qui m'a surtout permis d'accéder à cet aboutissement en acceptant ma candidature en formation continue au sein de son M2 Grands Instruments il y a cinq ans, et qui a eu confiance en ma motivation. Je suis vraiment reconnaissant d'avoir eu la chance de participer à votre formation très enrichissante tenue par une personne si dynamique et déterminée dans son travail.

Je remercie très chaleureusement Jérôme Degallaix, pour avoir accepté d'être examinateur de mon jury. Mais également pour tous les échanges qu'on a pu avoir, que ce soit au sujet des OPI ou des lock losses. J'ai particulièrement apprécié ta disponibilité, ta gentillesse, et ta rigueur scientifique.

Et je souhaite exprimer un très grand merci à Sophie Henrot-Versillé pour avoir accepté le poste de présidente du jury, et qui a su parfaitement introduire et animer la soutenance.

Il reste un dernier élément important pour le bon déroulement de soutenance (d'autant plus quand elle se doit d'être principalement en visioconférence) : le garant technique. Et je tiens à remercier Nicolas Leroy pour s'être plus que bien occupé de cette tâche. Mais, en fait, pour tellement d'autres choses aussi. Merci Nicolas pour ta disponibilité sans faille, d'avoir été une aide et lien direct avec une grande partie des démarches administratives sur place à Orsay (pas toujours facile quand on est quasiment tout le temps à plus de 1000 km), tes conseils scientifiques et professionnels, et tes encouragements et ton soutien.

Ringrazio molto sinceramente Paola Puppo, responsabile del gruppo PI con cui ho lavorato. Sei sempre stata ascoltando e disponibile quando avevo bisogno. Penso che tu sia una persona molto umana e gentile, ed è stato davvero un piacere lavorare con te.

As well, it was a great pleasure to work with Annalisa Allocca and Gilles Bogaert. Both of you were always keen to help me whenever I felt the need. I truly appreciated the conversations and chats that we shared.

I would also like to thank all the other members of the PI group for our fruitful conversations: Margherita Turconi, Nelson Christensen (thank you also for your encouragement and support for my talk at Les Rencontres de Moriond, and for the organisation of the summer school at École de Physique des Houches), Walid Chaibi, Thomas Harder, Marco Romanelli, and François Bondu.

Che sarebbe stata la vita a Pisa senza il buon umore e la cordialità sul sito di EGO? Mi è piaciuto come all'inizio l'atmosfera può sembrare un poco timida (almeno non c'è ipocrisia) pero, in realtà, tutti sono pronti ad aiutarti con la loro area di competenza speciale, e con molto piacere. Alla fine si può imparare tante cose sulla fisica di Virgo. Vi ringrazio voi tutti.

Un grazie speciale per Maddalena Mantovani, Diego Bersanetti, John Brooks, Paolo Ruggi, Antonino Chiumo, Andrea Magazzu, Irene Fiori, Valerio Boschi, Heinrich Heitmann, Gary Hemming, e Bas Swinkels per la loro aiuta e le loro risposte dettagliate alle mie domande. Pure, tra di loro sono alcuni che spesso mi hanno portato da Pisa al sito di EGO, vi ringrazio molto per quello. Ovviamente un pensiero particolare per tutti che giocano a ping pong. Non dimenticherò mai tutti questi « - Io gioco! - Sotto il tavolo! Sotto il tavolo! etc. ». Une attention particulière pour Julia Casanueva-Diaz (muchas gracias por tu ayuda en EGO desde el principio), Camilla De

Rosi, Matthieu Gosselin, et Gabriel Pillant, pour ce que j'ai déjà énoncé ici, et, également, pour les moments passés ensembles et leur soutien.

I cannot forget all Virgo members who spent some time on site, and with whom we also shared interesting scientific talks, car rides, and amazing ping pong matches! A particular thank to Francesco Di Renzo, Imran Khan, Mattia Boldrini, Neha Singh, Valeria Sequino, Alex Amato.

Je voudrais également exprimer ma gratitude à toute l'équipe Virgo-LAL, devenue Virgo-IJCLab, avec qui je n'ai eu que des contacts et relations sporadiques à cause de ma localisation à Pise, mais avec qui j'ai apprécié passer les rares moments où je devais être à Paris/Orsay, autant pour les discussions scientifiques que pour les plus relâchées : Florent Robinet, Valentin Frey, Pierre Gruning, Angelique Lartaux-Vollard et Misha Belahcene (Les Houches était un grand moment ! Et bravo Misha pour l'escalade !), Sarah Antier, Fabien Cavalier, Marie-Anne Bizouard (super cool organisation de la summer school des Houches !), David Corre (« Mec, ils servent du Genepi au bar ! » ; et la petite balade dans la neige), Jean-Grégoire Ducoin (« - Eh, ça te dit on va au village ? bien qu'il pleuve comme vache bretonne qui pisse. - Ça part ! ! ! » Courage pour la dernière ligne droite !), et Pierre-Alexandre Duverne. Et ceux qui sont arrivés plus tard et avec qui j'ai eu, malheureusement, peu voire pas d'échange, Marion Pillas et Shaymaa Hussein (bon courage à toutes les deux pour votre PhD !), Tito Dal Canton (loving linguistics at least as much as physics, I really appreciated when you pointed out the relation between Dal Canton and Ducoin ;)), et Aymeric van de Walle (merci pour tes conseils et encouragements lors de notre première rencontre).

Un grand merci à Manon Paris, Sylvie Prandt, Sylvie Teulet, et Isabelle Vauléon pour leur aide plus que précieuse pour les démarches et problèmes administratifs. D'autant plus que je n'étais probablement pas toujours le cas le plus facile : « Alors, je pars en avion de Pise pour aller à Paris le 15, puis le 18 je prends un train pour Saint-Perdu-l'Église-en-Bauce-sur-Mer, mais le 34, je rentrerai de Strasbourg à Pise avec ma voiture, par nationales, ... », « Il faut que je vienne signer un contrat ? ! Mais là je suis à Pise... ».

Had I to point out a single small negative aspect of my PhD, I would say the lack of proper PhD student life. Indeed, I was far away from my university, and not in a university lab (there are few PhD students always on site at EGO). That's why I fancied so much participating to scientific events that would make me get together with other PhD students (and scientists), like the Summer School at École de Physique des Houches (Lectures, Beers, Hiking/Climbing, Repeat), Les Rencontres de Moriond, and the JRJC (ou la semaine du karaoké ? et celle où je ne me retrouve pas le seul fumeur du tout...! enfin). I thank all of those I had a lot of fun and interesting conversations with. If you happen to read this thesis, then you'll recognise yourself. But I'd like to give a special thank to Francesco Cabral, for we met again later, at his, in Sintra, Portugal, and for the extremely deep talks, muito obrigado; to Nicolas Radulesco, also because we met again later, for his interesting vision of life, and the love we share with mountains (j'espère pouvoir faire une randonée avec toi).

Je tenais également à remercier tout le staff de l'École de Physique des Houches, avec qui on a passé de très bons moments et délires, et dont j'ai revu certains en repartant des Rencontres de Moriond : Kevin, Julien, Grégoriié, et désolé pour ceux dont je ne me rappelle pas les noms.

Mmhh life in Pisa... how many times can we hear 'Pisa merdaaa!' from all of those students?! But how come could Pisa be so shitty if like so many students from Italy and Europe come over there? OK, it definitely misses concert halls... and proper clubs where we can stamp our feet from 120 to more than 200 bpm all the night long... But there's an emulating street life where you can always meet someone you know. Speaking of you guys... you've been just awesome! I'd like to thank all the people from various 'generations' that followed each other at *La Colmena*, the best house ever, as well as those who were part of this nice community: Piero (among so many altre cose, grazie bello per tu hospitalidad en Barcelona!), Irene, Vanessa (ahhh these three days of peace of mind and techno at *Klangtherapie*!), Amaro, Mati (longest Colmena flatmate!), Davor, Jorge (so cool to see you every now and then!), Kevin, Tamsin, Julia, Leo (so many tough, deep, animated conversations... pronto podremos hacerlas en castillano, estoy mejorando), Ankith (come back to Europe!! ;) we miss you! I'll come to see you in India bro), Chethan and Ivette (it was so cool to see you in Barcelona and Paris too! where should we meet next?), Christophe, Maxime, Nikos, Ovidiu ('Ovidiu! Do you wanna watch a video?'), Fabian (the visit of Rome wouldn't've been so interesting without you!), Joseph, Juliette, Katherine, Elisa, Laura, Alexander (I'll miss these parties in Mannheim), and Pauline (thanks for your hospitality in Amsterdam, plus I'd always dreamt to live a bit in these so typical Dutch city houses, and for joining me at the *7 Chakras festival*!). And thanks all of you a lot for all our trips in countryside! (« And if we rented a 9-passenger car? »)

And what would've been my Pisa life without the craziness and party-lover spirit of hyper dynamic Israeli people?! I mean, whenever I say 'Let's go the the beach!... to mountains!... to snow!... to this or that village!... to some sulphuric hot springs!... or even let's drive more than three hours to get to a party or a festival and arrive in the middle of the night... or anything... you'll be dedicated to do so. (non-Latin scripts force me to break this line)
Василий (aka Elevatus Vacuus Castagna the Psychonaut, my beloved братан flatmate! Beemet, che lingua do we speak latekh? and che magical colourful autumnal hiking to Monte Forato...!), אלי , רון (so many amazing sunsets!), אורי . Thank you for everything, from your psychological support to all these crazy and lovely moments. תודה רבה

I'd like to add a special mention to Toby, who was an intern at EGO, and who also always fancied joining any plan for visiting all around, and with whom I had the chance to hike bear-foot up to the Gran Sasso and see one of the southernmost European glaciers. As well, thank you very much for our exceptionally interesting conversations on linguistics! And another special mention to Marta, my Berlinerin activist friend, met while hiking in the Cinque Terre with Toby (thanks man for your success in dedicating me while I knew how crowded that place usually is). Danke schön for your hospitality in Berlin, for our extremely enriching talks on society, you helped me open my mind on some interesting social aspects.

I'd like to thank Nina, for your psychological support and your kindness.

Thank you Dinesh for your support when things started going wrong in my life. I hope we'll get together again very soon.

Thank you Ákos for meeting in Copenhagen. And thank you Harish you hosting us at yours in Århus, I was really glad to attend your PhD defence.

Thanks to all teachers who fed my thirst for knowledge in any field, and provided me with the keys to reach this achievement. And a special thank to Richard Donahue, Vladimir Smakhtin, and Yan Benhammou, who supervised my internships at LBNL and at Weizmann Institute of Science, and definitely made me want to carry on with a PhD.

Here I thank anyone who's not been mentioned, and that I shared incredible moments and deep talks with.

Before thanking longtime friends and relatives, I must here thank two important people to me, as controversial as it might be perceived. First, Alexandra Elbakyan, for her prominent contribution to Science. Second, in memory of Albert Hofmann: danke schön für dein Sorgenkind, it really has helped me go beyond and overcome difficulties, and be more sensitive to the beauty of life.

Je veux maintenant remercier mes amis de longues dates, pour qui je n'aurai pas besoin de m'étendre autant car nous savons déjà tout l'amour que nous nous portons. Wesh si si la famille ! ! J'vous kiffe !

Cependant, une petite kass-dédi à Nils et Noémie, ou Noémils, pour leur mariage. Ça a été plus qu'un honneur pour moi d'être un de tes témoins Nils. Merci à tous les deux pour tout en général !

Et j'ai une pensée particulièrement émue et tendre envers... pleins de gens en fait. Alors, mes potos de la Cité des Sciences : Ludivine, Benoît, Antoine, Luca, et Antonio. Les (ex-)Caennais : Coccococococoooo, Zaki, Fred, Ararat, Boris, Bouba, Raph, Julien F, Julien M, Damien (aka La P'tite Colle), Seb, Amine, Flo(teub ?). Les cliques d'Elsaß : Mathieu (aka pleins de trucs en -el(le) et même des trucs qui, normalement, ne finissent pas en -el(le), mais du coup... si), Vincent (aka Chiss aka Papier aka Pooopiiir aka Ciseaux aka Caillou aka 120sachets aka .... chaimemepu), Gaetan C'est-Pas-Ro (mais c'est qui alors ?), Alex (B-Boy Rastalex), Alexis (Braumeister), Sophie, Steve, Valérie, Julien et Marianne (c'était vraiment trop d'la balle ce confinement dans les Vosges !). Et également ceux chez qui j'ai obtenu une médaille de sale squatteur de merde : Anna (« Eh, si on parlait encore linguistique, montagnes et déserts ? ! »), Clo, Nino, et Axel. Voilà, je vous ai tous « thêmatisés », mais en vrai, VMVC que j'kiffe surtout mélanger les cliques de potes, et c'est dans l'ensemble assez bien réussi.

Merci à vous tous pour tout ce qu'on partage et d'être toujours présent dans le besoin, même sans prise de contact forcément fréquente.

J'ai une pensée pour Agnès, la sœur de ma mère, qui nous a également quittés en cette année tragique. Paix à son âme, et courage à ses enfants, et à son frère.

Et j'aimerais finir par remercier ma famille de tout mon cœur ! Je ne citerai pas tout le monde, ma famille est gigantesque même en n'allant que jusqu'aux cousins.

Premièrement, merci à tous pour votre soutien lors de cette année 2020 toute pourrie, vous avez tous su exprimer les mots qu'il fallait, ou même être présents. Et merci à tous, pour tous les moments partagés en famille.

Je remercie tout particulièrement mon père pour tous ses enseignements, son soutien, et d'avoir fait en sorte, avec ma mère, que nous ne manquions jamais de rien ma sœur et moi. Merci beaucoup à ma sœur pour son soutien et tous ces moments marrants. Ou moins marrants... mais on est toujours là quoi !

université PARIS-SACLAY

ÉCOLE DOCTORALE
Particules, hadrons, énergie et noyau : instrumentation, imagerie, cosmos et simulation (PHENIICS)

Titre : Étude des instabilités paramétriques optomécaniques pour le détecteur Advanced Virgo

Mots clés : détecteur Advanced Virgo, instabilités paramétriques optomécaniques (OPI), modes propres de cavités optiques, résonateur optique de Fabry-Perot, cavity à miroirs sphériques

Résumé : Le 14 septembre 2015, la collaboration LIGO-Virgo fit la première détection directe d'une onde gravitationnelle, produite par la fusion de deux trous noirs. Cette détection a confirmé l'existence des trous noirs et a permis de prouver celle des ondes gravitationnelles. Cela a nécessité de détecter un signal extrêmement faible — une amplitude relative de l'ordre de 10^{-22} $Hz^{-1/2}$. Une telle prouesse a été rendue possible grâce à l'amélioration continue de la sensibilité des détecteurs pendant plus d'une décennie.

Augmenter la puissance du laser entrant dans l'interféromètre est une possibilité pour améliorer encore plus la sensibilité, parce cela diminue l'importance relative du bruit quantique du laser à haute fréquence. Cependant, des instabilités paramétriques optomécaniques limitent l'augmentation de la puissance optique.

Cette thèse présente les simulations que nous avons effectuées de ces instabilités. Nous avons calculé le gain paramétrique de chaque mode mécanique des quatre miroirs suspendus des cavités des bras kilométriques d'Advanced Virgo pendant la prise de données O3 (04/2019 – 03/2020). Ce calcul met en jeu les modes mécaniques des miroirs ainsi que les modes optiques des cavités de bras. Nous montrons l'influence sur les modes optiques et les gains paramétriques de la taille finie des miroirs, ainsi que de la déformation due à l'absorption thermique du laser dans les miroirs. Enfin, cette thèse donne également une prédiction sur les modes mécaniques qui seront potentiellement instables dans la configuration d'Advanced Virgo pendant la prochaine prise de données O4 qui devrait démarrer mi-2022.

Title : Study of optomechanical parametric instabilities in the Advanced Virgo detector

Keywords : Advanced Virgo detector, optomechanical parametric instability (OPI), cavity optical modes, Fabry-Perot optical resonator, spherical mirror cavity

Abstract : On 14 September 2015, the LIGO-Virgo collaboration performed the very first direct detection of a gravitational wave, emitted from a binary black hole merger. This detection demonstrated the existence of black holes and that of the gravitational waves. It required to detect an exceptionally weak signal — the order of 10^{-22} $Hz^{-1/2}$ in terms of strain amplitude. This tour de force was made possible thanks to several detector upgrades for over a decade.

Increasing the laser power is a way to improve the sensitivity of interferometric gravitational-wave detectors for it reduces even more the relative quantum shot noise at high frequency. However, optomechanical parametric instabilities can set a limit to that power.

This thesis presents the simulations that we have performed to compute the parametric gain of each mechanical mode of the four suspended 3km-arm-cavity mirrors of Advanced Virgo during the Observing run O3 (04/2019 – 03/2020). We study the influence of mirror finite size effects, and deformation due to thermal absorption, on optical modes and parametric gains. Finally, this thesis also gives a prediction on the potential unstable mechanical modes in Advanced Virgo's configuration during the next Observing run O4, which is expected to start in mid-2022.